HIGHLY STABLE METAL-ORGANIC FRAMEWORKS AND THEIR APPLICATIONS

A Dissertation

by

DAWEI FENG

Submitted to the Office of Graduate and Professional Studies of
Texas A&M University
in partial fulfillment of the requirements for the degree of

DOCTOR OF PHILOSOPHY

Chair of Committee,	Hong-Cai Zhou
Committee Members,	Marcetta Darensbourg
	Abraham Clearfield
	Perla Balbuena
Head of Department,	Francois Gabbai

August 2015

Major Subject: Chemistry

ABSTRACT

Metal-organic frameworks (MOFs) are a class of newly emerged porous materials. As inorganic-organic hybrid materials, MOFs exhibit many features such as crystalline structures, high surface areas, large porosities, and facile tunability However, the lack of high stability in harsh chemical conditions of most MOFs severely hampers MOFs' applications. This dissertation is focusing on synthesizing highly stable MOFs, developing new synthetic strategies towards single crystalline robust MOFs and their applications of catalysis, sensing as well as methane storage.

In the second section, a series of highly stable porphyrinic zirconium MOFs were synthesized. PCN-222 which exhibits one of the largest one dimensional channel and extraordinary stability in acidic condition, was studied as biomimetic catalyst. PCN-224, 221, 223 and 225 were studied as CO_2 fixation catalyst, alkane oxidation catalyst, catalyst for Diels Alder reaction and pH sensor respectively.

In the third section, a series of highly stable mesoporous MOFs were developed. In particular, PCN-333 exhibits the largest cage (5.5nm) among all the reported MOFs while maintaining excellent stability in aqueous environment. Therefore, PCN-333(Al) was selected for enzyme immobilization. Choosing horseradish peroxidase and cytochrome c as the guest enzymes, PCN-333(Al) shows the highest immobilization amount for both enzymes among all the reported porous supports. Meanwhile, the immobilized enzymes were proved having higher catalytic activity compared to the free enzymes.

In the fourth section, a new synthetic strategy towards robust Fe-MOFs, named kinetically tuned dimensional augmentation was developed. Using preformed iron carboxylate cluster, by judiciously adjusting the amount of competing reagent, 34 Fe-MOFs containing the same inorganic building block were successfully obtained with large singles crystals. Among these MOFs, PCN-250, which can be synthesized in large scale, shows one of the highest volumetric methane uptake capacity. More importantly, PCN-250 can be stable in water for more than six months without losing the porosity, which is superior to those other MOFs reported with high methane storage capacity. With its high gas uptake, extraordinary stability, and excellent scalability, PCN-250 is a viable candidate for natural gas storage for automotive applications.

In summary, a series of highly stable MOFs have been synthesized for different applications. In particular, the kinetically tuned dimensional augmentation strategy has been demonstrated as a facile method to synthesize single crystalline Fe-MOFs, which greatly facilitated the development of robust Fe-MOFs for practical applications.

DEDICATION

To my family, friends for their love and support

ACKNOWLEDGEMENTS

I would like to thank my committee chair, Dr. Hong-Cai Joe Zhou, and my committee members, Dr. Abraham Clearfield, Dr. Marcetta Darensbourg , and Dr. Perla Balbuena, for their guidance and support throughout the course of this research.

I will always appreciate my advisor, Dr. Zhou, for offering me the great opportunity to work in his lab. He gave me much insightful guidance and pushed me toward success in finishing my degree.

I will also thank all the group members with who I have been working. They are so friendly and patient in helping me. I would especially like to thank Dr. Daqiang Yuan, Mr. Kecheng Wang and Ms. Jihye Park. They worked with me closely and provided the best discussion and help I can ever have.

Thanks also go to the collaboration from Dr. Xiaodong Zou's group in Stockholm University,, Dr. Don Darensbourg's group in Texas A&M University, Dr. Berend Smit's group in University of California, Bekerley , Dr. Gregory J. Halder and Dr. Yu-Sheng Chen in Argonne National Lab BM-17 and ID-15, Dr. Mohammad A. Omary's group in University of North Texas. Their great work strongly supported and improved the quality of our research.

Thanks also go to my colleagues and the department faculty and staff for making my time at Texas A&M University a great experience.

My friends certainly deserve an acknowledgement. Your help in the five years in research and life have always been important to me.

Then I want to thank my wife Jianning Kong, my mother Boyan Ma and other family members, for their encouragement and love.

Finally, I would like to extend my gratitude to the funding agencies. U.S. Department of Energy (DOE Grants DE-FC36-07GO17033, DOE DE-SC0001015 and DE-AR0000073), part of the Methane Opportunities for Vehicular Energy (MOVE) Program, an ARPA-E Project under Award Number DE-AR0000249. Welch Foundation (A-1725), the National Science Foundation (NSF CBET-0930079), the National Science Foundation/Department of Energy under grant number NSF/CHE-0822838. Use of the Advanced Photon Source was supported by the U. S. Department of Energy, Office of Science, Office of Basic Energy Sciences, under Contract No. DE-AC02-06CH11357. China Scholarship Council.

NOMENCLATURE

BET	Brunauer-Emmett-Teller
FW	Formular Weight
MOF	Metal-Organic Framework
PCN	Porous Coordination Network
PSM	Post-Synthetic Modification
PXRD	Powder X-Ray Diffraction
SBU	Secondary Building Unit
TGA	Thermal Gravimetric Analysis
HRP	Horseradish Peroxidase
Cyto-c	Cytochrome C
MP-11	Microperoxidase-11

TABLE OF CONTENTS

Page

LIST OF FIGURES

Page

LIST OF TABLES

Page

1. INTRODUCTION

Metal-organic frameworks (MOFs), as an emerging class of porous materials, have attracted significant research interests over the past two decades. [1-5] As a new type of organic-inorganic hybrid porous solids consisting of metal nodes and organic linkers (Figure 1), MOFs exhibit crystalline structure, high internal surface area, , tunable structure, diverse functionality while compared to other convetional porous materials including activated carbons, mesoporous silica, and zeolites. [6-11] . Due to the above mentioned features, MOFs have been extensively studied for fundamental interests such as catalytic intermediate trapping, energy transfer, but also for potential practical applications including gas storage and separation, heterogeneous catalysis, chemical sensing, biomedical applications, proton conduction, and others. [12-15]

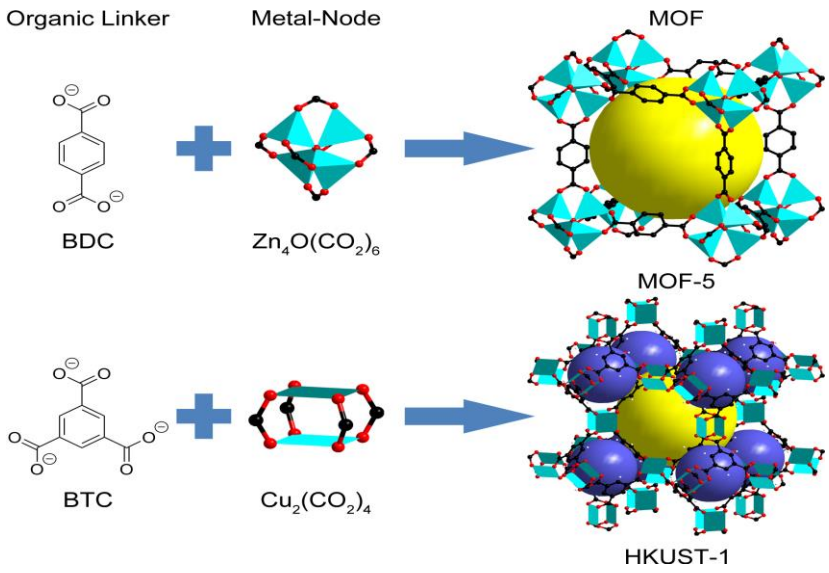

Figure 1. Schematic representation of synthesis of MOF-5 and HKUST-1.

When MOFs are used to certain applications, their framework intactness has always to be guaranteed to allow their feature properties to be fully utilized and maintained. However, most reported MOFs are suffering weak stability and can be hardly applied to harsh conditions, which severely restricted MOFs practical applications. [16] The major reason contributes to MOFs weak stability, especially chemical stability, is the labile metal-ligand coordination bond in the framework. The overwhelming majority of MOFs consists of carboxylate containing organic linkers and M^{2+} metal species, which gives rise to a combination of relatively soft Lewis acidic species and hard Lewis basic species, resulting in weak M-L bonds.[17] Therefore, the labile M-L bonds are undergoing fast dissociation (Figure 2) and the weak energy stabilization which makes it easily to be destructed by other reactive species, such as water, acid and base. Especially when certain functionality is incorporated into MOFs, when the weak M-L bond of the parent MOFs cannot stand for the harsh environment, the whole framework tends to collapse which would directly block the accessibility of the functional moieties in the framework, or even totally dissolved into homogenous status. Hence, guaranteeing MOFs stability is of great importance to ensure MOFs as practical materials.[18] To improve the stability of MOFs, high valent metal species are adopted due the stronger electron static interaction between them and the carboxylate end of the organic linkers. However, such MOFs are not very common (Figure 3). Such a discrepancy mainly arises from the differences of M-L bond dissociation rate in high valent metal containing MOFs compared to lower valence metals; for example their higher charge density which always results in strong

M-L bonds and thus less control over the crystallization process and/or in the formation of metal hydroxides or oxides. [20]

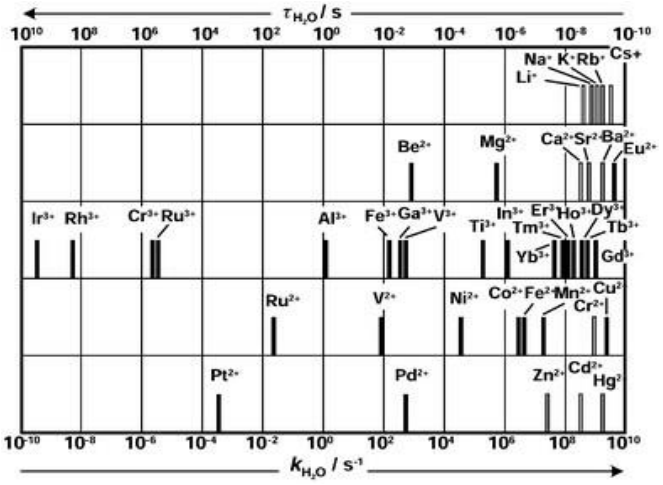

Figure 2. Rate of aqua ligand exchange for different metal cations as reference for M-L bond dissociation rate in carboxylate containing MOFs

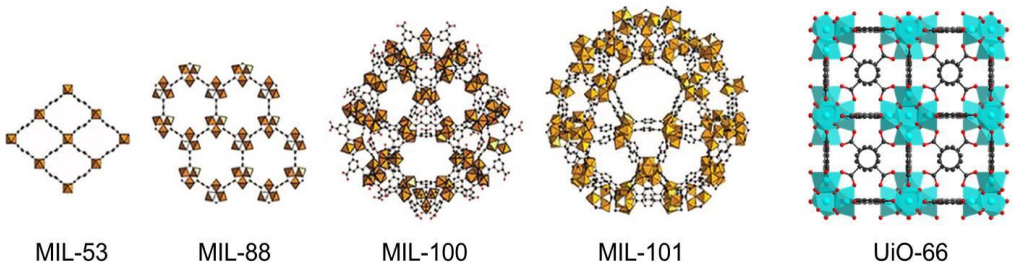

Figure 3. Representative robust MOFs

Therefore, making robust MOFs with desired structure, porosity, and internal surface property has always been a challenge. Almost all MOFs, in particular moisture-resistant MOFs constructed with high-valence metal ions, were made from the "one-pot" synthetic route, making it difficult to control the metal-containing nodes and therefore

the topology of the MOF. Several problems arise when targeting chemically stable MOFs through conventional one-pot reactions: (i) The overall design of novel MOFs with expected structures, even simple functionalization of existing MOFs for targeted applications, becomes very challenging because of the unpredictable in situ formation of inorganic building blocks; (ii) mixed phases often come out together due to the formation of diverse inorganic building blocks; (iii) polycrystalline or even amorphous products are prone to form, which not only bring challenges in structure determination, but also influence the properties of the targeted products.

To support the custom-designed functionalities in MOFs, therefore, synthesizing of stable MOFs with targeting functionality and more importantly development of facile synthetic method or strategy are sought-after goals for MOF chemists.

2. HIGHLY STABLE PORPHYRINIC ZIRCONIUM MOFS AND THEIR APPLICATIONS*

2.1 Zirconium-Metalloporphyrin PCN-222: Mesoporous Metal-Organic Frameworks with Ultrahigh Stability as A Biomimetic Catalyst

2.1.1 Introduction

In nature, metalloporphyrins are well known for performing many biological functions, such as light harvesting, oxygen transportation, and catalysis, in aqueous media. Heme, the iron-porphyrin derivative, is the cofactor for many enzyme/protein families, including peroxidases, cytochromes, hemoglobins, and myoglobins.[21-22] Using synthetic systems to mimic natural enzymes with high catalytic activity and distinct substrate selectivity has been a sought-after goal in the last decade. Direct application of a heme as an oxidation catalyst in aqueous solution is usually challenging due to the formation of catalytically inactive dimmer and self-destruction in the oxidizing reaction

*Reproduced with permission from: Feng, D.; Gu, Z.-Y.; Li, J.-R.; Jiang, H.-L.; Wei, Z.; Zhou, H.-C. "Zirconium-Metalloporphyrin PCN-222: Mesoporous Metal-Organic Frameworks with Ultrahigh Stability as A Biomimetic Catalyst" *Angew. Chem. Int. Ed.*, **2012**, *51*, *10307–10310*. Copyright 2012 by Wiley-VCH Verlag GmbH & Co. KGaA, Weinheim.; Feng, D.; Jiang, H.-L.; Chen, Y.-P.; Gu, Z.-Y.; Wei, Z.; Zhou, H.-C. "Metal−Organic Frameworks Based on Previously Unknown Zr_8/Hf_8 Cubic Clusters" *Inorg. Chem.*, **2013**, *52, 12661−12667*. Copyright 2013 American Chemical Society; Feng, D.; Jiang, H.-L.; Chen, Y.-P.; Gu, Z.-Y.; Wei, Z.; Zhou, H.-C. "Construction of Ultrastable Porphyrin Zr Metal−Organic Frameworks through Linker Elimination" *J. Am. Chem. Soc.*, **2013**, *135, 17105−17110*. Copyright 2013 American Chemical Society; Feng, D.; Gu, Z.-Y. ; Chen, Y.-P.; Park, J.; Wei, Z.; Sun, Y.; Bosch, M.; Yuan, S.; Zhou, H.-C. "A Highly Stable Porphyrinic Zirconium Metal-Organic Framework with shp-a Topology" *J. Am. Chem. Soc.*, ***2014,*** *136, 17714–17717*. Copyright 2014 American Chemical Society; Jiang, H.-L.; Feng, D.; Wang, K.; Gu, Z.-Y.; Wei, Z.; Chen, Y.-P.; Zhou, H.-C. "An Exceptionally Stable, Porphyrinic Zr Metal−Organic Framework Exhibiting pH-Dependent Fluorescence" *J. Am. Chem. Soc.*, **2013**, *135, 13934−13938.* Copyright 2013 American Chemical Society.

media.[23] One of the promising approaches is to load heme on supports, such as zeolites, clays, nanoparticles, hydrogels and carbon materials, which inevitably dilutes the density of active sites.[24-25] An alternative approach is to protect the heme centre by modifying the porphyrin to achieve dendrimers [26] or molecular crystals, [27] which is synthetically demanding. Herein, we propose a unique strategy by employing heme-like active center as structural motifs for the assembly of highly stable porous materials, which should possess well-defined meso-channels and ultrahigh stability in aqueous solution.

Metal-organic frameworks (MOFs) are a new class of crystalline porous materials with fascinating structures and intriguing properties, such as permanent porosity, high surface area, and uniform open cavities.[28] The availability of various building blocks of metals and organic linkers makes it possible to construct MOFs with unique properties for diverse applications.[29-40] However, these desirable features of MOFs have rarely been applied in an enzymatic mimic, especially for catalysis in an aqueous medium, despite the fact that assembly of ligands bearing high-density active sites into 3D frameworks may provide an ideal system to both enhance the catalytic activity and protect the cofactors.[41] One of the main reasons is the lack of water-stable MOFs containing redox-active metal centres [42-55] Additionally, most MOFs are microporous (pore size < 2 nm). Albeit suitable for gas storage, the small pore size slows down diffusion and limits the access of large substrate molecules to the active sites inside a MOF. Therefore, MOFs with meso-pores, accessible redox sites, and ultrahigh stability, especially in aqueous media, are indispensible for any successful biomimetic attempt in MOFs.[56]

2.1.2 Experimental Section

General Information Methyl 4-formylbenzoate was purchased from Oakwood Products. Inc. Pyrrole, propionic acid, *N*,*N*-dimethylformamide (DMF), *N*,*N*-diethylformamide (DEF), benzoic acid, acetone, iron(II) chloride tetrahydrate ($FeCl_2 \cdot 4H_2O$), manganese(II) chloride tetrahydrate ($MnCl_2 \cdot 4H_2O$), cobalt (II) chloride hexahydrate ($CoCl_2 \cdot 6H_2O$), nickel (II) chloride hexahydrate ($NiCl_2 \cdot 6H_2O$), copper (II) chloride hexahydrate ($CuCl_2 \cdot 2H_2O$), and zinc (II) chloride ($ZnCl_2$, anhydrous) were from Alfa Aesar. 5,10,15,20-Tetrakis(4-methoxycarbonylphenyl)porphyrin (TPPCOOMe) was prepared according to procedures described in Section S2. All commercial chemicals were used without further purification unless otherwise mentioned.

Powder X-ray diffraction (PXRD) was carried out with a BRUKER D8-Focus Bragg-Brentano X-ray Powder Diffractometer equipped with a Cu sealed tube (λ = 1.54178) at 40 kV and 40 mA. Elemental analysis (C, H, and N) were performed by Atlantic Microlab, Inc (Norcross, Georgia,). Thermogravimetry analysis (TGA) was conducted on a TGA-50 (SHIMADZU) thermogravimetric analyzer. Fourier transform infrared (IR) measurements were performed on a SHIMADZU IR Affinity-1 spectrometer. Nuclear magnetic resonance (NMR) data were collected on a Mercury 300 spectrometer. The UV-vis absorption spectra were recorded on a Shimadzu UV-2450 spectrophotometer. N_2 adsorption-desorption isotherms were measured using a Micrometritics ASAP 2420 system at 77K.

Ligand Synthesis The tetrakis(4-carboxyphenyl)porphyrin (H_2TCPP) ligand was purchased from Frontier Scientific. Other metal-involved TCPP (M-TCPP) ligands were synthesized based on previous reports with modifications. Typically, we obtained them by three steps as follows:

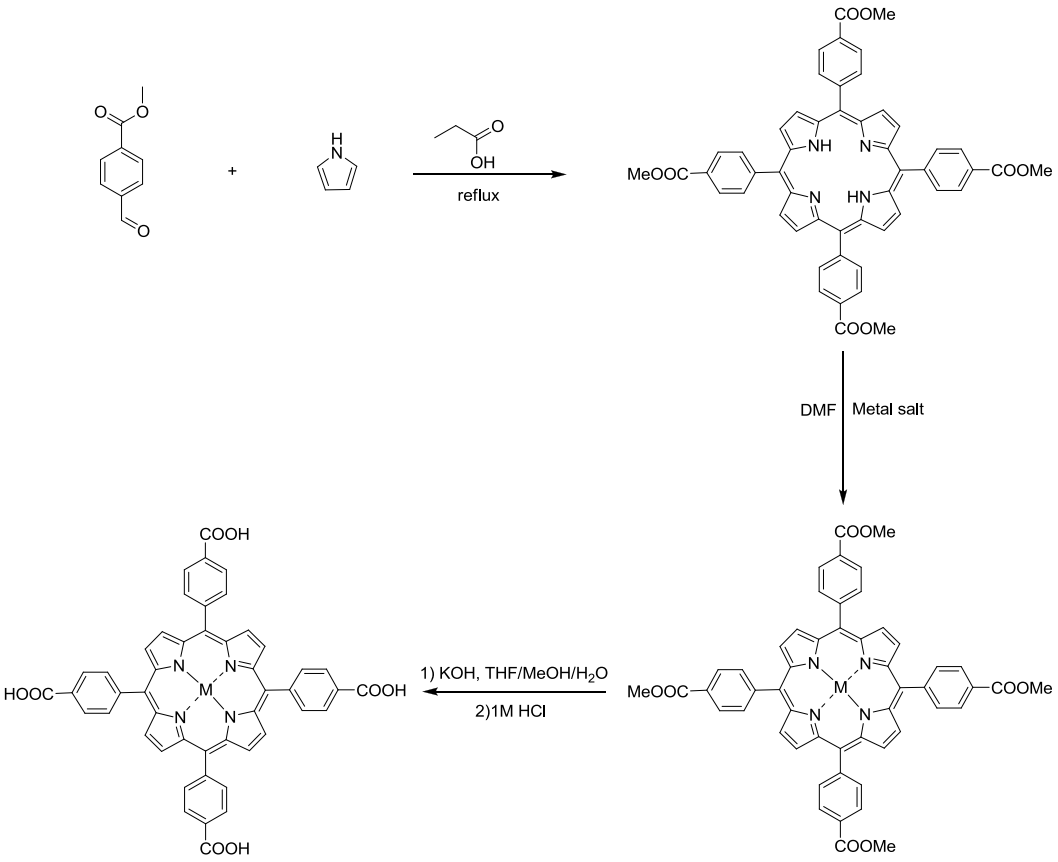

Scheme 1. Synthesis strategy for M-TCPP ligands.

To refluxed propionic acid (100 mL) in a 500-mL three necked flask were added pyrrole (3.0, 0.043 mol) and methyl *p*-formylbenzoate (6.9 g, 0.042 mol), and the solution was refluxed for 12h in darkness. After the reaction mixture was cooled to room temperature, crystals were collected by suction-filtration to afford purple crystals (1.9g, 2.24mmol, 21.3% yield). ^{1}H NMR (300 MHz, $CDCl_3$) δ 8.81 (s, 8H), 8.43 (d, 8H), 8.28 (d, 8H), 4.11 (s, 12H), -2.83 (s, 2H).

Synthesis of [5,10,15,20-Tetrakis(4-methoxycarbonylphenyl)porphyrinato]-Fe(III) Chloride A solution of TPP-COOMe 0.854 g (1.0 mmol) and $FeCl_2 \cdot 4H_2O$ (2.5 g, 12.8 mmol) in 100 mL of DMF was refluxed for 6 h. After the mixture was cooled to room temperature, 150 mL of H_2O was added. The resultant precipitate was filtered and washed with 50 mL of H_2O for two times. The obtained solid was dissolved in $CHCl_3$, followed by washing three times with 1 M HCl and twice with water. The organic layer was dried over anhydrous magnesium sulfate and evaporated to afford quantitative dark brown crystals.

Synthesis of [5,10,15,20-Tetrakis(4-methoxycarbonylphenyl)porphyrinato]-Mn(III) Chloride A solution of TPP-COOMe 0.854 g (1.0 mmol) and $MnCl_2 \cdot 4H_2O$ (2.5 g, 12.8 mmol) in 100 mL of DMF was refluxed for 6 h. After the mixture was cooled to room temperature, 150 mL of H_2O was added. The resultant precipitate was filtered and washed with 50 mL of H_2O for two times. The obtained solid was dissolved in $CHCl_3$, followed by washing three times with water. The organic layer was dried over anhydrous magnesium sulfate and evaporated to afford quantitative dark green crystals.

[5,10,15,20-Tetrakis(4-methoxycarbonylphenyl)porphyrinato]-Co(II) A solution of TPP-COOMe 0.854 g (1.0 mmol) and $CoCl_2 \cdot 6H_2O$ (3.1 g, 12.8 mmol) in 100 mL of DMF was refluxed for 6 h. After the mixture was cooled to room temperature, 150 mL of H_2O was added. The resultant precipitate was filtered and washed with 50 mL of H_2O for two times. The obtained solid was dissolved in $CHCl_3$, followed by washing three times with water. The organic layer was dried over anhydrous magnesium sulfate and evaporated to afford quantitative red crystals.

[5,10,15,20-Tetrakis(4-methoxycarbonylphenyl)porphyrinato]-Ni(II) A solution of TPP-COOMe 0.854 g (1.0 mmol) and $NiCl_2 \cdot 6H_2O$ (3.1 g, 12.8 mmol) in 100 mL of DMF was refluxed for 6 h. After the mixture was cooled to room temperature, 150 mL of H_2O was added. The resultant precipitate was filtered and washed with 50 mL of H_2O for two times. The obtained solid was dissolved in $CHCl_3$, followed by washing three times with 1 M HCl and twice with water. The organic layer was dried over anhydrous magnesium sulfate and evaporated to afford quantitative crimson crystals.

[5,10,15,20-Tetrakis(4-methoxycarbonylphenyl)porphyrinato]-Cu(II) A solution of TPP-COOMe 0.854 g (1.0 mmol) and $CuCl_2 \cdot 2H_2O$ (2.2g, 12.8 mmol) in 100 mL of DMF was refluxed for 6 h. After the mixture was cooled to room temperature, 150 mL of H_2O was added. The resultant precipitate was filtered and washed with 50 mL of H_2O for two times. The obtained solid was dissolved in $CHCl_3$, followed by washing three times with water. The organic layer was dried over anhydrous magnesium sulfate and evaporated to afford quantitative dark red crystals.

[5,10,15,20-Tetrakis(4-methoxycarbonylphenyl)porphyrinato]-Zn(II) A solution of TPP-COOMe 0.854 g (1.0 mmol) and $ZnCl_2$ (1.75 g, 12.8 mmol) in 100 mL of DMF was refluxed for 6 h. After the mixture was cooled to room temperature, 150 mL of H_2O was added. The resultant precipitate was filtered and washed with 50 mL of H_2O for two times. The obtained solid was dissolved in $CHCl_3$, followed by washing three times with water. The organic layer was dried over anhydrous magnesium sulfate and evaporated to afford quantitative violet crystals.

Synthesis of [5,10,15,20-Tetrakis(4-carboxyphenyl)porphyrinato]-Fe(III) Chloride The obtained ester (0.75 g) was stirred in THF (25 mL) and MeOH (25 mL) mixed solvent, to which a solution of KOH (2.63 g, 46.95 mmol) in H_2O (25 mL) was introduced. This mixture was refluxed for 12 h. After cooling down to room temperature, THF and MeOH were evaporated. Additional water was added to the resulting water phase and the mixture was heated until the solid was fully dissolved, then the homogeneous solution was acidified with 1M HCl until no further precipitate was detected. The brown solid was collected by filtration, washed with water and dried in vacuum. FTIR (KBr): ν= 3444 (m), 3034 (w), 2634 (w), 1702 (s), 1614 (s), 1570 (m), 1404 (s), 1311 (m), 1277 (s), 1204 (m), 1180 (m), 1106 (m), 1004 (s), 862 (m), 799 (s), 770 (s), 721 (m) cm^{-1}.

Synthesis of [5,10,15,20-Tetrakis(4-carboxyphenyl)porphyrinato]-Mn(III) Chloride The obtained ester (0.75 g) was stirred in THF (25 mL) and MeOH (25 mL) mixed solvent, to which a solution of KOH (2.63 g, 46.95 mmol) in H_2O (25 mL) was introduced. This mixture was refluxed for 12 h. After cooling down to room temperature,

THF and MeOH were evaporated. Additional water was added to the resulting water phase and the mixture was heated until the solid was fully dissolved, then the homogeneous solution was acidified with 1M HCl until no further precipitate was detected. The dark green solid was collected by filtration, washed with water and dried in vacuum. FTIR (KBr): ν= 3414 (m), 3044 (m), 2644 (w), 1702 (s), 1609 (s), 1565 (w), 1404 (m), 1336 (w), 1306 (w), 1248 (m), 1207 (m), 1175 (m), 1101 (m), 1009 (s), 867 (m), 794 (s), 716 (m), 672 (w) cm^{-1}.

Synthesis of [5,10,15,20-Tetrakis(4-carboxyphenyl)porphyrinato]-Co(II) The obtained ester (0.75 g) was stirred in THF (25 mL) and MeOH (25 mL) mixed solvent, to which a solution of KOH (2.63 g, 46.95 mmol) in H_2O (25 mL) was introduced. This mixture was refluxed for 12 h. After cooling down to room temperature, THF and MeOH were evaporated. Additional water was added to the resulting water phase and the mixture was heated until the solid was fully dissolved, then the homogeneous solution was acidified with 1M HCl until no further precipitate was detected. The red solid was collected by filtration, washed with water and dried in vacuum. FTIR (KBr): ν= 3423 (m), 2950 (w), 2840 (w), 1719 (s), 1605 (s), 1546(m), 1458 (m), 1394 (s), 1351 (m), 1276 (s), 1177 (w), 1112 (s), 1002 (s), 868 (w), 833 (m), 798 (s), 716 (m) cm^{-1}.

Synthesis of [5,10,15,20-Tetrakis(4-carboxyphenyl)porphyrinato]-Ni(II) The obtained ester (0.75 g) was stirred in THF (25 mL) and MeOH (25 mL) mixed solvent, to which a solution of KOH (2.63 g, 46.95 mmol) in H_2O (25 mL) was introduced. This mixture was refluxed for 12 h. After cooling down to room temperature, THF and MeOH were evaporated. Additional water was added to the resulting water phase and

the mixture was heated until the solid was fully dissolved, then the homogeneous solution was acidified with 1M HCl until no further precipitate was detected. The crimson solid was collected by filtration, washed with water and dried in vacuum. FTIR (KBr): ν= 3434 (m), 3034 (m), 2790 (w), 1692 (s), 1609 (s), 1541 (m), 1389(s), 1346 (m), 1311 (m), 1282 (s), 1175 (m), 1106 (m), 1004 (s), 867 (m), 833 (m), 799 (s), 716 (m) cm^{-1}.

Synthesis of [5,10,15,20-Tetrakis(4-carboxyphenyl)porphyrinato]-Cu(II) The obtained ester (0.75 g) was stirred in THF (25 mL) and MeOH (25 mL) mixed solvent, to which a solution of KOH (2.63 g, 46.95 mmol) in H_2O (25 mL) was introduced. This mixture was refluxed for 12 h. After cooling down to room temperature, THF and MeOH were evaporated. Additional water was added to the resulting water phase and the mixture was heated until the solid was fully dissolved, then the homogeneous solution was acidified with 1M HCl until no further precipitate was detected. The dark red was collected by filtration, washed with water and dried in vacuum. FTIR (KBr): ν= 3447 (m), 3060 (m), 2666 (w), 1696 (s), 1609 (m), 1565 (w), 1512 (w), 1456 (m), 1344 (m), 1289 (m), 1175 (m), 1101 (m), 1002 (s), 794 (s), 716(m) cm^{-1}.

Synthesis of [5,10,15,20-Tetrakis(4-carboxyphenyl)porphyrinato]-Zn(II) The obtained ester (0.75 g) was stirred in THF (25 mL) and MeOH (25 mL) mixed solvent, to which a solution of KOH (2.63 g, 46.95 mmol) in H_2O (25 mL) was introduced. This mixture was refluxed for 12 h. After cooling down to room temperature, THF and MeOH were evaporated. Additional water was added to the resulting water phase and the mixture was heated until the solid was fully dissolved, then the homogeneous

solution was acidified with 1M HCl until no further precipitate was detected. The violet solid was collected by filtration, washed with water and dried in vacuum. FTIR (KBr): ν= 3438 (m), 3040 (m), 2665 (w), 1680 (s), 1605 (s), 1565 (m), 1504 (m), 1423 (s), 1316 (m), 1291 (s), 1182 (m), 1105 (m), 1002 (s), 867 (m), 798 (s), 768 (m), 720 (m) cm^{-1}.

Synthesis of PCN-222(Fe) $ZrCl_4$ (70 mg), FeTCPPCl (50 mg) and benzoic acid (2700 mg) in 8 mL of DEF were ultrasonically dissolved in a 20 mL Pyrex vial. The mixture was heated in 120 ℃ oven for 48 h. After cooling down to room temperature, dark brown needle shaped crystals were harvested by filtration (35 mg, 46% yield). FTIR (KBr): ν= 3381 (m), 2952 (w), 1705 (w), 1601 (s), 1549 (s), 1411 (vs), 1340 (s), 1182 (m), 1003 (s), 871 (w), 809 (m), 776 (m), 723 (s) cm^{-1}. Anal. calcd. (%) for PCN-222(Fe): C, 44.84; H, 2.50; N, 4.36%. Found: C, 45.59; H, 3.12; N, 4.89%.

Synthesis of PCN-222(Mn) $ZrCl_4$ (70 mg), MnTCPPCl (50 mg) and benzoic acid (2700 mg) in 8 mL of DMF were ultrasonically dissolved in a 20 mL Pyrex vial. The mixture was heated in 120 ℃ oven for 48 h. After cooling down to room temperature, dark green needle shaped crystals were harvested by filtration (35mg, 48% yield). FTIR (KBr): ν= 3362 (m), 1710 (w), 1606 (s), 1544 (s), 1411 (vs), 1345 (s), 1182 (m), 1004 (s), 874 (w), 808 (m), 775 (m), 723 (s) cm^{-1}. Anal. calcd. (%) for PCN-222(Mn): C, 44.87; H, 2.51; N, 4.36%. Found: C, 44.73; H, 2.71; N, 3.67%.

Synthesis of PCN-222(Co) $ZrCl_4$ (70 mg), CoTCPP (50 mg) and benzoic acid (2700 mg) in 8 mL of DEF were ultrasonically dissolved in a 20 mL Pyrex vial. The mixture was heated in 120 ℃ oven for 48 h. After cooling down to room temperature, red needle shaped crystals were harvested by filtration (35 mg, 47% yield). FTIR (KBr):

ν= 3438 (m), 3057 (w), 2923 (w), 1710 (w), 1658 (s), 1601 (s), 1554 (s), 1416 (vs), 1350 (s), 1174 (m), 1103 (m), 1070 (w), 1000 (s), 871 (w), 804 (m), 780 (m), 714 (s) cm^{-1}. Anal. calcd. (%) for PCN-222(Co): C, 45.59; H, 2.57; N, 4.47%. Found: C, 43.97; H, 3.57; N, 4.38%.

Synthesis of PCN-222(Ni) $ZrCl_4$ (70 mg), NiTCPP (50 mg) and benzoic acid (2700 mg) in 8 mL of DEF were ultrasonically dissolved in a 20 mL Pyrex vial. The mixture was heated in 120 ℃ oven for 48 h, and then raised up to 130 ℃ for 24h. After cooling down to room temperature, crimson needle shaped crystals were harvested by filtration (30 mg, 41% yield). FTIR (KBr): ν= 3419 (m), 2933 (w), 1710 (w), 1659 (s), 1601 (s), 1558 (s), 1416 (vs), 1354 (s), 1184 (m), 1101 (m), 1000 (s), 871 (w), 804 (m), 780 (m), 714 (s) cm^{-1}. Anal. calcd. (%) for PCN-222(Ni): C, 46.00; H, 2.57; N, 4.47%. Found: C, 44.37; H, 2.56; N, 4.08%.

Synthesis of PCN-222(Cu) $ZrCl_4$ (70 mg), CuTCPP (50 mg) and benzoic acid (2700 mg) in 8 mL of DEF were ultrasonically dissolved in a 20 mL Pyrex vial. The mixture was heated in 120 ℃ oven for 48 h. After cooling down to room temperature, dark red needle shaped crystals were harvested by filtration (38 mg, 51% yield). FTIR (KBr): ν= 3428 (m), 3076 (w), 2952 (w), 1720 (m), 1653 (s), 1601 (s), 1553 (s), 1416 (vs), 1345 (s), 1179 (m), 1098 (m), 1000 (s), 871 (w), 804 (m), 780 (m), 723 (s) cm^{-1}. Anal. calcd. (%) for PCN-222(Cu): C, 45.80; H, 2.56; N, 4.36%. Found: C, 47.59; H, 2.66; N, 4.12%.

Synthesis of PCN-222(Zn) $ZrCl_4$ (70 mg), H_2TCPP (50 mg), $ZnCl_2$ (50mg), and benzoic acid (2700 mg) in 8 mL of DEF were ultrasonically dissolved in a 20 mL Pyrex

vial. The mixture was heated in 120 ℃ oven for 48 h. After cooling down to room temperature, violet needle shaped crystals were harvested by filtration (38 mg, 52% yield). FTIR (KBr): ν= 3281 (m), 2933 (w), 1705 (w), 1689 (s), 1601 (s), 1557 (s), 1415 (vs), 1352 (s), 1185 (m), 1101 (m), 1002 (s), 871 (w), 804 (m), 780 (m), 723 (s) cm^{-1}. Anal. calcd. (%) for PCN-222(Zn): C, 45.76; H, 2.56; N, 4.44%. Found: C, 44.99; H, 3.02; N, 4.72%.

Synthesis of PCN-222(No metal) $ZrCl_4$ (75 mg), H_2TCPP (50 mg) and benzoic acid (2700 mg) in 8 mL of DEF were ultrasonically dissolved in a 20 mL Pyrex vial. The mixture was heated in 120 ℃ oven for 48 h. After cooling down to room temperature, purple needle shaped crystals were harvested by filtration (35 mg, 46% yield). FTIR (KBr): ν= 3314 (m), 3076 (w), 1691 (w), 1601 (s), 1544 (s), 1410 (vs), 1269 (m), 1179 (m), 1018 (m), 961 (s), 871 (w), 799 (m), 771 (m), 724 (s) cm^{-1}. Anal. calcd. (%) for PCN-222(No metal): C, 48.18; H, 2.86; N, 4.68%. Found: C, 46.85; H, 2.98; N, 4.39%.

Syntheses of PCN-222(M) with Improved Yield $ZrCl_4$ (75 mg), MTCPP (50 mg, M= Fe(III), Mn(III), Co(II), Ni(II), Cu(II), Zn(II), H2) and benzoic acid (2700 mg) in 8 mL of DEF were ultrasonically dissolved in a 20 mL Pyrex vial. The vial was heated in oil bath at 120 ℃ under stirring with a stir bar inside for 24 h. After cooling down to room temperature, powder was obtained by centrifuge. The yield of PCN-222(M) was improved to 86%-89% corresponding to each ligand.

Single-Crystal X-ray Crystallography Single crystals of PCN-222 with different porphyrinic metal centers suitable for synchrotron single-crystal X-ray diffraction have

been obtained in our experiments. As their similar structures evidenced by powder X-ray diffraction, single crystal data of PCN-222(Fe) was collected only as a representative.

The single crystal (size: 0.07 x 0.03 x 0.025 cm^3, purple blade) intensity data were collected at **150K** on a D8 goniostat equipped with a Bruker APEXII CCD detector at Beamline 11.3.1 at the Advanced Light Source (Lawrence Berkeley National Laboratory) using synchrotron radiation tuned to **λ=0.7749Å**. For data collection frames were measured for a duration of 2-s at 0.5^o intervals of ω with a maximum 2θ value of ~60^o. The data frames were collected using the program APEX2 and processed using the program SAINT routine within APEX2. The data were corrected for absorption and beam corrections based on the multi-scan technique as implemented in SADABS.[2] The structure was solved by direct methods using the SHELXS program of the SHELXTL package and refined by full-matrix least-squares methods with SHELXL.[3] Metal atoms were located from the E-maps and other non-hydrogen atoms were refined with anisotropic displacement parameters during the final cycles. Hydrogen atoms were placed in calculated positions with isotropic displacement parameters set to 1.2 × Ueq of the attached atom. The solvent molecules are highly disordered, and attempts to locate and refine the solvent peaks were unsuccessful. Contributions to scattering due to these solvent molecules were removed using the SQUEEZE routine of PLATON;[3] structures were then refined again using the data generated. The contents of the solvent region are not represented in the unit cell contents in the crystal data.

Table 1. Crystal data and structure refinements for PCN-222(Fe).

Formula	$C_{48}H_{32}ClFeN_4O_{16}Zr_3$
Fw	1285.75
Color	Brown
Crystal system	Hexagonal
Space group	*P*6/mmm
a, *b* (Å)	41.968(7)
c (Å)	17.143(2)
α ( )	90
β ( )	90
γ ( )	120
V (Å^3)	26149(7)
Z	6
$d_{calcd.}$ (g/cm^3)	0.487
μ(mm^{-1})	0.292
T (*K*)	173(2)
F(000)	3786
Reflns collected	125544
Independent reflns	6038
Obsd data [I>2σ(I)]	4741
Data/restraints/parameters	6038 / 0 / 181
GOF on F^2	1.045
*R*1, *wR*2 [I > 2σ(I)]	0.0551, 0.1438
*R*1, *wR*2 (all data)	0.0821, 0.1583

2.1.3 Results and Discussion

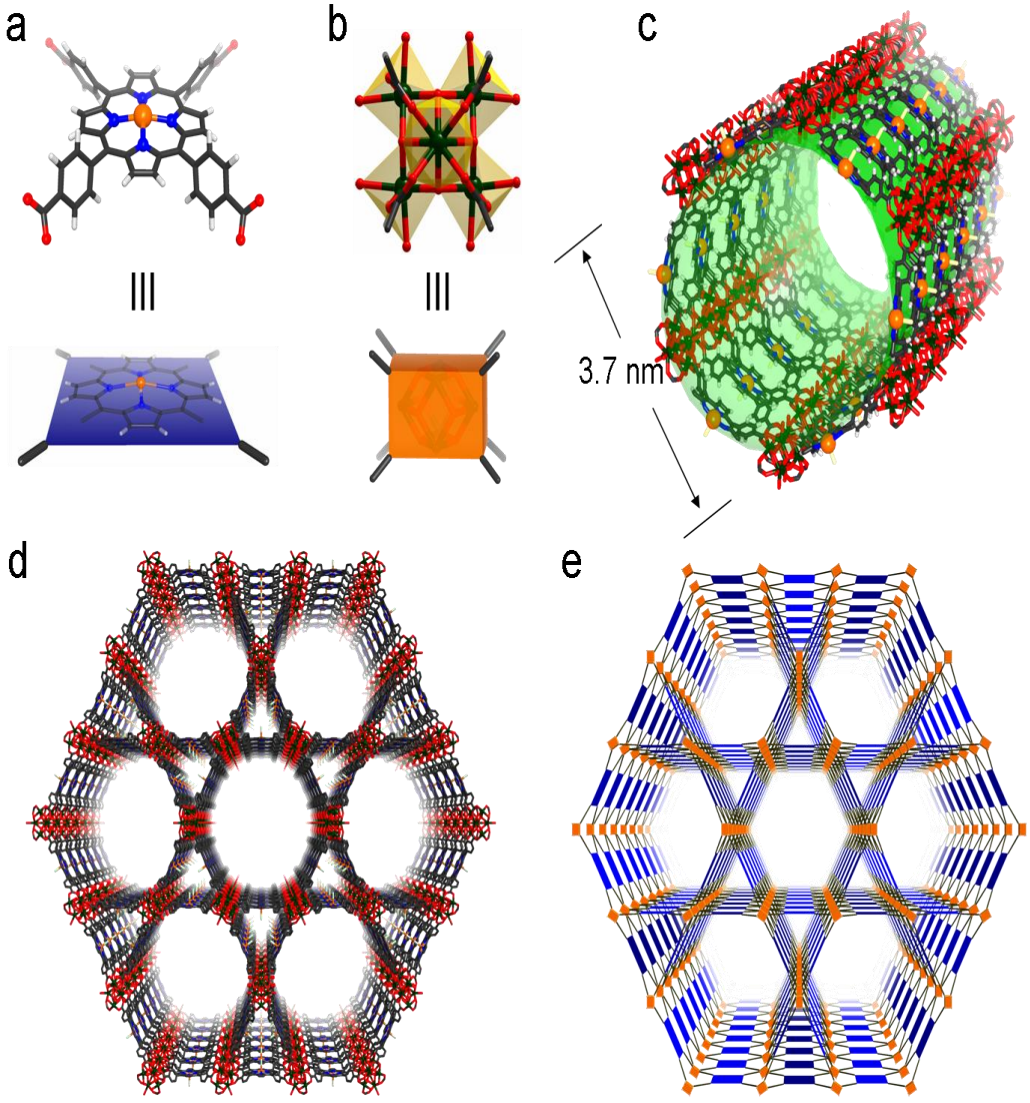

Figure 4. Crystal structure and underlying network topology of PCN-222(Fe). The Fe-TCPP (blue square, a) is connected to four 8-connected Zr_6 clusters (light orange cuboid, b) with twisted angle to generate a 3-D network in Kagome-like topology with 1-D large channels (green pillar, c) (d, e). (Colour scheme: Zr, black spheres; C, grey; O, red; N, blue; and Fe, orange. H atoms were omitted for clarity.)

Solvothermal reactions of M-TCPP (M = Fe, Mn, Co, Ni, Cu, Zn, H_2) (50 mg), $ZrCl_4$ (70 mg) and benzoic acid (2.7 g) in N, N-dimethylformamide or N, N-diethylformamide for 48 h at 120 °C yielded needle shaped single crystals of PCN-222. Single-crystal X-ray diffraction studies revealed that PCN-222(Fe) crystalizes in space group *P*6/*mmm*. Its framework consists of Zr_6 clusters linked by the square planar TCPP ligands. Each $Zr_6(OH)_8$ core, in which all of the triangular faces in a Zr_6-octahedron are capped by μ_3-OH groups, is connected to eight TCPP ligands. Different from the well-known 12-connected Zr_6 cluster observed in the UiO-series of MOFs,[57] only eight edges of the Zr_6 octahedron are bridged by carboxylates from TCPP ligands in PCN-222, while the remaining positions are occupied by terminal –OH groups. Consequently, the symmetry of the Zr_6 carboxylate unit is reduced from O_h to D_{4h}, which potentially engenders additional space for the formation of meso-pores. Interestingly, the benzene rings of TCPP ligand also rotate 35.88° from the original position corresponding to that in the free ligands. The 3D framework of PCN-222 can also be viewed as zirconium-carboxylate layers, which form a Kagome-type pattern in the *ab* plane, pillared by TCPP ligands. Remarkably, the 3D framework contains very large hexagonal 1D open channels with a diameter as large as 3.7 nm along the *c*-axis, among one of the largest reported in MOFs.[58-59]

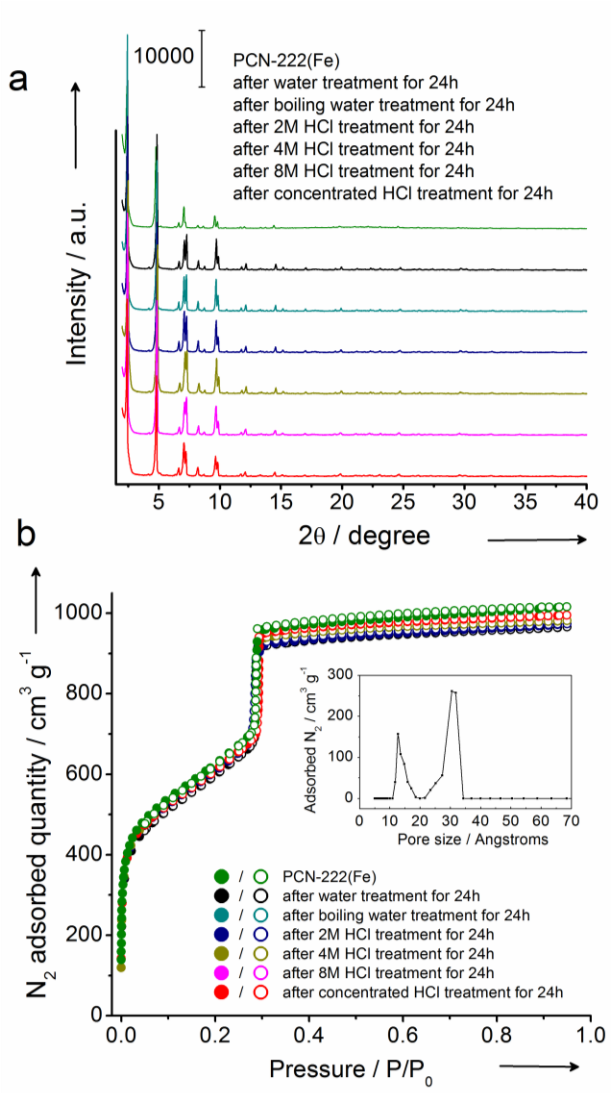

Figure 5. (a) Powder X-ray diffraction pattern and (b) N_2 adsorption isotherms for PCN-222(Fe) at 77 K, showing the framework stability of PCN-222(Fe) upon treatments with water, boiling water, 2 M, 4 M, 8 M and even concentrated HCl; Inset, DFT pore size distribution for original PCN-222(Fe) using data measured with N_2 at 77K.

The porosity of PCN-222 has been examined by nitrogen adsorption experiments at 77 K. The typical type IV isotherm of PCN-222(Fe) exhibits a steep increase at the point of P/P_0 = 0.3, suggesting meso-porosity. A N_2 uptake of 1009 cm^3 g^{-1} (STP) and a Brunauer-Emmett-Teller (BET) surface area of 2200 m^2 g^{-1} have been observed for

PCN-222(Fe), when the activation procedures were carefully optimized by applying a dilute acid solution for pre-activation treatments. The experimental total pore volume of 1.56 cm^3 g^{-1} is also in good agreement with the calculated pore volume of 1.63 cm^3 g^{-1}. Based on the evaluation of density functional theory (DFT) simulation from the N_2 sorption curve, there are two types of pores with sizes of 1.3 nm and 3.2 nm (Figure 4b inset), respectively assigned to triangular micro-channels and hexagonal meso-channels, which are consistent with the crystallographic data when van der Waals contact is considered. Other PCN-222 MOFs with different porphyrin centres also showed similar type IV N_2 sorption isotherms and gave surface area, N_2 uptake, and total pore volume up to 2312 m^2 g^{-1}, 1067 cm^3 g^{-1} (STP), and 1.65 cm^3 g^{-1}, respectively

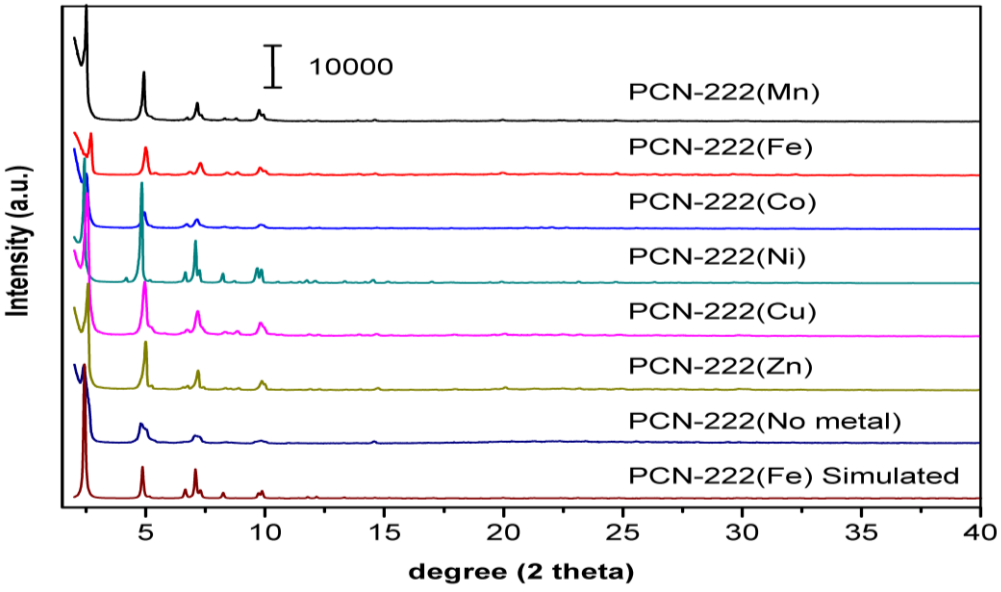

Figure 6. Powder XRD profiles for simulated and experimental PCN-222 samples.

The freshly made PCN-222 samples show much lower porosity compared to calculated ones, which could be possibly resulted from the residues trapped inside of the ultralarge 1-D channels. To remove those residues, before sorption experiment, as-synthesized PCN-222 (~100 mg) samples were immersed into 40 mL DMF to remove unreacted starting ligands, inorganic species and trapped benzoic acid at 120 ℃ for 12 h. For optimization of activation procedures, specific amount of HCl aqueous solution were added to the DMF suspension of PCN-222. Afterwards, extract was carefully decanted and washed with DMF and acetone for one time. Fresh acetone was subsequently added, and the sample was allowed to stay for 24 h to exchange and remove the nonvolatile solvates (DMF). After the removal of acetone by decanting, the sample was activated by drying under vacuum for 6 h, then was dried again by using the 'outgas' function of the adsorption instrument for 12 h at 120 ℃ prior to gas adsorption/desorption measurement.

The N_2 adsorption-desorption isotherms of PCN-222(Fe) with different amounts of HCl during activation were given to optimize the procedure. The mesopore size and overall uptake were increased with increasing amount of HCl added to DMF solution. After enough HCl added to the system, no further improvement was observed when adding more HCl, on the other hand, indicating the excellent stability of PCN-222. Finally, we chose adding 1.5 mL of 8 M HCl to 40 mL DMF suspension of PCN-222 (60mg) as typical activation step. N_2 adsorption isotherms of PCN-222(Mn) and PCN-222(Ni) in the absence and presence of HCl also demonstrated the great improvement of pore size and pore volume when using acid activation.

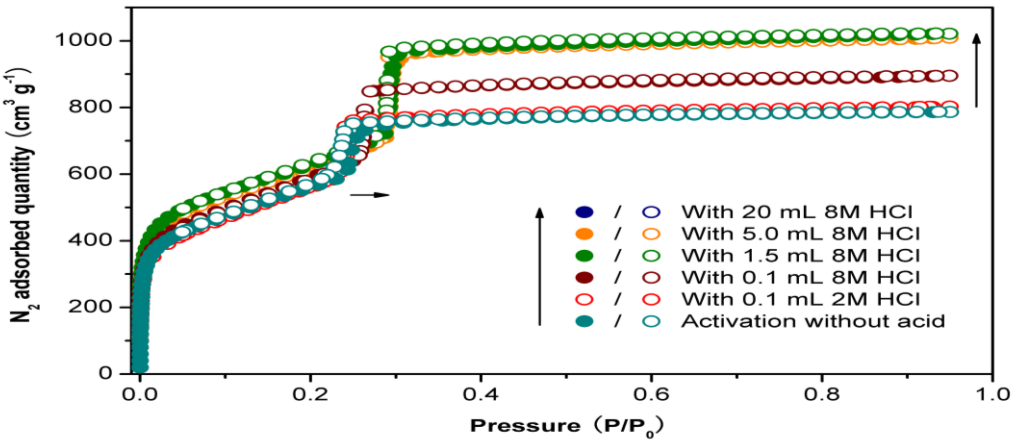

Figure 7. N_2 adsorption-desorption isotherms for PCN-222(Fe) at 77 K, 1 atm with different activation methods.

Table 2. Surface areas, mesopore sizes, N_2 uptakes and total pore volumes for PCN-222 samples

MOFs	BET surface area (m^2 g^{-1})	Mesopore size (Å) [a]	N_2 uptake (STP cm^3 g^{-1}) [b]	Total pore volume (cm^3 g^{-1}) [c]
PCN-222(Fe)	2200	32.0	1009	1.56
PCN-222(Mn)	2046	29.7	906	1.40
PCN-222(Co)	1864	30.0	844	1.31
PCN-222(Ni)	2283	32.0	1067	1.65
PCN-222(Cu)	2312	31.0	899	1.39
PCN-222(Zn)	1906	30.1	764	1.18
PCN-222(No metal)	2223	31.9	846	1.31

[a] calculated based on DFT method. [b] measurement was taken at P/P_0=0.95. [c] calculated by single point method.

Counter-intuitively, PCN-222 series possess not only one of the largest open channels, but also extraordinary stability among all MOFs. The powder X-ray diffraction (XRD) patterns remain intact upon immersion in water, boiling water, as well as 2M, 4M, 8M, and even concentrated HCl aqueous solutions for 24 h, suggesting no phase transition or framework collapse happening during these treatments (Figure 5a). More importantly, the N_2 sorption isotherms remained almost the same upon all treatments, which further confirmed the intactness of the tested frameworks (Figure 5b and Table 2). Strikingly, PCN-222(Fe) survived even after the treatment with concentrated HCl, a strong acid, which has rarely been observed for MOF materials, showing its exceptionally high chemical stability. The Zr_6 cluster, which was demonstrated as one of the most stable building units for MOF construction, is presumably responsible for the exceptional stability of PCN-222. Zr^{IV}, with its high charge density (Z/r), polarizes the O atoms of the carboxylate groups to form strong Zr–O bonds with significant covalent character. Furthermore, chelating effect stabilizes the four bonds between Fe^{III} and porphyrin. Therefore, the coordination bonds thus the whole framework becomes highly resistant to the attack of water and even acid.

PCN-222 is an extraordinary example that can meet all the prerequisites for a biomimetic system: ultra-large pore size, exceptionally high water stability, and potentially catalytically active centres. To test the catalytic activity, PCN-222 samples with different metalloporphyrins were employed in the oxidation reactions for several substrates, including pyrogallol, 3,3,5,5-tetramethylbenzidine and o-phenylenediamine

(Figure 6). These oxidation reactions are commonly used standard assays to characterize the catalytic performance of heme-like enzyme mimics. Kinetic studies revealed that an activated sample of PCN-222(Fe) exhibited excellent peroxidase-like catalytic activity, while other MOFs did not show significant activities under identical conditions (Figure 6).

Table 3. Kinetic parameters for the oxidation of substrates by different catalysts

Substrate	Catalyst	K_m (mM)	k_{cat} (min^{-1})	k_{cat}/K_m ($M^{-1}\cdot min^{-1}$)
pyrogallol	PCN-222(Fe)	0.33	16.1	4.85×10^4
	hemin[3a]	N/A	2.4	N/A
	HRP[3a]	0.81	1.8×10^3	2.20×10^6
3,3,5,5-tetramethylbenzidine	PCN-222(Fe)	1.63	14.0	8.59×10^3
	hemin[13]	0.78	0.1	1.26×10^2
	HRP[14]	0.43	2.4×10^5	5.58×10^8
o-phenylenediamine	PCN-222(Fe)	8.92	7.3	8.18×10^2
	hemin[13]	N/A	0.8	N/A
	HRP[15]	0.16	3.2×10^4	4.51×10^7

These reactions catalyzed by PCN-222(Fe) were carried out with constant hydrogen peroxide and catalyst concentrations (2.5 μM or 10 μM active site equivalent) but variable substrate concentrations. The reaction process follows the conventional enzymatic dynamic regulation of the Michiaelis-Menten equation that monitored by

absorption spectroscopy in kinetic mode. Based on the different oxidation rates with variable substrate concentrations, a Lineweaver-Burk plot can be obtained with a nearly ideal linear relationship, from which important kinetic parameters such as k_{cat} and K_m can be obtained (Table 3). The k_{cat} value gives a direct measure of the catalytic activity, *i.e.*, it measures the maximum number of substrate molecules turned over per catalyst molecule per unit time under optimal conditions. It can also be viewed as the optimum turnover rate. K_m is the Michaelis constant and often associated with the affinity of the catalyst molecules for the substrate. K_m is also a measure of the substrate concentration required for effective catalysis to occur. For pyrogallol oxidation reaction, the derived k_{cat} of the PCN-222(Fe) catalyst shows a high value of 16.1 min^{-1}, which is 7-times higher than k_{cat} of free hemin (2.4 min^{-1}). Moreover, the derived K_m value of 0.33 mM is lower than that of the natural enzyme horseradish peroxidase (HRP) (0.81 mM), indicating a better affinity of the substrate to PCN-222(Fe). Considering the fast rate of such catalytic reaction, complete utilization of the porphyrin centres is limited by the diffusion rate of the substrates, which indicates even higher k_{cat} values of effective catalytic centres in PCN-222(Fe). Such excellent catalytic performance can be attributed to the high density of porphyrin active centres in PCN-222(Fe), which provides one active site per 1286 Da. In sharp contrast, 44174 Da is necessary for each active site in HRP. Other substrates such as 3,3,5,5-tetramethylbenzidine and o-phenylenediamine have also been examined for peroxidase-like oxidation to demonstrate the general applicability of PCN-222(Fe) as enzyme mimics. PCN-222(Fe) showed superior

catalytic activity than free hemin as the obtained k_{cat} is nearly ten-times to over two orders of magnitude higher than that of free hemin.

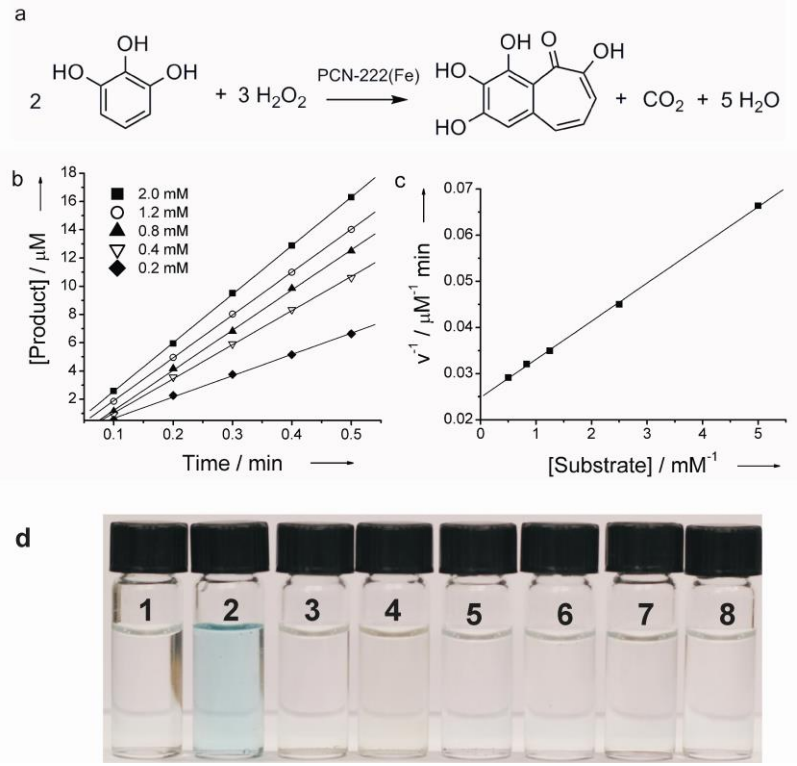

Figure 8. (a) Peroxidase-like oxidation reaction of pyrogallol catalyzed by PCN-222(Fe), in which pyrogallol is oxidized to purpurogallin by hydrogen peroxide. (b) The initial pyrogallol oxidation profile catalyzed by PCN-222(Fe) (2.5 μM active site equivalent). The concentrations of pyrogallol range from 0.2 mM to 2 mM. (c) Lineweaver-Burk plot of the pyrogallol oxidation catalyzed by PCN-222(Fe). (d) The image shows catalytic activity of PCN-222(Fe) (2) in comparison with 1: no catalyst, 3: PCN-222(Mn), 4: PCN-222(Co), 5: PCN-222(Ni), 6: PCN-222(Cu), 7: PCN-222(Zn), and 8: PCN-222(No metal) in the peroxidase-like oxidation of 3,3,5,5-tetramethylbenzidine (0.7 mM) after one minute.

For substrates with different sizes, it is clear that different level of concentration is required for effective catalysis (K_m). However, it is worth noting that k_{cat} values for diverse substrates on PCN-222(Fe) are similar, while entirely different catalytic

activities for these substrates are observed on hemin and HRP. It highlights that PCN-222(Fe) offers large channels with accessible catalytic sites for the substrates, which greatly facilitate their diffusion. The excellent catalytic performance of PCN-222(Fe) is attributed to the successful construction of stable 3-D structures with large open channels, which effectively prevents the self-dimerization of porphyrin centres and decrease diffusion resistance. Compared with reported MOFs with porphyrin encapsulated in the pores,[60-64] PCN-222 constructed by porphyrin struts with large meso-channels and high stability presents higher density of catalytic centres and faster diffusion rate of substrates, although it may not have specific selectivity for very small-size molecules.

2.1.4 Conclusions

In summary, we have successfully demonstrated a highly stable, mesoporous MOF PCN-222(Fe) exhibiting biomimetic catalytic activities. The active site of the catalyst is located on the inner wall of an open channel with a diameter of 3.7 nm and shows good activity for oxidation of a variety of substrates. The integration of high density of catalytic centers, ultra-large open channels, and extraordinary chemical stability of PCN-222(Fe) offers a bright future of building MOF-based platforms for enzyme-mimic catalysis.

2.2 Metal-Organic Frameworks Based on Previously Unknown Zr_8/Hf_8 Cubic Clusters

2.2.1 Introduction

Metal-organic frameworks (MOFs) are extended structures assembled from metal-containing units (metal cations or clusters) and organic linkers.[1] As a new class of porous materials, MOFs have attracted tremendous attention in the past two decades. One of the main reasons is their application potential in gas storage/separation, catalysis, sensing, and drug delivery,[2-5] thanks to their exceptionally high surface area as well as adjustable pore shape, size, and functionality. In the construction of MOFs, going from simple metal ions to metal clusters (M_2 paddlewheel, M_3O and M_4O basic carboxylates) represents a significant initial step. [65-66] The utilization of a new metal cluster as a structural unit often led to a series of new MOFs. In general, the introduction of metal clusters of high nuclearity has lead to MOFs with improved stability, which is a prerequisite for industrial applications. Although only a limited number of Zr-based MOFs were reported,[67-74] they have unambiguously shown improved stability compared to the common Zn/Cu/Cd-based carboxylate frameworks. Robust MOFs based on Zr clusters with high porosity are highly desirable for practical applications. However, it is particularly difficult to obtain single crystals of Zr-based MOFs due to the inert coordination bonds between Zr^{4+} cations and carboxylate anions, making ligand exchange reactions extremely slow, which is unfavorable for defect repair during crystal growth. To meet such a challenge, a modulated synthetic strategy was adopted and

benzoic acid was introduced to the reaction mixture. Such a synthetic strategy has greatly facilitated crystal growth for the study of Zr-MOFs, however, only a few MOFs containing Zr clusters have been reported, almost all of them are based on the octahedral Zr_6 cluster.

So far in cluster chemistry, Zr_3, Zr_4, Zr_5, Zr_6 and Zr_{10} clusters have been synthesized and characterized.[75-77] Due to very similar radii of Hf^{4+} and Zr^{4+} cations, polyoxohafnium clusters of Hf_3, Hf_4, Hf_6, Hf_{17} and Hf_{18} have also been reported.[78-79] Most of these clusters are difficult to incorporate into MOF structures due to symmetry limitations. To the best of our knowledge, only Zr_6 clusters and zirconium oxide chains have been introduced into Zr-MOFs. Only one Hf-MOF containing Hf_6 clusters was reported. In our continuing search for ultra-stable Zr- and Hf-MOFs, with tetrakis(4-carboxyphenyl)porphyrin (TCPP) as an organic linker, a series of MOFs supported by previously unknown Zr_8 and Hf_8 cubic clusters have been isolated and structurally characterized. The MOFs exhibit high surface area and interesting gas-sorption properties. In particular, a Zr_8-MOF constructed from an Fe-TCPP ligand was tested as a catalyst for cyclohexane oxidation, which revealed very high selectivity toward cyclohexanone and cyclohexanol formation using neat cyclohexane.

2.2.2 Experimental Section

Materials and Instrumentation Methyl 4-formylbenzoate was purchased from Oakwood Products, Inc. Pyrrole, propionic acid, *N*,*N*-dimethylformamide (DMF), *N*,*N*-diethylformamide (DEF), benzoic acid, acetone, zirconium(IV) chloride, hafnium(IV)

chloride, iron(II) chloride tetrahydrate ($FeCl_2 \cdot 4H_2O$), copper(II) chloride tetrahydrate ($CuCl_2 \cdot 4H_2O$), cobalt (II) chloride hexahydrate ($CoCl_2 \cdot 6H_2O$), chlorobenzene, tert-butyl hydroperoxide and cyclohexane were purchased from Alfa Aesar. 5,10,15,20-Tetrakis(4-methoxycarbonylphenyl)porphyrin (TPPCOOMe) was prepared according to procedures described below. All commercial chemicals were used without further purification unless otherwise mentioned.

Powder X-ray diffraction (PXRD) was carried out with a BRUKER D8-Focus Bragg-Brentano X-ray Powder Diffractometer equipped with a Cu sealed tube (λ = 1.54178) at 40 kV and 40 mA. Elemental analysis (C, H, and N) were performed by Atlantic Microlab, Inc (Norcross, Georgia). Thermogravimetry analyses (TGA) were conducted on a TGA-50 (SHIMADZU) thermogravimetric analyzer. Fourier transform infrared (IR) measurements were performed on a SHIMADZU IR Affinity-1 spectrometer. Nuclear magnetic resonance (NMR) data were collected on a Mercury 300 spectrometer. X-ray photoelectron spectra (XPS) were acquired with Axis Ultra DlD (Kratos) equipped with Al monochromatic X-rays operating at 12 kV and 10 mA. Gas sorption measurements were conducted using a Micrometritics ASAP 2420 system at different temperatures. Electron paramagnetic resonance (EPR) spectra for TCPP ligand and Zr-PCN-221(no metal) were recorded on a Varian E-line 12'' Century Series X-band CW spectrometer.

Synthesis of Zr-PCN-221(no metal) $ZrCl_4$ (7 mg), H_2TCPP (10 mg) and 7 drops of acetic acid or trifluoroacetic acid (80 μL) in 2 mL of DEF were ultrasonically dissolved in a Pyrex vial. The mixture was heated in 120 ℃ oven for 12 h. After cooling

down to room temperature, dark red powder was harvested by filtration (10 mg, 71% yield). FTIR (KBr, cm^{-1}): 1735 (w), 1664 (vs), 1587 (m), 1548 (m), 1408 (vs), 1257 (w), 1209 (w), 1185 (w), 1158 (w), 1099 (s), 1022 (w), 968 (s), 837 (w), 811 (m), 775 (s), 722 (m), 662 (vs). Anal. calcd. (%) for Zr-PCN-221(No metal): C, 52.29; H, 2.47; N, 5.28%. Found: C, 50.34; H, 2.84; N, 5.81%.

Synthesis of Zr-PCN-221(Fe) $ZrCl_4$ (7 mg), Fe-TCPPCl (10 mg) and 7 drops of acetic acid or trifluoroacetic acid (80 μL) in 2 mL of DEF were ultrasonically dissolved in a Pyrex vial. The mixture was heated in 120 ℃ oven for 12 h. After cooling down to room temperature, dark brown powder was harvested by filtration (10 mg, 70% yield). FTIR (KBr, cm^{-1}): 1738 (w), 1607 (s), 1545 (m), 1414 (vs), 1346 (w), 1182 (w), 1150 (w), 1102 (w), 998 (s), 870 (w), 805 (s), 776 (s), 710 (m), 671 (s). Anal. calcd. (%) for Zr-PCN-221(Fe): C, 51.67; H, 2.17; N, 5.02%. Found: C, 50.72; H, 2.12; N, 4.84%.

Synthesis of Zr-PCN-221(Cu) $ZrCl_4$ (10 mg), CuTCPP (10 mg) and benzoic acid (250 mg) in 2 mL of DMF were ultrasonically dissolved in a Pyrex vial. The mixture was heated in 120 ℃ oven for 12 h. After cooling down to room temperature, the mixture of dark red needle shaped and cubic crystals were harvested. The red needle phase has been demonstrated to be PCN-222[1] by powder X-ray diffraction. The cubic crystal, which is PCN-221, has been characterized by single X-ray diffraction.

Synthesis of Hf-PCN-221(Co) $HfCl_4$ (30 mg), CoTCPP (10 mg) and benzoic acid (400 mg) in 2 mL of DMF were ultrasonically dissolved in a Pyrex vial. The mixture was heated in 120 ℃ oven for 8 h. After cooling down to room temperature, red cubic crystals were harvested by filtration (10 mg, 47% yield). FTIR (KBr, cm^{-1}): 1750 (w),

1685 (m), 1643 (w), 1610 (w), 1548 (s), 1512 (s), 1414 (s), 1379 (m), 1340 (w), 1269 (w), 1150 (w), 1040 (m), 870 (w), 838 (w), 775 (w), 722 (m). Anal. calcd. (%) for Hf-PCN-221(Co): C, 42.65; H, 1.79; N, 4.15%. Found: C, 41.81; H, 2.40; N, 3.30%.

X-ray Crystallography A crystal was taken directly from the mother liquor, transferred to oil and mounted into a loop for single crystal X-ray data collection, which was conducted on a Bruker Smart Apex diffractometer equipped with a low temperature device (under 110 K) and a Mo-Kα sealed-tube X-ray source (λ = 0.71073 Å, graphite monochromator). The data frames were collected using the program APEX2 and processed using the program SAINT routine within APEX2. The data were corrected for absorption and beam correction based on the multi-scan technique as implemented in SADABS. The structures were solved by direct methods using SHELXS and refined by full-matrix least-squares on F^2 using SHELXL software.[80] Non-hydrogen atoms were refined with anisotropic displacement parameters during the final cycles. Organic hydrogen atoms were located in calculated positions with isotropic displacement parameters set to 1.2 × U_{eq} of the attached atoms. The solvent molecules are highly disordered, and attempts to locate and refine the solvent peaks were unsuccessful. Contributions to scattering due to these solvent molecules were removed using the SQUEEZE routine of PLATON;[81] structures were then refined again using the data generated. The contents of the solvent region are not represented in the unit cell contents in the crystal data. Crystallographic data and structural refinements for PCN-221 are summarized in Table 4.

Table 4. Crystal data and structure refinements for PCN-221.

Compound name	Zr-PCN-221(Cu)	Hf-PCN-221(Co)
Formula	$C_{144}H_{72}Cu_3N_{12}O_{30}Zr_8$	$C_{144}H_{72}C_{l0}Co_3Hf_8N_{12}O_{30}$
Fw	3370.52	4054.85
Color	Red	dark red
Crystal system	Cubic	Cubic
Space group	*Pm*-3*m*	*Pm*-3*m*
a, b, c (Å)	19.51(3)	19.152(3)
α, β, γ ( )	90	90
V (Å^3)	7424(21)	7025(2)
Z	1	1
$d_{calcd.}$ (g/cm^3)	0.754	0.959
μ(mm^{-1})	0.515	3.151
T (*K*)	173(2)	110(2)
F(000)	1667	1917
Reflns collected	67300	65582
Independent reflns	1350	1217
Obsd data [I>2σ(I)]	728	876
Data/restraints/parameter	1350 / 212 / 59	1217 / 16 / 25
Completeness	99.0 %	98.9 %
GOF on F^2	1.409	1.078
*R*1, *wR*2 [I > 2σ(I)]	0.1924, 0.4359	0.1996, 0.3284
*R*1, *wR*2 (all data)	0.2450, 0.4573	0.2412, 0.3488

Activation Procedures and Gas Sorption Measurements for PCN-221 Before gas sorption experiment, as-synthesized PCN-221 (~70 mg) samples were washed with DMF three times and once with acetone, and then immersed in acetone for over 12 h. Afterward, the mixture was centrifuged. After the removal of acetone by decanting, the samples were activated by drying under vacuum for 6 h, then were dried again by using the 'outgas' function of the adsorption instrument for 12 h at 80 ℃ prior to gas adsorption/desorption measurement.

Thermal Stability Examination for PCN-221 For the thermal stability test, 5-10 mg of PCN-221 sample was heated on a TGA-50 (Shimadzu) thermogravimetric analyzer from room temperature to 650 ℃ at a rate of 5 ℃ min^{-1} under N_2 flow of 50 mL min^{-1}. Both as-synthesized and activated samples for PCN-221 were measured.

Catalytic Reaction of Cyclohexane Oxidation over Zr-PCN-221(Fe) Given the presence of catalytically active porphyrinic metal centers, PCN-221 could be an ideal candidate for catalysis. Therefore, Zr-PCN-221(Fe) as a representative has been explored as a catalyst for cyclohexane oxidation. For the catalytic reaction, typically, tert-butyl hydroperoxide (84.7 μmol, 14 μL, 5.0-6.0 M in decane), cyclohexane (10 mL), chlorobenzene (0.1 mmol, 10 μL) and 5 mg Zr-PCN-221(Fe) catalyst were heated at 65 ℃ in a 25 mL three-necked round-bottom flask under neat conditions. The reaction progress was monitored by taking 1-3 μL of reaction mixture for GC-FID analysis over varying intervals. The reaction turnover number was calculated by dividing a summation of moles of cyclohexanol plus two times moles of cyclohexanone by moles of catalytic center (Fe).

2.2.3 Results and Discussions

Solvothermal reactions of zirconium(IV) or hafnium(IV) chloride, M'-TCPP (M' = Fe, Co, Cu, no metal), and benzoic acid in N,N-dimethylformamide (DMF) at 120 ℃ yielded cubic single crystals or polycrystalline powder of M_8O_6(M'-TCPP)$_3$ [Single crystals: M = Zr, M' = Cu, Zr-PCN-221(Cu). Both single crystals and pure powder phase: M = Hf, M' = Co, Hf-PCN-221(Co). Pure powder phase: M = Zr, M' = no metal, Zr-PCN-221(no metal); M = Zr, M' = Fe, Zr-PCN-221(Fe). PCN represents porous coordination networks]. Single-crystal and powder X-ray diffraction (XRD) studies have revealed that all PCN-221 crystallize in space group *Pm*-3*m* and are isostructural. Therefore, the structure of Zr-PCN-221(Cu) will be discussed below as a representative.

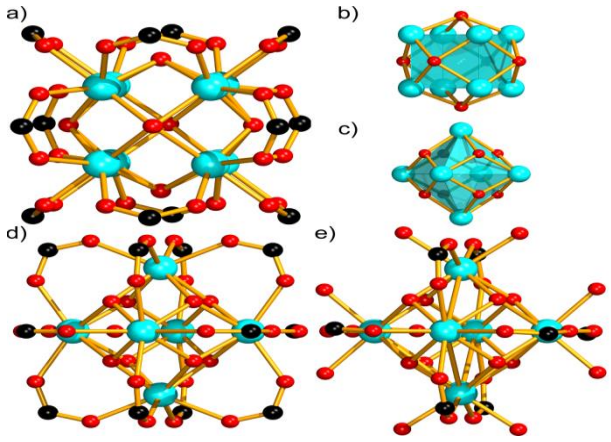

Figure 9. (a) $[Zr_8O_6(CO_2)_{12}]^{8+}$ cluster and (b) the Zr_8O_6 core in PCN-221. (c) The $Zr_6O_4(OH)_4$ core and (d) $Zr_6O_4(OH)_4(CO_2)_{12}$ cluster in PCN-56 with UiO-type structure. (e) $Zr_6(OH)_8(OH)_8(CO_2)_8$ cluster in PCN-222. The μ-oxo, terminal hydroxyl O, carboxylate O, Zr, and C atoms are shown in green, blue, red, purple, and dark gray, respectively. The Zr_6 octahedron (b) and Zr_8 cube (c) are highlighted in purple.

The unique zirconium, in a distorted octahedral coordination environment, coordinates three oxygen atoms from three carboxylates and three μ_4-oxygen atoms (Figure 9). Eight zirconium atoms connect six μ_4-oxygen atoms to form a Zr_8O_6 core leading to an idealized Zr_8 cube, in which the cubic vertices are occupied by zirconium atoms and the six faces are capped by six μ_4-oxygen atoms (Figure 9). Each edge of the Zr_8 cube is bridged by a carboxylate from a TCPP ligand to give a $[Zr_8O_6(CO_2)_{12}]^{8+}$ cluster with O_h symmetry. Bond-valence calculation shows that the total bond valence of a zirconium atom is +4.10, indicating the oxidation state of +4.[82-83] To further demonstrate the oxidation state of zirconium cations in PCN-221, X-ray photoelectron spectrum (XPS) and electron paramagnetic resonance (EPR) measurements have been conducted. As shown in Figure 10a, the positions for $3d_{3/2}$ and $3_{d5/2}$ peaks locate at 185 and 182.5 eV, respectively, which well match with those for Zr(IV) in ZrO_2.[84] In addition, EPR experiments for Zr-PCN-221(no metal) show that the signal positions are the same as those for H_2TCPP ligand (Figure 10b), revealing that the signals simply originate from the free radicals produced by the porphyrin-based ligand[85] but not zirconium cations. The weaker intensity of EPR signals in the MOF than those in the free ligand could be attributed to the lower concentrations of porphyrin center in the MOF. Both XPS and EPR results as described above approve the assignment of the oxidation state of +4 for the zirconium.

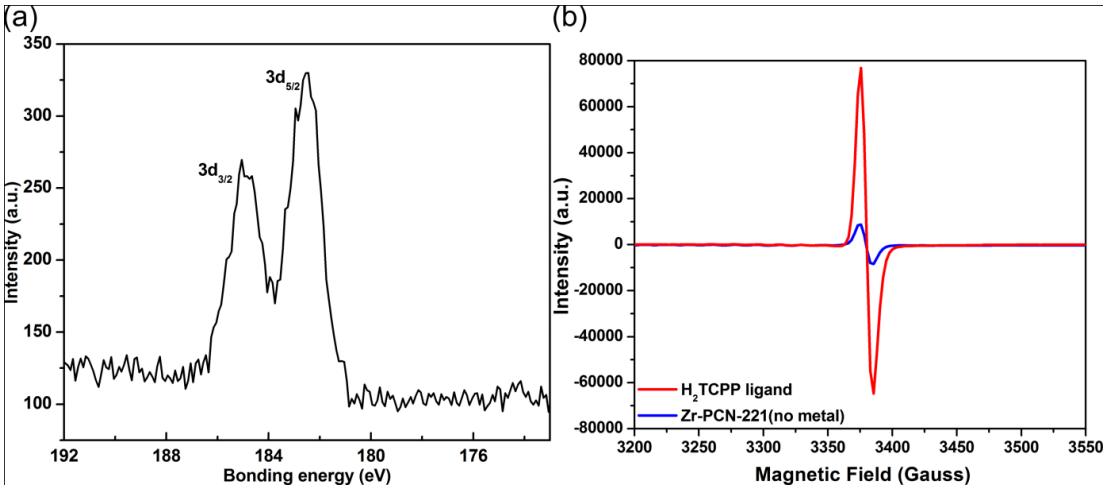

Figure 10. (a) XPS spectra of Zr 3d for Zr-PCN-221(no metal). (b) EPR curves for H_2TCPP ligand and Zr-PCN-221(no metal).

It is very interesting to compare the structures of Zr_8 and the previously reported Zr_6 clusters. As shown in Figure 9, the Zr_6 clusters have two types of coordination environments: $Zr_6O_4(OH)_4(CO_2)_{12}$ (Figure 9d) and $Zr_6(OH)_8(OH)_8(CO_2)_8$ (Figure 9e). The former has O_h symmetry and is composed of a $Zr_6O_4(OH)_4$ core coordinated by twelve carboxylate anions, while the latter has D_{4h} symmetry and is constructed with a $Zr_6(OH)_8$ core and the coordinated ligands are eight hydroxyl and eight carboxylate anions. Therefore, both Zr_6 clusters have similar cores of $Zr_6(OH)_8$ or $Zr_6O_4(OH)_4$, in which six zirconium atoms are connected by oxygen or/and hydroxyl groups to form a Zr_6 octahedron, the triangular faces of which are capped by eight μ_3-OH groups or alternatively capped by μ_3-O and μ_3-OH groups (Figure 9c). Remarkably, the zirconium and oxygen atoms exchange positions with each other in the Zr_8O_6 core in PCN-221 and the Zr_6O_8 [or $Zr_6O_4(OH)_4$] cluster core (Figure 9b, c).

The average dihedral angle between a benzene ring of a TCPP ligand and the porphyrin plane is 54.12 º in previously reported Zr_6-based PCN-222. In contrast, the four peripheral benzene rings are perpendicular to the porphyrin in PCN-221, comparable to those in other reported porphyrinic MOFs.[86-89] Each TCPP ligand connects four Zr_8 clusters in a 4-connected mode, in which each carboxylic acid coordinates one Zr_8 cluster (Figure 11a). Similar to that of the Zr_6 cluster in UiO-type structures, each edge of the Zr_8 cube is bridged by one carboxylate from a TCPP ligand, so each Zr_8 cluster is 12-connected and coordinated by twelve TCPP ligands. Such connectivity leads to a three-dimensional (3D) network, exhibiting a very rare (4,12)-connected **ftw** topology with point symbol of $\{4^{36}\cdot6^{30}\}\{4^4\cdot6^2\}_3$ (Figure 11b).[90-92] The structure features two types of polyhedral cages with pore openings of ~0.8 nm. The small cage, a slightly distorted octahedron with a cavity diameter of ~1.1 nm, comprises two Zr_8 clusters in the axial sites and four TCPP ligands in the equatorial plane (Figure 11d). The other cage, a cube with edge length of ~2.0 nm, is surrounded by eight Zr_8 clusters at the vertices and six TCPP ligands at the faces (Figure 11e). The solvent-accessible volume in PCN-221 is 70.5% calculated using the PLATON routine.[93] This provides sufficient space for solvent molecules and charge-balancing counter-ions for the framework, which are common in previously reported MOFs.[94-95]

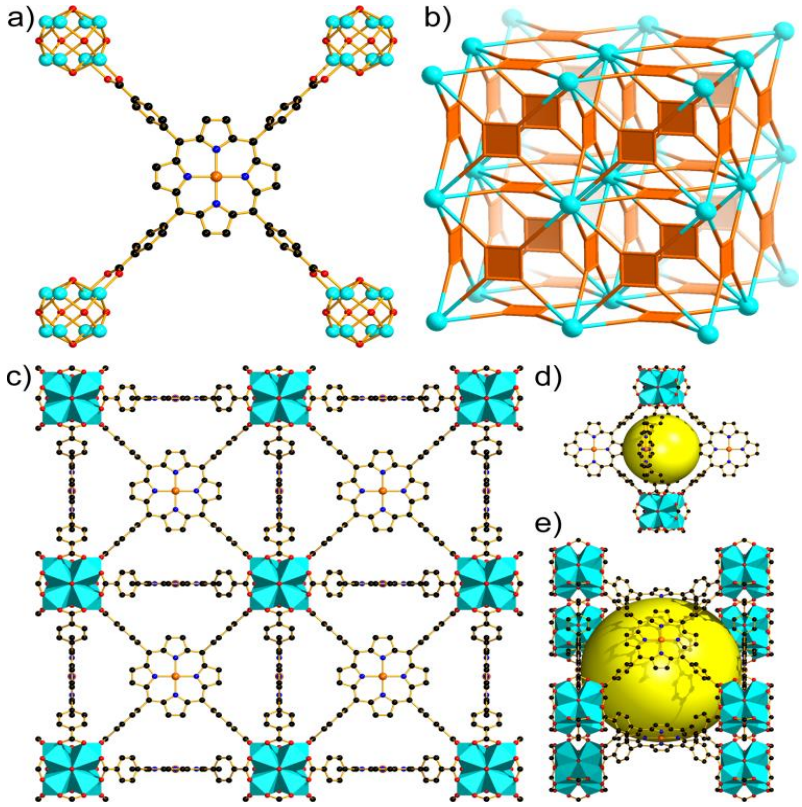

Figure 11. (a) The Cu centered-TCPP ligand is 4-connected to four Zr_8 clusters. The four peripheral benzene rings are perpendicular to the porphyrinic ring in the ligand. (b) Schematic representation of the (4,12)-connected 3D network of PCN-221 with ftw topology, in which Zr_8 cluster and TCPP ligand are simplified as purple dodecahedral and green square nodes, respectively. (c) View of the 3D structure of PCN-221 along the a-axis. (d) Octahedral and (e) cubic cages comprised Zr_8 clusters and organic linkers in PCN-221. The space inside a cage is highlighted with a yellow sphere. The ZrO_6 polyhedra in (c-e) are shown in purple. Color Scheme: Zr-purple, C-dark gray, O-red, N-blue, Cu-green. H atoms are omitted for clarity.

The permanent porosity of PCN-221 has been confirmed by nitrogen adsorption experiments at 77 K (Figure 12). The typical type I isotherms suggest microporosity. The N_2 uptakes range from 450 to 650 cm^3/g (STP) and experimental pore volumes are in the range of 0.6-0.8 cm^3/g depending on what metal is coordinated by the porphyrin in PCN-221. The Brunauer-Emmett-Teller (BET) surface areas are 1936, 1549, and 1532

m^2/g for Zr-PCN-221(no metal), Zr-PCN-221(Fe), and Hf-PCN-221(Co), respectively. These values are very high for porphyrinic MOFs, as the porosity is hardly preserved upon removal of guest solvent molecules in other reported porphyrinic MOFs.[96-98] The H_2 uptakes for Zr-PCN-221(no metal), Zr-PCN-221(Fe) and Hf-PCN-221(Co) are 1.73, 1.71 and 1.62 wt% at 1 atm and 77 K, which are comparable to those of other MOFs and at the high end among those for Zr- and Hf-MOFs. The slightly lower isosteric heat of H_2 adsorption for Zr-PCN-221(no metal) than those of the other two MOFs can be attributed to the absence of exposed porphyrinic metal centers .

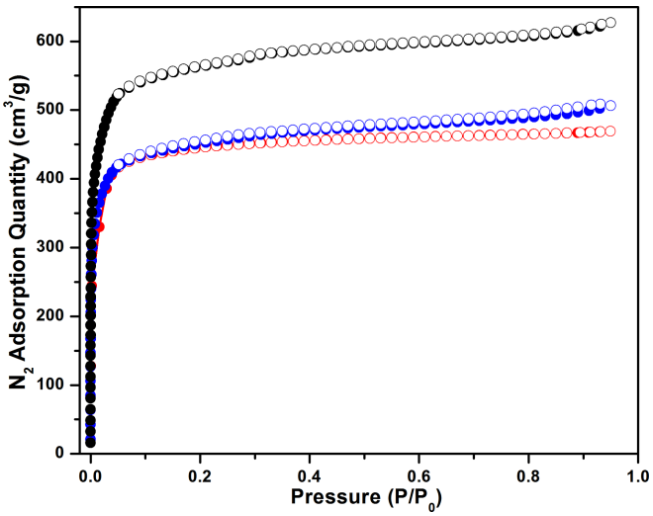

Figure 12. N_2 sorption isotherms for Zr-PCN-221(no metal) (black curves), Zr-PCN-221(Fe) (blue curves), and Hf-PCN-221(Co) (red curves).

The metalloporphyrin moiety within PCN-221 makes it an ideal platform for catalytic studies. Selective oxidation of cyclohexane to cyclohexanone (K) and cyclohexanol (A), key intermediates in the production of Nylon-6 and Nylon-6,6, continues to be a key and challenging process. Industrially, the process for cyclohexane oxidation was carried out at 423-433 K over cobalt-based homogeneous catalysts,

leading to about 4% conversion and 70-85% selectivity to K/A oil.[99] Herein, Zr-PCN-221(Fe) was explored as a heterogeneous catalyst for cyclohexane oxidation in the presence of tert-butyl hydroperoxide (TBHP) as an oxidant at 65 ℃ under neat conditions. Based on the assumption that each mole of cyclohexanone is produced by consuming two equivalents of oxidants and each mole of cyclohexanol is generated by consuming one equivalent of oxidant, the reaction proceeds very quickly and completes in about 11 hours, when the reaction products are produced in almost stoichiometric amount with TBHP utilization efficiency of close to 100%. The selectivity is mainly toward cyclohexanone (86.9%) and a small amount of cyclohexanol (5.4%) is also produced, while no other oxidation products are found (Figure 13). To the best of our knowledge, the total yield of K/A oil and a turnover number of 18 are comparable to or higher than those of other MOF-based or conventional molecular sieve catalysts.[100-102] This high reactivity and selectivity can be attributed to the high-density of accessible active porphyrinic iron(III) centers within the porous framework.

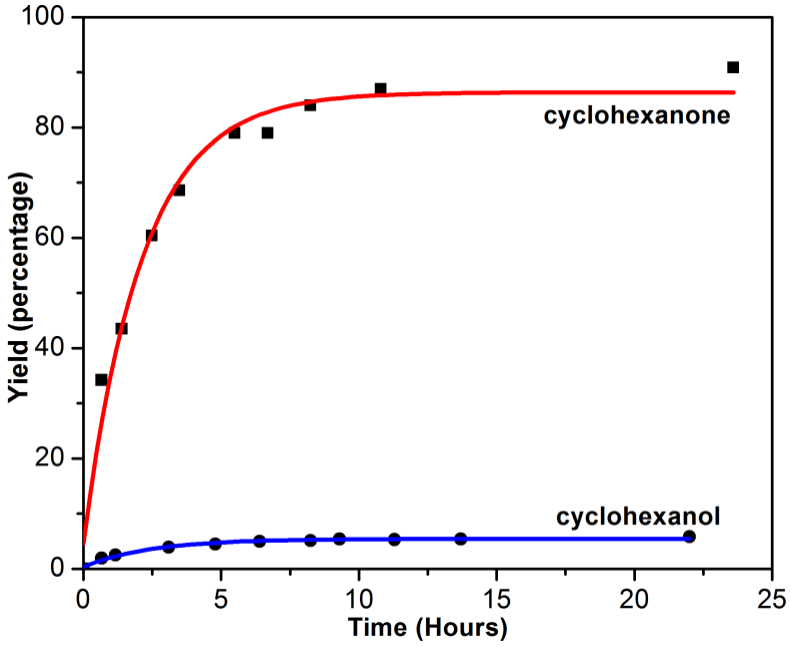

Figure 13. Catalytic oxidation of cyclohexane over Zr-PCN-221(Fe) at 65 ℃ under neat conditions. The yields are calculated on the basis of TBHP. The curves are to guide the eye and not fit to the data.

2.2.4 Conclusions

In summary, unprecedented Zr_8 and Hf_8 clusters have been prepared and structurally characterized for the first time in extended networks, although the molecular forms of these clusters are still unknown. Each cluster coordinates twelve TCPP ligands giving rise to highly porous 3D frameworks of PCN-221 containing two types of cavities with diameters of 1.1 and 2.0 nm. The MOFs exhibit high surface area and interesting gas sorption properties. With accessible active porphyrinic iron(III) centers, PCN-221 catalyzes the oxidation of cyclohexane with very high selectivity toward ketone and alcohol products. The discovery of Zr_8 and Hf_8 clusters not only greatly enriches cluster science, but also expands the structural diversity of Zr- and Hf-based MOFs.

2.3 Construction of an Ultrastable Porphyrin Zr Metal-organic Framework through Linker Elimination

2.3.1 Introduction

Metal-organic frameworks (MOFs), an emerging class of organic-inorganic hybrid porous solids, have attracted a great deal of research interest for their potential applications, especially in gas storage and separation, catalysis, drug delivery, and sensing.[30-35] Moreover, the tunable nature of MOFs offers a unique advantage over other porous materials in that functional moieties can be readily introduced into the frameworks by either ligand design or post-synthetic modification. Consequently, the incorporation of different functionalities into MOFs has been widely investigated for various applications.[38-42]

Metallo-porphyrins exhibit excellent catalytic activities. Immobilization of porphyrin catalysts in polymers and zeolites has been extensively explored. With uniform but tunable pore sizes, MOFs provide a special platform for the effective utilization of the porphyrinic catalytic centers. Recently, porphyrin derivatives have been introduced into MOFs by either linker extension or encapsulation.[43-53] Catalytic activities and optical properties have been investigated in such porphyrinic MOFs. However, most of these MOFs are constructed by the combination of soft acids (low-oxidative transition metal ions) and hard bases (carboxylates), and consequently have relatively weak chemical stabilities. Hence, the applications of porphyrinic MOFs in catalysis have been restricted to mild reaction conditions.

To improve the stability of porphyrinic MOFs and to facilitate the study of their catalytic activities, a chemically stable MOF is a prerequisite. So far, very few MOFs have high chemical stability, most of which are based on either high-oxidation-state metal species with carboxylate linkers or nitrogen containing ligands with divalent metals, while Zr (IV)-based MOFs, an example of the former, are relatively less explored.[67-74] We are particularly interested in Zr-based MOFs because the strong interaction between Zr(IV) and carboxylate will make the resultant MOFs chemically stable; moreover, the modulating method in Zr-MOF synthesis makes their single crystals, suitable for structure determination, readily accessible.

Combing the versatility of metalloporphyrins and the stability of Zr-carboxylate MOFs, we have reported an iron-porhpyrin zirconium MOF, PCN-222(Fe) (PCN stands for porous coordination network), which exhibits extraordinary stability and peroxidase-like catalytic activity. In UiO-66, the Zr_6 cluster binds twelve carboxylates and exhibits O_h symmetry. Notably, in PCN-222, four of the surrounding carboxylate linkers connected to the Zr_6 cluster are replaced by hydroxyl groups. As a result, the O_h symmetry of the Zr_6 cluster is reduced to one of its subgroups, D_{4h}. Fewer carboxylate linkers on the Zr_6 means more space for catalysis is available. Moreover, the introduction of OH groups improves the hardness of the Zr_6 core, which further strengthens the bonding between the bridging ligands and the Zr_6 units. Therefore, the PCN-222 series shows ultrahigh chemical stability. Such a linker-elimination strategy in the Zr_6 cluster inspires us to go further. By adjusting the reaction conditions, the coordination environment around the Zr_6 cluster could be tuned. MOFs containing novel

Zr_6 clusters, which binds less than eight linkers with symmetry of another subgroup of O_h could be obtained, which would allow us to construct new porphyrinic zirconium MOFs with new structures, high stability, and unexplored catalytic activity.

Bearing this in mind, by carefully varying the ratio of starting materials and the amount of modulating reagent, we have obtained a new series of porous porphyrinic zirconium MOFs, denoted PCN-224 based on a Zr_6 cluster with D_{3d} symmetry and MTCPP ligand (TCPP = tetrakis(4-carboxyphenyl)porphyrin). PCN-224 possesses three dimensional (3-D) channels as large as 19Å and exhibits high stability over a wide range of pH in aqueous solution. Interestingly, PCN-224(Co) shows very high efficiency as a heterogeneous catalyst for the CO_2 and epoxide coupling reaction with good recyclability.

2.3.2 Experimental Section

Synthesis of PCN-224(No metal) $ZrCl_4$ (30 mg), H_2TCPP (10 mg) and 400mg benzoic acid in 2 mL of DMF were ultrasonically dissolved in a Pyrex vial. The mixture was heated in 120 ℃ oven for 24 h. After cooling down to room temperature, cubic dark purple crystal was harvested by filtration (10 mg, 71% yield). FTIR (KBr, cm^{-1}): 1664 (vs), 1601 (m), 1551 (m), 1497 (w), 1406 (vs), 1251 (m), 1179 (w), 1087 (s), 1022 (w), 974 (w), 808 (m), 772 (m), 728 (s), 662 (vs). Anal. calcd. (%) for PCN-224 (No metal): C, 44.04; H, 2.62; N, 4.28%. Found: C, 50.34; H, 3.10; N, 3.64%.

Synthesis of PCN-224 (Ni) $ZrCl_4$ (10 mg), Ni-TCPP (10 mg) and 250mg benzoic acid in 2 mL of DMF were ultrasonically dissolved in a Pyrex vial. The mixture was

heated in 120 ℃ oven for 24 h. After cooling down to room temperature, dark red cubic crystal was harvested by filtration (10 mg, 70% yield). FTIR (KBr, cm^{-1}): 1661 (s), 1604 (m), 1548 (w), 1411 (vs), 1358 (s), 1254 (w), 1182 (w), 1108 (m), 998 (s), 802 (m), 772 (s), 716 (vs), 659 (vs). Anal. calcd. (%) for PCN-224(Ni): C, 42.22; H, 2.36; N, 4.10%. Found: C, 45.43; H, 3.13; N, 4.48%.

Synthesis of PCN-224(Co) $ZrCl_4$ (30 mg), CoTCPP (10 mg) and benzoic acid (400 mg) in 2 mL of DMF were ultrasonically dissolved in a Pyrex vial. The mixture was heated in 120 ℃ oven for 24 h. After cooling down to room temperature, dark red cubic crystal was harvested (10 mg, 70% yield). FTIR (KBr, cm^{-1}): 1664 (m), 1607 (m), 1548 (m), 1402 (vs), 1349 (m), 1212 (w), 1182 (w), 1096 (w), 995 (s), 835 (w), 799 (w), 772 (s), 713 (vs), 657 (vs). Anal. calcd. (%) for PCN-224(Co): C, 42.21; H, 2.36; N, 4.10%. Found: C, 46.74; H, 2.57; N, 3.73%.

Synthesis of PCN-224(Fe) $ZrCl_4$ (30 mg), FeTCPPCl (10 mg) and benzoic acid (400 mg) in 2 mL of DMF were ultrasonically dissolved in a 4 mL Pyrex vial. The mixture was heated in 120 ℃ oven for 12 h. After cooling down to room temperature, dark brown square and needle shaped crystals (PCN-222) mixture were harvested. FTIR (KBr): ν= 3381 (m), 2952 (w), 1705 (w), 1601 (s), 1549 (s), 1411 (vs), 1340 (s), 1182 (m), 1003 (s), 871 (w), 809 (m), 776 (m), 723 (s) cm^{-1}. Anal. calcd. (%) for PCN-222(Fe): C, 42.12; H, 2.30; N, 4.08%. Found: C, 42.59; H, 3.12; N, 4.15%.

Stability Test Around 500mg of freshly made PCN-224(Ni) sample was separated into 5 different vials containing 10mL of 1M HCl, pH=1, pH=10, pH=11 aqueous solutions and pure water. After immersion in those solutions for 24h, PCN-224(Ni)

samples were centrifuged and washed with acetone for 3 times, them dried on the vacuum lime and measured N_2 adsorption on ASAP 2420. The filtrate of each treatment was compared with 0.5mg (1% of ligands containing in MOF sample) Ni-TCPP ligand aqueous solution.

Sample Activation Process Before gas sorption experiment, as-synthesized PCN-224 (~70 mg) samples were washed with DMF for three times and once with acetone, and then immersed in acetone for over 12 h. Afterwards, the mixture was centrifuged. After the removal of acetone by decanting, the samples were activated by drying under vacuum for 6 h, then was dried again by using the 'outgas' function of the adsorption instrument for 12 h at 80 ℃ prior to gas adsorption/desorption measurement.

Catalysis PCN-224(Co) (45.7 mg, 0.0321 mmol), tetrabutylammonium chloride (19.9 mg, 0.0716 mmol) and propylene oxide (2.50 mL, 35.7 mmol) were added to a 12 mL autoclave reactor which had previously been dried for 6 h. The reactor was pressurized to 2 MPa with CO_2 and maintained at 100 ^{o}C. After 4h, the reactor was put into ice bath for 10 min and depressurized, a small aliquot was taken to be analyzed by 1H NMR to calculate the conversion of propylene oxide. The reaction solution was centrifuged to recover catalyst for next cycle, and the supernatant was collected. The process was repeated using recovered catalyst, which had been dried in vacuo for 6h.

2.3.3 Results and Discussion

Single-crystal X-ray diffraction studies have revealed that PCN-224 crystalizes in space group *Im*-3*m*. Its framework consists of Zr_6 clusters linked by the square planar

TCPP ligands. Each $Zr_6(OH)_8$ core, in which all of the triangular faces in a Zr_6-octahedron are capped by μ_3-OH groups (Figure 14), is connected to six TCPP ligands.

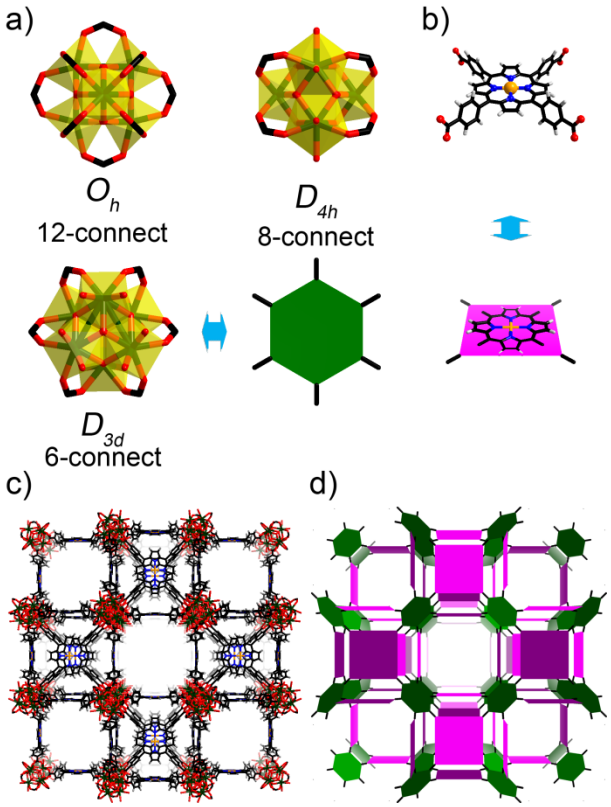

Figure 14. Crystal structure, structural components, and underlying network topology of PCN-224(Ni). (a)The 12-connected O_h symmetric Zr_6 cluster in UiO-66, 8-connected D_{4h} symmetric Zr_6 in PCN-222 and 6-connected D_{3d} symmetric Zr_6 in PCN-224. (b) Tetratopic TCPP ligands (violet square) with twisted dihedral angles generate a framework with 3-D nanochannels (c, d). Colour scheme: Zr, green spheres; C, grey; O, red; N, blue; Ni, orange; and H, white.

Different from the 12-connected Zr_6 cluster observed in the UiO-66 and 8-connected Zr_6 cluster in PCN-222, only six edges of the Zr_6 octahedron are bridged by carboxylates from TCPP ligands in PCN-224. Viewed along the S_6 axis, each triangle at the top and bottom of the Zr_6 octahedron is occupied by six terminal OH (or H_2O)

groups (two on each Zr) giving rise to a D_{3d} symmetric Zr_6 cluster (Figure 14). Moreover, the average dihedral angle between a phenyl ring and the porphyrin centre of the ligand, 76.39 °, is also different from that in PCN-222. With the reduced number of carboxylate linkers, the new Zr_6 cluster allows more free space, which eventually leads to the formation of 3-D channels. The solvent-accessible volume in PCN-224 reaches 78.9% calculated using the PLATON routine (1.8 Å probe). As described above, the cluster and ligand can be viewed as 6- and 4-connected node respectively. Thus topologically, the framework can be classified as a 3D (4,6)-connected *she* net with the point symbol $(4^4 \cdot 6^2)_3(4^6 \cdot 6^6 \cdot 8^3)_2$ (Figure 14d).

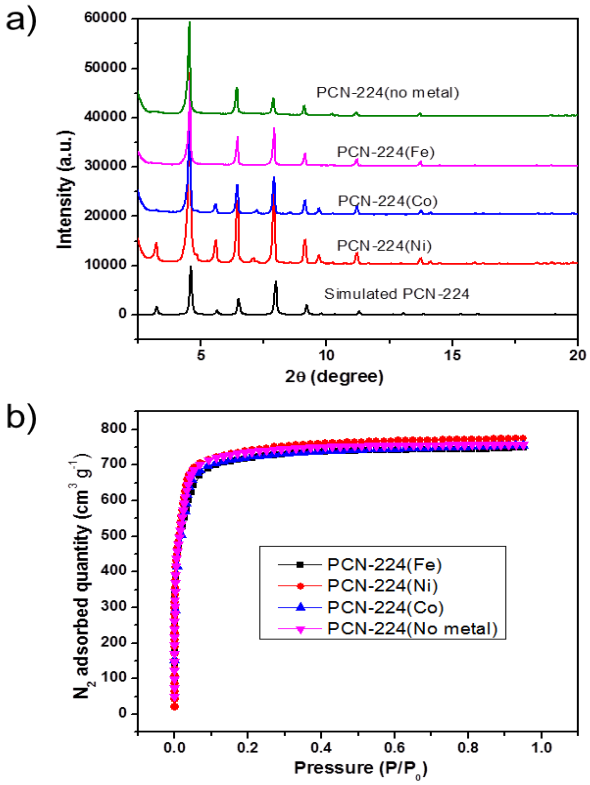

Figure 15. (a) Powder XRD patterns for simulated and experimental PCN-224 samples. (b) N_2 adsorption isotherm of PCN-224 series at 77 K, 1 atm.

The porosity of PCN-224 series has been evaluated by nitrogen adsorption studies at 77 K. A N_2 uptake of 790 cm^3 g^{-1} (STP) and Brunauer-Emmett-Teller (BET) surface area of 2600 m^2 g^{-1} have been obtained for PCN-224(Ni). The calculated total pore volume of PCN-224 is as high as 1.59 cm^3 g^{-1}. To the best of our knowledge, the BET surface area of PCN-224(Ni) represents the highest among all reported porphyrinic MOFs. Other PCN-224 MOFs with different metal centres in the porphyrin also show similar N_2 adsorption isotherms and surface areas (Figure 15a and 15b).

With 3-D channels of 1.9 nm, surprisingly, PCN-224 exhibits very high chemical stability. PCN-224 samples of the same batch were soaked in pH=0 to pH=11 aqueous solution for 24h. After that, those samples were centrifuged and reactivated. Powder X-ray diffraction (PXRD) patterns suggest that PCN-224 retains good crystallinity upon these treatments (Figure 16a). Such a wide range of pH stability is even better than our previously reported PCN-222. The N_2 adsorption isotherms of those samples show the perfect maintenance of the porosity, further demonstrating the framework stability (Figure 16b). Moreover, almost no dissolved ligand was detected in the filtrate after those chemical treatments (Figure 16c). Such good chemical stability has rarely been observed in other reported porphyrinic MOFs, or even most reported MOFs.

With 3-D open channels constructed from multifunctional porphyrin moieties, PCN-224(M) exhibits high chemical and thermal stability and meets most of the prerequisites as an ideal platform for heterogeneous catalysis: First, with free porphyrin as the building block, PCN-224 allows the convenient insertion of all kinds of metals for different types of catalysis. Second, as an assembly of metalloporphyrins, PCN-224(M)

provides evenly distributed catalytic centres, different from metalloporphyrins encapsulated in porous materials. Third, the 3-D nano-channels allow fast diffusion and transportation of substrates and products. Therefore, the catalytic efficiency could be highly improved compared to MOFs with smaller pores.

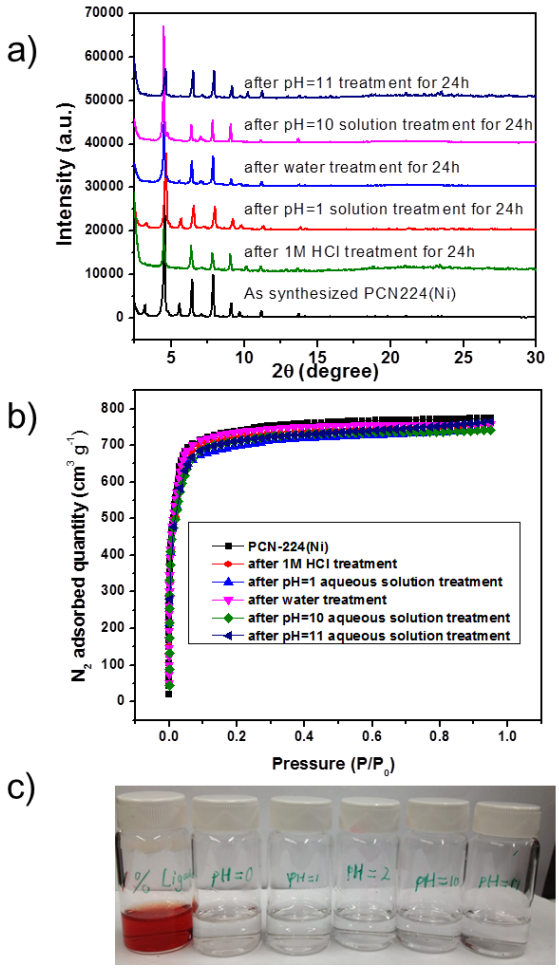

Figure 16. (a) PXRD patterns and (b) N_2 adsorption isotherms for PCN-224(Ni), showing the framework stability of PCN-224(Ni) upon treatments in 1 M HCl, pH=1, water, pH=10 and pH=11 aqueous solutions. (c) Comparison between 1mg dissolved ligand and the corresponding solutions after the stability test.

Last, excellent stability, especially stability over a wide pH range, allows the application of PCN-224(M) as a reusable heterogeneous catalyst under harsh reaction conditions. With the most important advantage of heterogeneous catalysis, which is that it is easy to separate the catalyst from the reaction mixture, catalyst efficiency could be maintained and contamination from catalyst decomposition could be avoided.

Being a main cause of the greenhouse effect, CO_2 is also an abundant, cheap, and non-toxic renewable C1 resource. The development of efficient catalytic processes for CO_2 transformation into desirable, economically useful products is therefore of great interest. In particular, cyclic carbonates are in an important class of compounds that can be used in various areas, such as polar aprotic solvents, degreasers, electrolytes in lithium ion batteries, as well as intermediates for linear dialkyl carbonate synthesis.[103-104]

Since metalloporphyrins are commonly used catalysts for the CO_2 and epoxide coupling reaction, herein, we evaluated PCN-224(Co) as a heterogeneous catalyst for such a purpose (Figure 17a). In a typical reaction, PCN-224(Co) (32.1 μmol), tetrabutylammonium chloride (71.6 μmol), and propylene oxide (35.7mmol) were added into an autoclave reactor. The reactor was pressurized to 2 MPa with CO_2 and maintained at 100 ^{o}C for 4h. After that PCN-224(Co) was recovered and reused in the next run with the same conditions. Even after three consecutive catalysis runs, the catalyst was demonstrated to be highly crystalline by PXRD (Figure 17b), which indicates the reusability of PCN-224(Co) as a heterogeneous catalyst. The resulting

solution of each trial was analyzed by ^{1}H NMR to calculate the conversion of propylene oxide (Table 5).

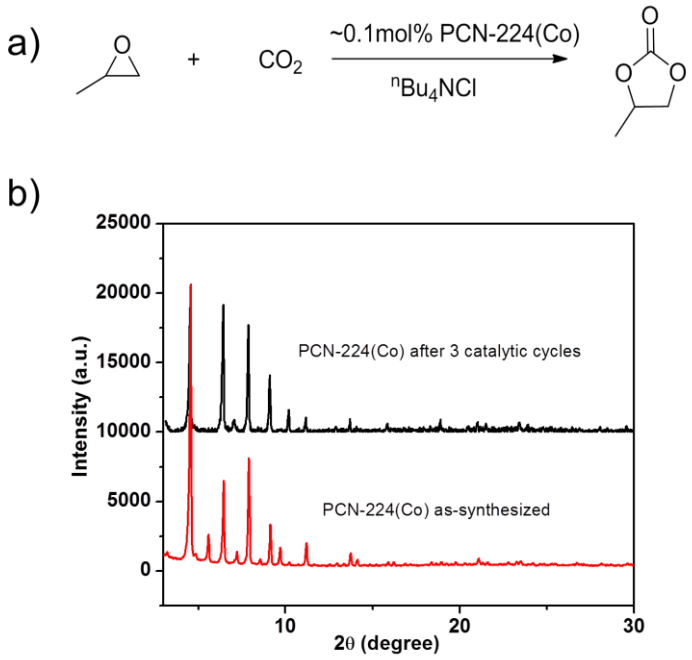

Figure 17. (a) CO_2 and propylene oxide coupling reaction catalyzed by PCN-224(Co) and (b) PXRD patterns of PCN-224(Co) as-synthesized sample (red) and after 3 catalytic cycles (black).

Table 5. CO_2/propylene oxide coupling reaction catalysed by PCN-224(Co)

Run	Conversion(%)	TON[a]	TOF (h^{-1})[b]
1	42	461	115
2	33	419	104
3	39	518	129

[a] moles of propylene oxide consumed/ moles of Co, [b] moles of propylene oxide consumed/ moles of Co/reaction time

Compared to the result from the homogeneous cobalt-porphyrin catalyst,[11] PCN-224(Co) shows similar heterogeneous catalytic activity, which implies that the reaction

is not under diffusion control, thanks to the 3-D nano-channels of PCN-224. Despite this interesting catalytic activity, the advantage of MOFs as heterogenous catalysts can be further explored. For instance, normally the CO_2 pressure should remain high to make desirable portions dissolve in solution. However, with a MOF as a heterogeneous catalyst, the reaction can be conducted in the gas phase, in which CO_2 and epoxide gas can diffuse to the catalytic centre more easily than in the liquid phase without any solubility concern. Moreover, with the gas phase starting materials, catalysed by solid MOFs, generating liquid products, the separation process would be significantly simplified.

2.3.4. Conclusions

In conclusion, we have synthesized a series of new porphyrinic zirconium MOFs, PCN-224(M), by adopting a linker eliminations approach. The PCN-224(M) series exhibits high surface area and 3-D open channels, in particular, PCN-224(Co) was demonstrated to be a reusable heterogeneous catalyst for the CO_2 epoxide coupling reaction.

2.4 A Highly Stable Porphyrinic Zirconium Metal-Organic Framework with shp-a Topology

2.4.1 Introduction

Due to the readily adjustable nature of MOFs, one of the most convenient approaches to introduce functional moieties into the framework is to construct MOFs with those moieties or their derivatives as building units. [1-5] As a solid state material with periodic structure and porosity, consequently, MOFs make those functional moieties well dispersed with extremely high accessibility, which will result in effective utilization of each individual unit. In other words, homogenous arrangement and the accessibility of functional moieties, which is one main advantage of homogenous liquid or gas systems, are almost completely realized in a heterogenous solid state material. Moreover, once stable MOFs are formed, they can be used under different media without concern for solubility, which tremendously diminishes the synthetic effort in some homogeneous catalytic systems where solubility and their working environment conflicts.

Porprhyrin derivatives have been substantially explored as organic linkers in MOFs due to their multifunctionality.[42-55] As one of the most frequently found species in biological systems, porphyrin derivatives can be used as light harvesting reagents, anti-cancer drugs, catalysts, sensors, nonlinear optical materials and DNA-binding or cleavage agents. After being introduced into MOFs, the dimerization of some porphyrinic species was eliminated. Meanwhile, as highly conjugated large molecules, most artificial porphyrinic species suffer solubility problems under either physiological

conditions or unreactive organic solvents (mostly nonpolar). When immobilized into MOFs, porphyrinic species can be used in any media without considering their solubility. Despite that, the chemical stability of porphyrinic MOFs severely restricted wide applications for a long period when relatively soft Lewis acidic metal species were used as nodes. [67-74] The practice of using hard Lewis acidic species, such as Zr^{4+} and Al^{3+}, has successfully expanded the range of working environments for porphyrinic MOFs, especially in aqueous media, and thus greatly diversified the application of those MOFs. Porphyrinic Zr-MOFs are outstanding representatives with excellent chemical stability under harsh conditions for novel applications in the MOF field, such as biomimetic catalysis and pH sensing. The variation of connecting numbers and symmetry provides many topological possibilities to form different frameworks with the same TCPP (tetrakis(4-carboxyphenyl) porphyrin) linker and Zr_6 node. These porphyrinic Zr-MOFs obtained from variation of synthetic conditions exhibit not only different pore sizes and shapes, but also different chemical stabilities, which offer eligible candidates for different applications. For example, the mesoporous PCN-222 has extremely high stability under acidic conditions, which makes it an ideal candidate for incorporation of large substrates or being applied under acidic environments. In comparison, PCN-224 has worse stability under acidic conditions but survives much better under basic conditions. Although there are already several different porphyrinic Zr-MOFs reported, the variable connectivity and symmetry of the Zr_6 cluster still provides topological possibilities to obtain more frameworks with different applicable properties. Therefore,

exploration of novel porphyrinic Zr-MOFs might further expand the study of novel applications for MOFs.

2.4.2 Experimental Section

Synthesis of PCN-223(Fe) Method 1 $ZrCl_4$ (7 mg), Fe(III)-TCPPCl (10 mg) and acetic acid (1.1mL) in 2 mL of DMF were ultrasonically dissolved in a 4 mL Pyrex vial. The mixture was heated in 120 ℃ oven for 12 h. After cooling down to room temperature, dark brown crystals were harvested by filtration.

Synthesis of PCN-223(Fe) Method 2 $ZrCl_4$ (10 mg), Fe(III)-TCPPCl (10 mg) and benzoic acid (250 mg) in 2 mL of DMF were ultrasonically dissolved in a 4 mL Pyrex vial. The mixture was heated in 120 ℃ oven for 12 h. After cooling down to room temperature, dark brown needle shaped crystals were harvested by filtration.

Synthesis of PCN-223(No) Method 1 $ZrCl_4$ (7 mg), H_2TCPP (10 mg) and acetic acid (0.7mL) in 2 mL of DMF were ultrasonically dissolved in a 4 mL Pyrex vial. The mixture was heated in 120 ℃ oven for 12 h. After cooling down to room temperature, dark needle shaped crystals were harvested by filtration.

Synthesis of PCN-223(No) Method 2 $ZrCl_4$ (10 mg), H_2TCPP (10 mg) and benzoic acid (250 mg) in 2 mL of DMF were ultrasonically dissolved in a 4 mL Pyrex vial. The mixture was heated in 100 ℃ oven for 12 h. After cooling down to room temperature, dark needle shaped crystals were harvested by filtration.

Single-Crystal X-ray Crystallography A brown spindle crystal was taken from the mother solution, transferred to oil and mounted into a loop for single crystal X-ray

data collection. Diffractions were measured on a Bruker Smart Apex diffractometer equipped with a Mo-Kα sealed-tube X-ray source (λ = 0.71073 Å, graphite monochromated) and a cooling device (110 K). The data frames were recorded using the program APEXII and processed using the program *SAINT* routine within APEXII. The data were corrected for absorption and beam corrections based on the multi-scan technique as implemented in *SADABS*. The structures were solved by direct method using *SHELXS* and refined by full-matrix least-squares on F^2 using *SHELXL* software.

We started solving this structure with cubic crystal system. $P\ \bar{3}$ showed lowest CFOM factor (8.94). After checking the heavy atom moiety in *PLATON* addsym unit, it was suggested that the correct space group should be upgraded to *P*6/*mmm*. But it was very difficult to give a normal distance for the porphyrin ring, as failed to solve the structure. After fixing geometry in the space group of $P\ \bar{3}$ and rechecking the symmetry, we found *P*6/*m* works well. Because the Zr_{18} cluster shown in the structure is a 3-fold disorder of Zr_6 cluster, we manually change the occupancy (multiply 1/3) for each Zr atoms.

For the refinements, all non-hydrogen atoms were refined with anisotropic displacement parameters. Those with enormous thermal ellipsoids were refined with the help of EADP restrains on each ligand to clear the warnings about non-positive definite matrices. Organic hydrogen atoms were located in calculated positions with isotropic displacement parameters set to $1.2 \times U_{eq}$ of the attached atoms. The solvent molecules were highly disordered, and attempts to locate and refine the solvent peaks were unsuccessful.

Table 6. Crystal data and structure refinements for PCN-223.

Compound PCN-223	
Formula	$Zr_6\ C_{144}\ H_{72}\ N_{12}\ O_{24}\ Fe_3\ Cl_3$
Fw	3175.36
Shape	Spindle
Crystal system	Hexagonal
Space group	*P*6/*m*
a (Å)	21.43(3)
b (Å)	21.43(3)
c (Å)	16.89(2)
α (°)	90.00
β (°)	90.00
γ (°)	120.00
V (Å^3)	6717(15)
Z	1
T (*K*)	110(2)
$d_{calcd.}$ (g/cm^3)	0.785
μ(mm^{-1})	0.447
F(000)	1581
θ_{max} [deg]	16.72
Completeness	99.2%
Collected reflections	13030
Unique reflections	1315
Parameters	89
Restraints	28
R_{int}	0.1911
*R*1 [I > 2σ(I)]	0.1331
*wR*2 [I > 2σ(I)]	0.3131
*R*1 (all data)	0.1922
*wR*2 (all data)	0.3473
GOF on F^2	1.013
$\Delta\rho_{max}$/ $\Delta\rho_{min}$ [e·Å^{-3}]	0.753 / -0.548

2.4.3 Results and Discussion

Through a kinetically controlled process, we synthesized a new porphyrinic Zr-MOF (PCN-223). PCN-223 contains the unprecedented D_{6h} symmetric twelve-connected Zr_6 cluster, which gives rise to the **shp-a** network, of which this is the first example in a MOF. PCN-223 has uniform one dimensional (1-D) triangular channels with porphyrinic walls. With the highest connectivity among the Zr-MOFs, PCN-223 shows excellent stability in aqueous environments with pH values ranging from 0 to 10. We generated a naked cationic iron(III) porphyrin center in PCN-223(Fe), which catalyzed the hetero-Diels−Alder reaction between unreactive aldehydes and a diene with very high yield and excellent recyclability.

The fully bridged Zr_6 [$Zr_6O_4OH_4(COO)_{12}$] cluster reported in UiO-66 is a twelve-connected O_h symmetric node, which both symmetrically and in connectivity matches with the four-connected D_{4h} symmetric TCPP node. The combination of these two nodes gives rise to an **ftw-a** network. However, the relative position between the two nodes is not compatible with that in the **ftw-a** network unless a relatively high energy conformation is adopted for each node. As a result, both the connectivity and the symmetry of the Zr_6 SBU always decrease to form other networks with the symmetry reduced TCPP ligands with a variety of dihedral angles between the central and peripheral rings. Despite the structural differences, the Zr porphyrinic MOFs are obtained under very similar reaction conditions, suggesting the lack of a thermodynamically dominant phase, providing opportunities to explore more new structures by tuning the synthetic conditions. By using less competing reagent (benzoic

acid or acetic acid), which could accelerate the formation of MOFs while maintaining the crystallinity, we successfully obtained a kinetically favored phase of porphyrinic zirconium MOFs, PCN-223.

Solvothermal reactions of $ZrCl_4$, TCPP (free base or Fe coordinated) and the competing (modulating) reagent in DMF give rise to spindle-shaped crystals of PCN-223. Single crystal X-ray diffraction reveals that PCN-223(Fe) crystallizes in the *P6/m* space group. Originally, a twelve-connected Zr_{18} cluster was observed, which has never been reported in either Zr carboxylates or Zr-MOFs (Figure 18a). However, the shortest Zr···Zr distance in the Zr_{18} cluster is 2.45 Å, which is much shorter than that in the Zr_6 cluster (~2.70 Å) or other reported zirconium carboxylates. Considering Zr_6 is the absolutely dominant inorganic node in all the reported Zr-MOFs, we tried to confirm the discovery of this unusual Zr_{18} cluster by measuring the ratio between Zr and the TCPP linker. According to the result of energy dispersive X-ray spectroscopy (EDX), the Zr to Fe ratio in PCN-223(Fe) was determined to be 2:1, which suggests a twelve connected Zr_6 cluster instead of Zr_{18}. To rationalize this result, we separated the Zr_{18} cluster into three Zr_6 clusters oriented in different directions, which are periodically arranged in the framework and appear as a Zr_{18} cluster through crystallographic disorder (Figure 18a). In each individual Zr_6 cluster, there are only eight carboxylates bridging adjacent Zr atoms while the other four chelating single Zr atoms (Figure 18b). In Zr-MOFs, this is a novel building unit different from the conventional twelve-connected Zr_6 cluster in UiO-66, in which all the carboxylates bridging adjacent Zr atoms (Figure 18b). After topological simplification (only carbon atoms on the carboxylates are considered), each twelve

connected Zr_6 cluster in PCN-223 exhibits D_{6h} symmetry and overall gives rise to the first **shp-a** topology among all reported MOFs (Figure 19). Along the c-axis, PCN-223 has uniform triangular 1-D channels of 12 Å; this arrangement is equivalent to separating the hexagonal channel in PCN-222 by six more TCPP linkers and an extra Zr_6 node (Figure 19).

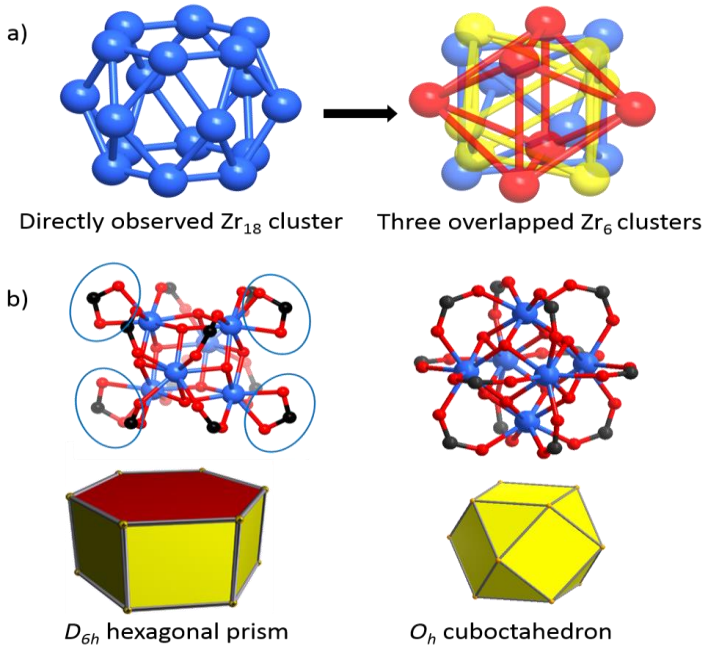

Figure 18. (a) Directly observed Zr_{18} cluster (left) and overlapping Zr_6 clusters(right), each exhibiting partial crystallographic occupancy. (b) The unusual twelve-connected Zr_6 cluster (left) and the conventional twelve-connected O_h symmetric Zr_6 cluster

It is worth noting that such a shp-a network is one of the three predicted edge-transitive (4,12)-c nets by O'Keeffe and coworkers.[105] Interestingly, another (4,12)-c net, ftw-a, has also been realized in porphyrinic Zr-MOFs (MOF-525 and PCN-221). In comparison, MOF-525 was obtained with a much higher acid to ligand ratio and a longer

reaction time, suggesting that PCN-223 may be more kinetically favored. Compared with the **shp-a** net, the ftw-a net shows more a regular arrangement (higher symmetry). To obtain the latter requires a longer time for the assembly and crystal growth procedures. Moreover, less or weaker competing reagent is needed for PCN-223 compared to PCN-222, which not only kinetically accelerates MOF growth but also facilitates the formation of an entropically favored product.

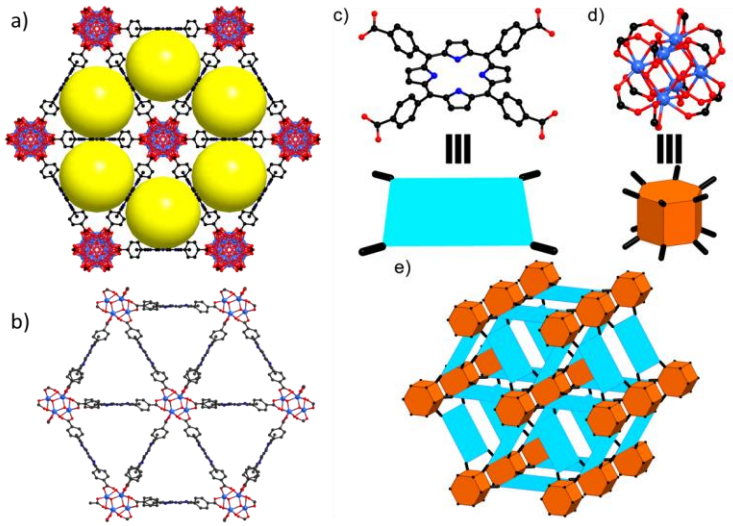

Figure 19. PCN-223 viewed along c axis with uniformed triangular 1-D channels observed in the structure (a) and after removing disorder (b). Topology analysis of PCN-223(c-e).

In order to assess the porosity of PCN-223(No metal and Fe), we performed N_2 sorption measurements at 77 K (Figure 20b). Both PCN-223(Free base) and PCN-223(Fe) show N_2 uptake around 430 cm^3/g at 1 bar. The experimental Brunauer-Emmett-Teller (BET) surface area of PCN-223(Free base) and PCN-223(Fe) is around 1600m^2/g and porosity is 0.6cm^3/g, values of which are in good agreement with the calculated

results using the non-disordered structure. When the Zr_{18} cluster model is used, the simulated results of both would be lower than experimental data, which further confirms our structural rationalization. The single crystal structure of PCN-223 is finally validated with powder X-ray diffraction results. Since the **shp-a** network has one of the highest connectivity among all the reported MOFs, we expected high chemical stability for PCN-223 and tested that under aqueous solutions with different pH values. After soaking in different solutions for 24h hours, the PXRD patterns of PCN-223(No metal) are completely maintained from 1M HCl solution to pH = 10 aqueous solution. Meanwhile, the N_2 uptakes of PCN-223(Free base) samples after different treatments are almost the same as that of the pristine sample, which is evidence for the stability of the framework under harsh chemical conditions (Figure 20b). Although the stability of PCN-223 under acidic conditions is not as good as PCN-222, PCN-223 exhibits much better stability in basic environments, allowing its application under different conditions. Moreover, PCN-223 shows excellent thermal stability.

Due to the high concentration of porphyrinic centers in the framework as well as excellent chemical stability for PCN-223, we therefore studied its catalytic activity for the hetero-Diels−Alder reaction between unreactive aldehydes and a diene, confirming PCN-223 as a recyclable heterogeneous catalyst.

The hetero-Diels−Alder reaction is one of the most powerful synthetic approaches for the construction of six-membered heterocyclic compounds. In particular, the cyclo-addition of aldehydes to dienes has been widely applied in the preparation of natural products.[106] However, most of these reactions involve the use of activated aldehydes

such as glyoxylates or electron-rich dienes such as Danishefsky's diene to reach a high yield. Only a small number of hetero-Diels−Alder reactions have been reported using unactivated aldehydes and simple dienes.[107] Moreover, the use of very strong Brønsted acids or Lewis acids is always necessary to activate the poorly reactive hetero-dienophile to compensate for the low reactivity of simple dienes, which severely restricts the choice of functional groups that can be tolerated under such harsh reaction conditions. Recently, Fujiwara *et al* reported the catalysis of the hetero-Diels−Alder reaction with unactivated aldehydes and simple dienes by using a iron(III) porphyrinic cation, which shows high catalytic performance as well as robustness in the reaction. [8c]

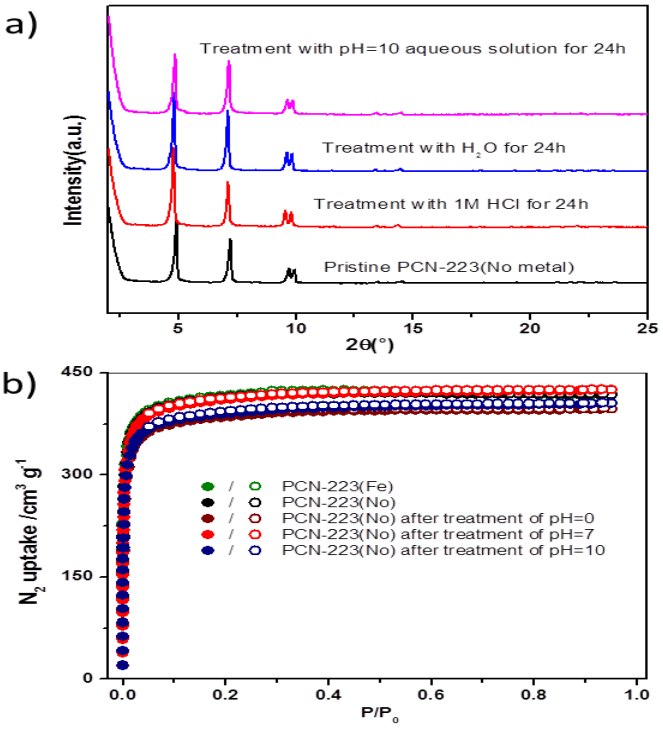

Figure 20. (a) Powder X-ray diffraction of PCN-223(No metal) under different conditions and (b) N_2 adsorption isotherms for PCN-223(Fe) and PCN-223(Free base) after harsh treatments to show the excellent stability.

Since the cationic iron (III) porphyrin has very strong affinity to all electron donating species, the synthesis and handling have to be conducted under an inert environment. However, when porphyrinic MOFs are used, the catalysts can be conveniently recycled, which could save a lot of effort for making new catalyst and for product separation. Following the synthetic procedure in the reported homogeneous system, we made the cationic Fe(III) porphyrin center in PCN-223(Fe) and tested its catalytic performance using the same substrates (Scheme 2). The potential block of cationic sites and pores of PCN-223(Fe) due to the generation of AgCl precipitates is highly concerned but could not be directly measured because of the high activity of cationic PCN-223(Fe). Remarkably, the reaction of benzaldehyde with 2,3-dimethyl-1,3-butadiene reached 99% yield confirmed by both column chromatography (NMR) and GC (Table 7), which is even higher than that reported in the optimal homogeneous system. It is also worth noting that we employed toluene as the solvent instead of the carcinogenic benzene, which is the optimized solvent in the reported homogenous system. Since the catalytic mechanism is to use the naked cationic iron (III) center to polarize the aldehyde species, electron withdrawing groups on the porphyrin should increase the polarization ability of the iron center and thus enhance the catalytic activity. To eliminate other possible reactive centers, two control experiments were performed with PCN-223(Free base) and PCN-223(Fe) with no $AgBF_4$ additives to confirm that only the cationic PCN-223(Fe) is active towards the catalysis of the hetero-Diels-Alder reaction. Therefore, the higher catalytic activity in cationic PCN-223(Fe) than the homogeneous system could be ascribed to two possible reasons: carboxylate itself is an

electron withdrawing group, which could decrease the electron density on the iron center; meanwhile, due to its high (Z/r) value, zirconium could be considered as an extremely effective electron withdrawing group, which would dramatically decease the electron density on the porphyrin after bonding to the carboxylates. Both effects could further increase the polarization ability of the iron center and increase the overall catalytic activity. Such an extraordinary result also highlights the advantages of using MOFs as a heterogeneous system. Because of the porous framework, MOFs can be used as heterogeneous catalysts in any solvent despite the solubility of the catalyst, compared to homogenous systems that always require extra synthetic effort to find the appropriate solvents, which greatly limits the scope of the catalytic reaction. For instance, although carboxylate groups might enhance the catalytic activity, TCPP has very low solubility in nonpolar solvents, so it cannot be used alone in benzene or toluene. Furthermore, the inorganic units could further increase the activity of the linker instead of acting as pure spectators; however, these inorganic clusters would be useless in a homogeneous system due to their limited solubility in common organic solvents. This illustrates that when MOFs are applied in a suitable system, the metal-containing nodes, organic linkers, and framework porosity can be most effectively integrated to enhance the utility of a catalytic system. Of course, it should be pointed out that optimizing reaction conditions, such as temperature, substrate solubility, and even substrate diffusion from the solvent towards the porous catalyst, are still necessary.

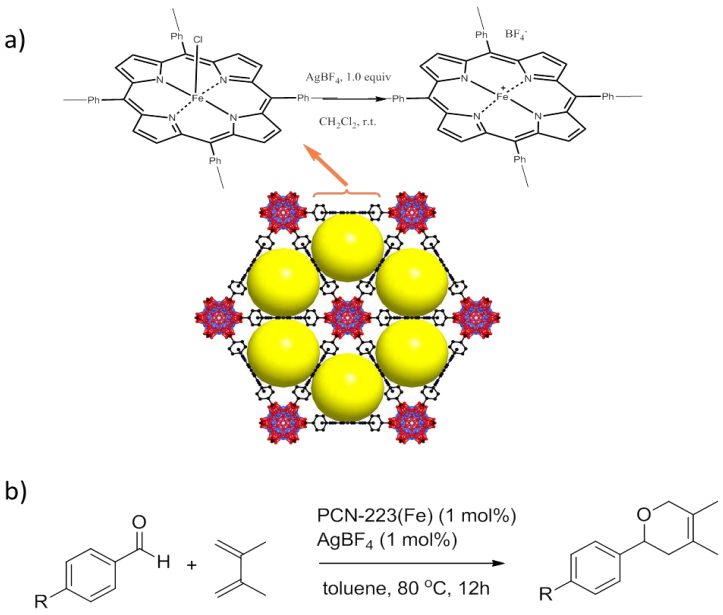

Scheme 2. (a) The preparation of cationic iron porphyrin center in PCN-223(Fe). (b) Hetero-Diels−Alder reaction catalyzed by PCN-223(Fe).

Table 7. Hetero-Diels−Alder reaction based on different benzaldehydes.

Entry	R	GC yield (%)	Isolated yield(%)
1	H	>99	>99
2	CH_3	98	96
3	CN	28	30
4	Ph	51	56

Three other functionalized benzaldehydes were also tested (Table 7); 4-methylbenzaldehyde is almost completely converted to product while 4-

phenylbenzaldehyde and 4-cyanobenzaldehyde show relatively low yields, which are presumably caused by the electron withdrawing effect of the functional groups. To evaluate the recyclability, the PCN-223(Fe) catalyst was recovered after each reaction (4-methylbenzaldehyde and 12 h) by simple centrifugation and the recovered catalyst was reused for the next reaction. The catalytic activity was well maintained; the yield of the reaction (12 h) is still higher than 90% after 5 cycles, which demonstrates the excellent recyclability of PCN-223(Fe) (Table 8).

Table 8. Recyclability test of PCN-223(Fe) using 4-methylbenzaldehyde (12 h reaction time).

Cycles	R	GC yield (%)
1	CH_3	98
2	CH_3	95
3	CH_3	96
4	CH_3	94
5	CH_3	90

2.4.4 Conclusion

In conclusion, we synthesized a new porphyrinic Zr-MOF (PCN-223), which is constructed from a new hexagonal prismatic twelve-connected Zr_6 cluster. After post synthetic treatment, the cationic PCN-223(Fe) is demonstrated to be an excellent recyclable heterogeneous catalyst for the hetero-Diels−Alder reaction.

2.5 An Exceptionally Stable, Porphyrinic Zr Metal-Organic Framework Exhibiting pH-dependent Fluorescence

2.5.1 Introduction

In recent two decades, metal-organic frameworks (MOFs) have received tremendous attention due to their powerful attributes on structural and chemical versatility and tailorability.[1] The rational design in their construction promises these porous materials tailored to specific functional applications, such as, gas storage/separation, catalysis, sensor, and drug delivery.[2-5] Despite this, stability has being recognized as a crucial issue on the way to practical applications of MOFs. Thermally, MOFs usually stabilize up to 250 ℃ and the best record demonstrates that the framework is able to maintain until even higher than 500 ℃, which are robust enough as porous functional materials.[108-111] However, most of MOFs are more or less sensitive to moisture, which could be one of key limitations to meet the requirements of various applications. In addition, seldom MOFs were reported to be chemically resistant in an acidic or basic medium. Based on the previous reports, MOFs constructed by imidazole or pyrazolate derivatives are inclined to survive under alkaline conditions,[109] while carboxylate-coordinated MOFs would withstand an acidic environment.[112]

To target the MOFs with both thermal and chemical stabilities, our group have aimed at zirconium(IV) carboxylates. According to “soft and hard acids and bases” theory, zirconium(IV) cation and carboxylate anion belong to hard acid and hard base, respectively, which makes the coordination bonds between zirconium and carboxylic

oxygens very strong and potentially tolerable to attack of water, acid and even base. However, the inert coordination bonds between Zr^{4+} cations and carboxylate anions make ligand exchange reactions extremely slow, which is unfavorable for defect repair in the process of crystal growth. Therefore, it is especially difficult to obtain single crystals of zirconium carboxylate MOFs and only a couple of them have been structurally characterized to date.[112] During our persistent efforts in this research line, we have reported PCN-56 to -59 with UiO type structure that remain intact in dilute acid and base (2< pH <11) and PCN-222 survive in concentrated HCl solution recently. In this work, the assembly of zirconium(IV) and tetracarboxylic acids based on porphyrin center that could play multifunctionalities (such as light-harvesting, oxygen transportation, and catalysis, etc.), leads to exceptionally stable Zr-MOFs, which not only thermally stable (≥ 350ºC) but also retain frameworks in the aqueous solutions with pH ranges from 1 to 11. To our knowledge, this is the broadest pH range that a porphyrinic MOF can survive thus far. Remarkably, by perfectly combining the wide-pH-range stability and the dye characteristic of involved porphyrin center, our preliminary results have demonstrated that the resultant MOF could present pH-dependent fluorescence.

2.5.2 Experimetal Section

Materials Methyl 4-formylbenzoate was purchased from Oakwood Products, Inc. Pyrrole, propionic acid, *N*,*N*-dimethylformamide (DMF), *N*,*N*-diethylformamide (DEF), benzoic acid, acetone, zirconium(IV) chloride, glacial acetic acid, and zinc(II) chloride

were purchased from Alfa Aesar. The tetrakis(4-carboxyphenyl)porphyrin (H_2TCPP) and [5,10,15,20-Tetrakis(4-carboxyphenyl)-porphyrinato]-Zn(II) (Zn-TCPP) ligands were synthesized according to previous reports.[8b] All commercial chemicals were used without further purification unless otherwise mentioned.

Instrumentation Powder X-ray diffraction (PXRD) was carried out with a BRUKER D8-Focus Bragg-Brentano X-ray Powder Diffractometer equipped with a Cu sealed tube (λ = 1.54178) at 40 kV and 40 mA. Elemental analysis (C, H, and N) were performed by Atlantic Microlab, Inc (Norcross, Georgia). Thermogravimetric analyses (TGA) were carried out on a Shimadzu TGA-50 thermal analyzer from room temperature to 650 ℃ at a ramp rate of 5 ℃/min in a flowing nitrogen atmosphere. Fourier transform infrared (IR) measurements were performed on a SHIMADZU IR Affinity-1 spectrometer. Nuclear magnetic resonance (NMR) data were collected on a Mercury 300 spectrometer. Scanning Electron Microscope (SEM) images and Energy Dispersive Spectrometer (EDS) analyses were taken by FEI Quanta 600 FE-SEM.The fluorescence spectra were recorded by a PTI QuantaMaster series spectrofluorometer. The pure MOF sample obtained without introduction of pre-synthesized PCN-225 in the starting material was employed for fluorescent pH sensing studies. Prior to the fluorescent experiments, 2 mg of PCN-225 was soaked in 2.55 mL aqueous solutions with different acidity-basicity and the mixtures were ultrasonicated for some time to reach good dispersion. The final pH values for all solutions were re-measured by a pH-meter after fluorescent experiment. Gas sorption measurements were conducted using a Micrometritics ASAP 2020 system at different temperatures.

Synthesis of PCN-225 $ZrCl_4$ (25 mg), H_2TCPP (10 mg), benzoic acid (550mg) and 5 drops of acetic acid in 2 mL of DEF were ultrasonically dissolved in a Pyrex vial. The mixture was heated in 120 ^{o}C oven for 12 h. After cooling down to room temperature, purple powder was harvested by filtration (10 mg, 70% yield). Anal. calcd. (%) for PCN-225: C, 48.18; H, 2.86; N, 4.68%. Found: C, 48.78; H, 2.99; N, 4.32%.

Synthesis of PCN-225(Zn) $ZrCl_4$ (60 mg), Zn-TCPP (50 mg), and benzoic acid (3g) in 9 mL of DEF were ultrasonically dissolved in a Pyrex vial. The mixture was heated in 120 ^{o}C oven for 12 h. After cooling down to room temperature, violet crystals were harvested by filtration (10 mg, 70% yield). Anal. calcd. (%) for PCN-225(Zn): C, 45.76; H, 2.56; N, 4.45%. Found: C, 46.44; H, 2.86; N, 4.05%.

Sample Activation Before gas sorption experiment, as-synthesized PCN-225 and PCN-225(Zn) samples were washed with DMF followed by acetone, and then immersed in acetone for around 2 days and exchanged once with fresh acetone during the period. The mixture was finally centrifuged and the acetone was removed by decanting. The sample was dried first by N_2 sweeping and then by using the "outgas" function of the adsorption instrument for 10 h at 100 ^{o}C prior to gas adsorption/desorption measurement.

Single Crystal X-ray Crystallography Single crystals of PCN-225 suitable for single-crystal X-ray diffraction have been obtained in our experiments. As their similar structures evidenced by powder X-ray diffraction patterns and smaller crystals of PCN-225(Zn), single crystal data of PCN-225 were collected only.

Single crystal X-ray data of PCN-225 were collected on a Bruker Smart Apex diffractometer equipped with a low temperature device and a fine-focus sealed-tube X-

ray source (Mo-Kα radiation, λ = 0.71073 Å, graphite monochromated). The data frames were collected using the program APEX2 and processed using the program SAINT routine within APEX2. The data were corrected for absorption and beam corrections based on the multi-scan technique as implemented in SADABS. The structure was solved by direct methods and refined by full-matrix least-squares on F^2 with anisotropic displacement using the SHELXTL software package. Non-hydrogen atoms were refined with anisotropic displacement parameters during the final cycles. Hydrogen atoms on carbon and nitrogen were calculated in ideal positions with isotropic displacement parameters set to 1.2 $\times$ Ueq of the attached atoms, while hydroxide hydrogen atoms were not added into the structure. In the structure, free solvent molecules were highly disordered, and attempts to locate and refine the solvent peaks were unsuccessful. Contributions to scattering due to these solvent molecules were removed using the SQUEEZE routine of PLATON; the structures were then refined again using the data generated. The contents of the solvent region are not represented in the unit cell contents in the crystal data. Crystallographic data and structural refinements for PCN-225 are summarized in Table 9.

Table 9. Crystal data and structure refinements for PCN-225.

Formula	$C_{48}H_{34}N_4O_{16}Zr_3$
Fw	1196.5
Color	Purple
Crystal system	Tetragonal
Space group	$I4_1/amd$
a, b (Å)	16.581(5)
c (Å)	78.30(2)
α, β, γ (°)	90
V (Å^3)	21527(11)
Z	8
$d_{calcd.}$ (g/cm^3)	0.733
μ(mm^{-1})	0.319
T (*K*)	163(2)
F(000)	4720
Reflns collected	102518
Independent reflns	5921
Obsd data [I>2σ(I)]	3333
Data/restraints/parameters	5921 / 18 / 169
Completeness	99.7%
GOF on F^2	0.954
*R*1, *wR*2 [I > 2σ(I)]	0.0560, 0.1451
*R*1, *wR*2 (all data)	0.1219, 0.1721

2.5.3 Results and Discussion

Solvothermal reactions of zirconium(IV) chloride, tetrakis(4-carboxyphenyl)porphyrin (H_2TCPP), acetic acid and benzoic acid in N,N-diethylformamide (DEF) at 120 ℃ yielded single crystals of $Zr_6(\mu_3\text{-}O)_4(\mu_3\text{-}OH)_4(OH)_4(H_2O)_4(H_2TCPP)_2$ (denoted as PCN-225, PCN stands for "porous coordination network"). The similar reaction afforded polycrystalline powder of $Zr_6(\mu_3\text{-}O)_4(\mu_3\text{-}OH)_4(OH)_4(H_2O)_4(ZnTCPP)_2$ (denoted as PCN225(Zn)) in the presence of $ZnCl_2$ while without acetic acid in the reactants. Powder X-ray diffraction (XRD) studies have revealed that both MOFs have similar framework topology and the only difference should be the replacement of two hydrogen atoms in each porphyrin center in PCN-225 with one Zn atom in PCN-225(Zn). Therefore, the structure of PCN-225 will be discussed below as a representative.

PCN-225 crystallizes in the tetragonal $I4_1/amd$ space group. There are two unique Zr atoms and both are coordinated by eight oxygen atoms, in which Zr1 coordinates four μ_3-oxygens and the other four carboxylate oxygens from four H_2TCPP ligands; Zr2 connects three hydroxide oxygens, three μ_3-oxygens, and two carboxylate oxygens from two H_2TCPP ligands. In the Zr_6 core of PCN-225, one Zr-O bond is around 2.05Å that is shorter than 2.13Å in UiO-66 and another Zr-O bond is 2.23Å, which is longer than 2.13 Å. Since the Zr-O bond is an average length due to the symmetry in UiO-66 and the Zr_6 has lower symmetry in PCN-225, those two types of μ_3 oxygen could be differentiated into O^{2-} and OH^-. Therefore, the terminal oxygens have to be 4-OH and 4 H_2O. The average length of the bonds between Zr and terminal oxygens is 2.18Å which is shorter

than Zr-H_2O bond (2.21Å) in PCN-222, which suggests shorter bonds (Zr-OH) existing in PCN-225. This is consistent with our assignment. Therefore, the cluster formula in PCN-225 is assigned to be $Zr_6(\mu_3\text{-}O)_4(\mu_3\text{-}OH)_4(OH)_4(H_2O)_4(COO)_8$.

Six Zr atoms connect eight μ_3-oxygen atoms to form a $Zr_6(\mu_3\text{-}O)_4(\mu_3\text{-}OH)_4$ cluster core, around which four –OH and four H_2O groups are attached as terminal groups with the eight bridging hydroxide oxygens in the same plane. As displayed in Figure 18a, each edge of Zr_6 octahedron is bridged by one carboxylate from a H_2TCPP ligand to afford an 8-connected Zr_6 core. It is worthy to note that the only 8-connected Zr_6 cluster was reported in PCN-222 most recently, while the other ZrO_x motifs are 12-connected Zr_6 clusters and zirconium oxide chains in all Zr-carboxylate MOFs. Interestingly, for the cluster core in PCN-225, the six Zr atoms combine an exact octahedron (Figure 21b), while the eight μ_3-oxygens capped on the triangular faces of the Zr_6 octahedron form a highly distorted polyhedron, in which each three oxygens are in a unique plane (Figure 21c). In comparison, both Zr_6 octahedron and $(\mu_3\text{-}O)_8$ cube are idealized in PCN-222 (Figures 21). As a result, the cluster symmetry in D_{4h} in PCN-222 reduces to D_{2d} in PCN-225, which could further induce lower symmetry in the framework of PCN-225.

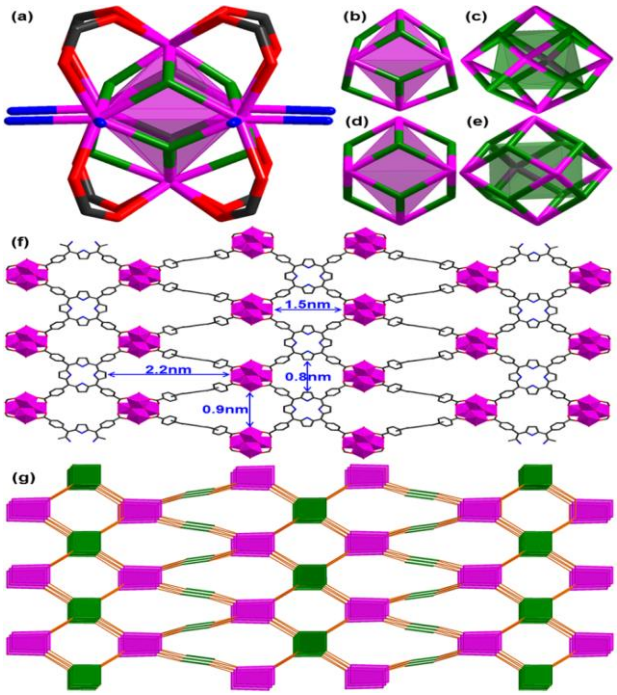

Figure 21. (a) $Zr_6(\mu_3\text{-}O)_4(\mu_3\text{-}OH)_4(OH)_4(H_2O)_4(COO)_8$ cluster. The oxygen atoms from μ_3-OH/-O, -OH/H_2O and -COO groups are shown in green, blue and red, respectively. (b, c) The irregular $Zr_6(\mu_3\text{-}O)_4(\mu_3\text{-}OH)_4$ cluster core in PCN-225, in which six Zr atoms combine an idealized octahedron shaded in pink (b) whereas eight μ_3 oxygen atoms form a highly distorted polyhedron highlighted in green (c). (d, e) The idealized $Zr_6(\mu_3\text{-}OH)_8$ cluster core in PCN-222, where the Zr_6 octahedron and $(\mu_3\text{-}O)_8$ cube are drawn in pink and green, respectively. (f) View of the structure of PCN-225 along the *b*-axis with two types of channels. The Zr, O, C, N atoms are shown in pink, red, gray and blue, respectively. H atoms are omitted for clarity. (g) Schematic representation of the unprecedented (4,8)-connected **sqc** net for PCN-225 framework, in which Zr_6 cluster and H_2TCPP ligand are simplified as purple cubic and green square nodes, respectively.

In the H_2TCPP ligand, the peripheral benzene rings have 60.84 ° dihedral angle deviated from the porphyrin central plane and each carboxylic acid links to one Zr_6 cluster. Therefore, the H_2TCPP ligand is in a 4-connected mode to interconnect with Zr_6 clusters, giving rise to a three-dimensional (3D) structure with exactly the same two types of channels along either *a* or *b*-axes, while all pores are blocked along the *c*-axis.

The small channel with size of 0.8 × 1.5 nm^2 in quadrangle shape is surrounded by two Zr_6 clusters and two ligands, whereas the larger one with size of 0.9 × 2.2 nm^2 in pear-like shape is comprised of three Zr_6 clusters and three ligands (Figure 21f). The solvent-accessible volume in PCN-225 is as high as 68.1% calculated using the PLATON routine.[12] As described above, the cluster and ligand can be respectively regarded as 8- and 4-connected nodes, thus in a topological view, the whole network can be extended to a 3D (4,8)-connected **sqc** net with the point symbol of $(4^4 \cdot 6^2)_2(4^8 \cdot 6^{16} \cdot 8^4)$ (Figure 21g). There has been a few (4,8)-connected MOFs reported and they are almost concerned with **flu**, **scu** and **alb** nets.[13] As far as we know, PCN-225 and PCN-225(Zn) represent the first MOFs with a (4,8)-connected **sqc** net.

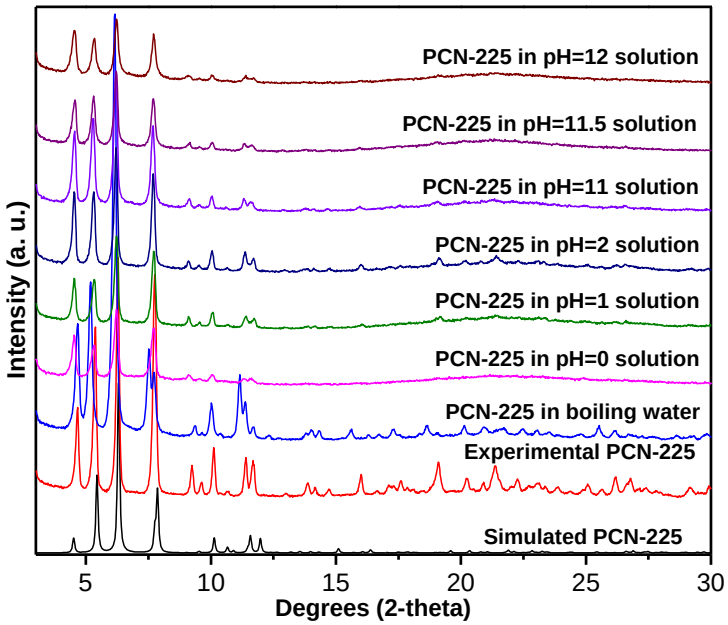

Figure 22. Powder X-ray diffraction (XRD) profiles for simulated and experimental PCN-225 and PCN-225 samples soaked in boiling water and aqueous solutions with pH values of 0, 1, 2, 11, 11.5 and 12 for 12 h.

Thermogravimetric (TG) analyses in N_2 stream show that the frameworks of both MOFs start to decompose around 350 ℃ and the weight loss before 300 ℃ could be mainly attributed to the isolated N,N-diethylformamide (DEF) molecules and coordinated hydroxide groups/water molecules. Strikingly, both MOFs also exhibit amazing chemical stability and powder XRD results have suggested that they remain stable not only in boiling water but also in aqueous solutions with pH values in the range of 0-12 (Figure 22). The powder XRD profiles are almost unaltered, revealing the retained crystallinity. To further demonstrate the stability of PCN-225, we have conducted N_2 sorption upon soaking MOF in the solutions with different pH values. N_2 adsorption isotherms indicate that the porosity of PCN-225 is perfectly maintained in pH = 1 to 11 solutions as well as boiling water. Only slight decrement has been found in pH=0 solution and less than half of the porosity loss has been observed in pH=12 solution, which indicates the relative stability in a wider pH range. Although some MOFs have been reported to have water tolerance or chemical stability in acidic or basic media, very few MOFs were found to be resistant to both acid and base. To our knowledge, NO_2-tagged UiO-66 was reported to have short-period (2 h) stability in both acid and basic solutions, and a microporous pyrazolebased Ni-MOF with pore size of 1 nm was demonstrated to be stable in solutions with a pH range of 2-14. The enlarged pore sizes usually weaken the framework stability and make their collapse easier under harsh conditions. Therefore, PCN-225 is one of the most stable MOFs with large pore sizes which can survive in an extensive pH range.

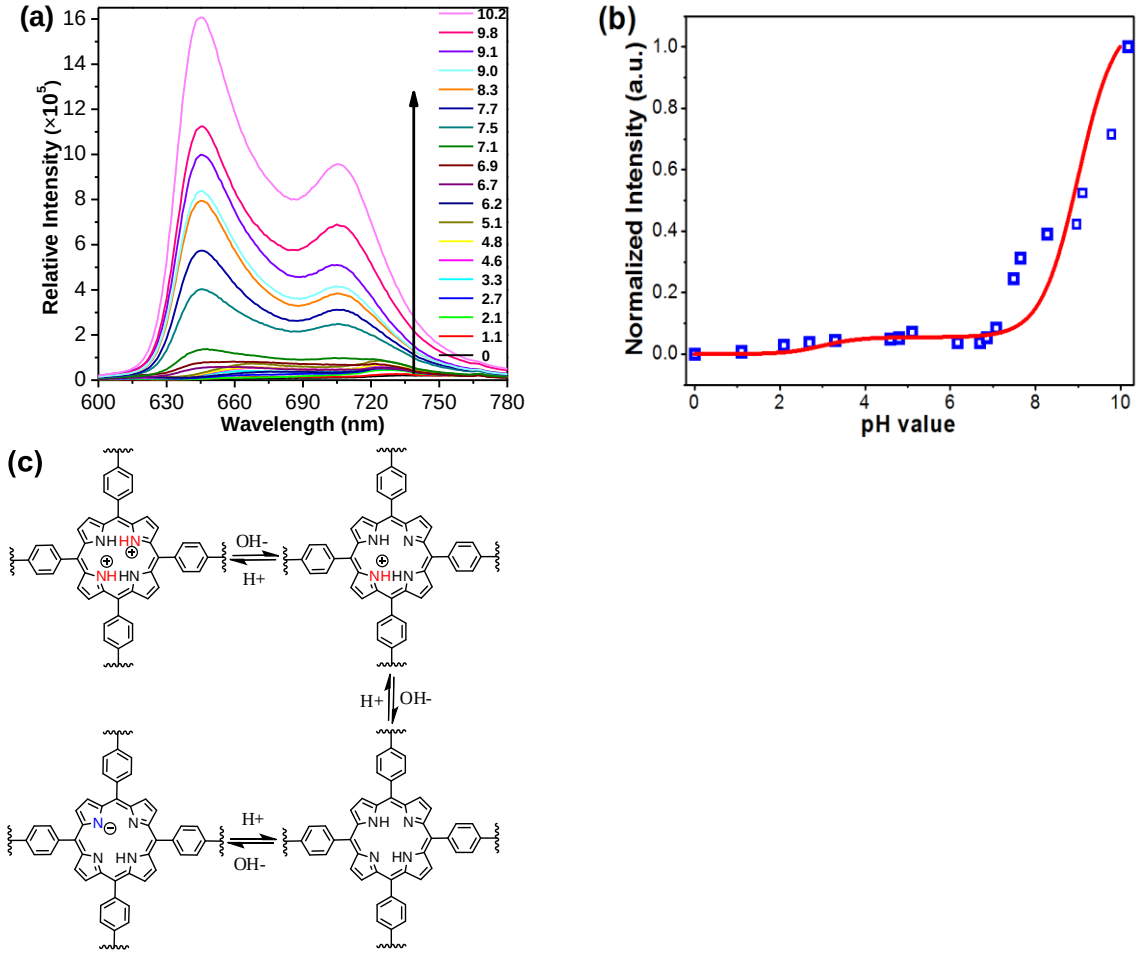

Figure 23. (a) The pH dependent fluorescence of PCN-225 in the aqueous solutions with pH ranging from 0 to 10.2 measured under excitation of 415 nm. (b) The blue points showed fluorescence emission at 725 nm at different pH, matching the simulation fluorescence intensity (red line). (c) The protonation and deprotonation processes of porphyrin involved in PCN-225 framework in experimental acidic and basic media (pH = 0-10.2).

The permanent porosity of both MOFs has been confirmed by nitrogen and argon sorption experiments at 77 and 87 K, respectively. The N_2 uptakes fall in 450-500 cm^3/g (STP) and the similar Brunauer-Emmett-Teller (BET) surface areas are 1902 and 2080 m^2/g, respectively for PCN-225 and PCN-225(Zn). These values are among the highest reported for porphyrinic MOFs and the porosity is hardly preserved upon removal of

solvent molecules in previously reported porphyrinic MOFs.[47-55] The slightly higher Ar uptakes than N_2 should be attributed to the smaller molecule diameter of argon that allows it to occupy pore spaces more efficiently. The similar H_2 uptakes for PCN-225 and PCN-225(Zn) are 1.80 and 1.76 wt%, which are comparable to most of MOFs and at the high end among those for Zr-MOFs with the high weight of Zr element. The slightly lower isosteric heat of H_2 adsorption for PCN-225 than that of PCN-225(Zn) should be ascribed to the absence of exposed zinc (II) centers.

Fluorescent pH sensors have certain advantages over electrodes and present widespread applications spanning from environmental analysis, bioanalytical chemistry to medical diagnostics, etc. Encouraged by the wide-pH-range stability, in the combination of fluorescent porphyrin dye involved in the framework, the pH-dependent fluorescence of PCN-225 has been explored (Figure 23a). The weak fluorescence emission of H_2TCPP ligand at 725 nm (λ = 415 nm) is owing to the conjugated double bond system and the high mobility of the π-electrons. Similarly, the excitation of PCN-225 at 415 nm gives emission peak at ~725 nm, which could be assigned to the intraligand transitions. Interestingly, the fluorescence intensity of PCN-225 is strongly correlated with pH value of the dispersed solution in our experimental pH range (0-10.2), in which the most acidic solution gave weakest fluorescence while the highest intensity was obtained with pH = 10.2 solution. Significantly, although the intensity almost rises along with pH increasing in the whole experimental range (0-10.2), it is not a simple linear relationship between pH value and fluorescent intensity (Figure 23b), which is in good agreement with our simulated results (Section 11 in the SI). When the pH is below

5, which is characteristic of protonation of the pyrrole ring, rising the pH leads to a very slightly increase in emission intensity. At high acidity, proton in the aqueous solution attach to the pyridine-type nitrogen atoms in the porphyrin center to afford the protonated nitrogens, which destroy the π-electron conjugated double-bond system of porphyrin and thus result in significant fluorescence quenching (Figure 23c).[113-114] In comparison, when the pH is higher than 7, PCN-225 presents much stronger fluorescence that is in close association with pH. The fluorescence enhancement and slight blue shift in basic solution are assumed to arise from deprotonation of imino group of porphyrin involved in the PCN-225 framework (Figure 23c).[113] So far, only one Eu-based MOF has been reported as a pH senor in the pH range of 5-7.5.[115-116] Our preliminary results indicate pH-dependent fluorescence response of PCN-225 in a much wider pH range due to the exceptional chemical stability, which suggests that PCN-225 could be promising MOF for pH sensing, especially in the pH range of 7-10.

2.5.4 Conclusion

In summary, zirconium-porphyrin frameworks, PCN-225 and PCN-225(Zn), have been developed, as the first MOFs with a (4,8)-connected **sqc** net. They exhibit exceptional chemical stability in aqueous solutions with pH ranging from 1 to 11, which, to our knowledge, is the most extensive pH range that a porphyrinic MOF can survive. Remarkably, given the wide-pH-range stability and that the central core region of porphyrin free base is subject to protonation-deprotonation equilibrium upon varying the pH, the fluorescence intensity of PCN-225 is in close correlation with pH variation, of

which 7< pH <10 is most sensitive range for intensity response. The results indicate PCN-225 is promising for pH sensing. Furthermore, the readily installation of exposed metal sites in the porphyrin center in PCN-225, combined with its high stability, should raise their potential for a variety of applications, especially, catalysis, light-harvesting, sensor, and so on.

3. STABLE METAL-ORGANIC FRAMEWORKS CONTAINING SINGLE-MOLECULE TRAPS FOR ENZYME ENCAPSULATION [*]

3.1 Introduction

Metal-organic frameworks (MOFs) with large pores or channels are considered as promising candidates for immobilization of many catalysts, such as metal complexes, nanoparticles, and enzymes.[117~120] Enzymes in particular can be made more valuable by immobilization, due to their high cost and difficulty in their reuse and recovery.[121] A range of solid supports have been explored for enzymes, such as sol gels, hydrogels, organic micro-particles, and porous or nonporous inorganic supports.[122] However, there have been disadvantages associated with these supports, including very low protein loading in the nonporous systems and denaturation of enzymes in sol gels due to their brittle and disordered structures. [123-127] Mesoporous silica nanoparticles, which possess large pore size, high porosity, and a very ordered structure, have been demonstrated as promising enzyme supports. However, due to their one dimensional (1-D) channel structure, insufficient interactions between the inner channel surface of mesoporous silica and enzymes result in significant leaching during multiple cycles of use. Moreover, aggregation still occurs inside the channel.[123-126]

---

[*] Reproduced with permission from: Feng, D.; Liu, T.-F.; Su, J.; Bosch, M.; Wei, Z.; Wan, W.; Chen, Y.-P.; Wang, X.; Wang, K.; Lian, X.; Gu, Z.-Y.; Park, J.; Yuan, D.; Zou, X.; Zhou, H.-C. "Stable Metal-Organic Frameworks Containing Single-Molecule Traps for Enzyme Encapsulation" Nature Comm, 2015, 6:5979. Copyright 2015 Nature Publishing Group.

Recently, we studied MOFs containing pre-designed single-molecule traps (SMTs) for carbon capture, wherein each SMT can trap one CO_2 molecule.[128] If the same concept is applied in enzyme immobilization, we can potentially diminish leaching, and encapsulate each enzyme molecule in a SMT to eliminate aggregation, optimizing the catalytic environment. MOFs, which have ultra-high porosity, tunable pore shape and size, and adjustable surface functionality, are an ideal platform for this novel single-enzyme encapsulation (SEE) or multiple-enzyme encapsulation (MEE) approach.

Based on structural rationalization, we herein report facile syntheses of a series of highly stable SMT-containing metal-organic frameworks (MOFs) based on trivalent metal species, namely PCN-332(M) (M = Al(III), Fe(III), Sc(III), V(III), In(III)) and PCN-333(M) (M = Al(III), Fe(III), Sc(III)). PCN-333 exhibits the largest cage (5.5 nm) and one of the highest void volumes (3.84 cm^3g^{-1}) among all reported MOFs. Remarkably, PCN-333(Al, Fe) shows high stability in aqueous solutions with pH values ranging from 3~9, making it an extraordinary candidate for enzyme encapsulation. Three enzymes with different sizes, horseradish peroxidase (HRP), cytochrome-c (Cyt C), and microperoxidase-11(MP-11), were selected. From a pure size-match point of view, HRP and Cyt C will most likely undergo SEE, whereas MP-11 will go through MEE due to size mismatch. Nevertheless, all three enzymes have been successfully encapsulated into PCN-333(Al) with extremely high loading amounts among all reported solid supports. These immobilized enzymes either maintain or surpass their catalytic activities over the free enzymes, and exhibit smaller K_m and better catalytic performance in organic

solvents. Remarkably, these immobilized enzymes show almost no leaching during catalysis and recycling, and maintain high catalytic activity.

3.2 Experimental Section

Materials and Instrumentation Horseradish peroxidase (HRP), N, N-dimethylformamide (DMF), N, N-diethylformamide (DEF), Acetone, 1,3,5-Trichlorobenzene, $AlCl_3$, $FeCl_3$, VCl_3, $ScCl_3.6H_2O$, $In(NO_3)_3.xH_2O$, $CHCl_3$ were purchased from Alfa Aesar. Cytochrome C from bovine heart (Cyt c) and Microperoxidase sodium salt (MP-11) were purchased from Sigma Aldrich. All commercial chemicals were used without further purification unless otherwise mentioned. Synchrotron powder X-ray diffraction (PXRD) was carried out with Bruker D8-Discover diffractometer equipped with a Mo sealed tube (λ = 0.72959) on the beamline 17-BM at the Advanced Photon Source, Argonne National Laboratory. Other PXRD experiments were carried out on a BRUKER D8-Focus Bragg-Brentano X-ray powder Diffractometer equipped with a Cu sealed tube (λ = 1.54178) at 40 kV and 40 mA. HRTEM was performed on a JEOL JEM-2100F microscope at 200 kV equipped with a field emission gun. Thermogravimetric analyses (TGA) were carried out on a Shimadzu TGA-50 thermal analyzer from room temperature to 600 ℃ at a ramp rate of 2 ℃/min in a flowing nitrogen atmosphere. Nuclear magnetic resonance (NMR) data were collected on a Mercury 300 spectrometer. Gas sorption measurements were conducted at different temperatures using a Micrometritics ASAP 2020 system.

3.3 Results and Discussion

The largest pore reported in MOFs was based on a 1-D hexagonal channel structure, which requires a complicated synthetic process to make an extremely long organic linker in order to reach enzymatic size. Considering the structural feature of the 1-D channel, it can only partially interact with immobilized enzymes even if the size is very compatible. As is in mesoporous silica, once enzymes are incorporated, aggregation still exists. Moreover, after those channels are occupied, there is no other pathway allowing the fast diffusion of both reactants and products. In comparison, cages will act as SMTs affording strong interactions between the cages and the encapsulated enzymes. Additionally, cages usually have small windows, which can efficiently encapsulate enzymes, diminishing aggregation, eliminating leaching, and optimizing the catalytic environment. Unfortunately, there are very few reported MOFs with enzyme compatible cages, and even fewer can survive in aqueous media[129-130]. Thus, MOFs with larger cages and better stability are highly desired for enzyme encapsulation.

The extension of organic linkers, which mostly serve as the faces or edges of pores in MOFs, is the main approach to achieve large pores in MOFs.[131-137] However, the pore shape or symmetry plays a very important role in determining the overall pore size. Approximating the cross-section of a pore (cage or channel) as a regular polygon with *n* edges (Figure. 24a), the diameter *d* of the inscribed circle corresponding to the pore can be expressed as the following,

$$d = \frac{1}{\tan(\frac{\pi}{n})} \times a \qquad (1)$$

where *a* is the edge of the regular polygon.

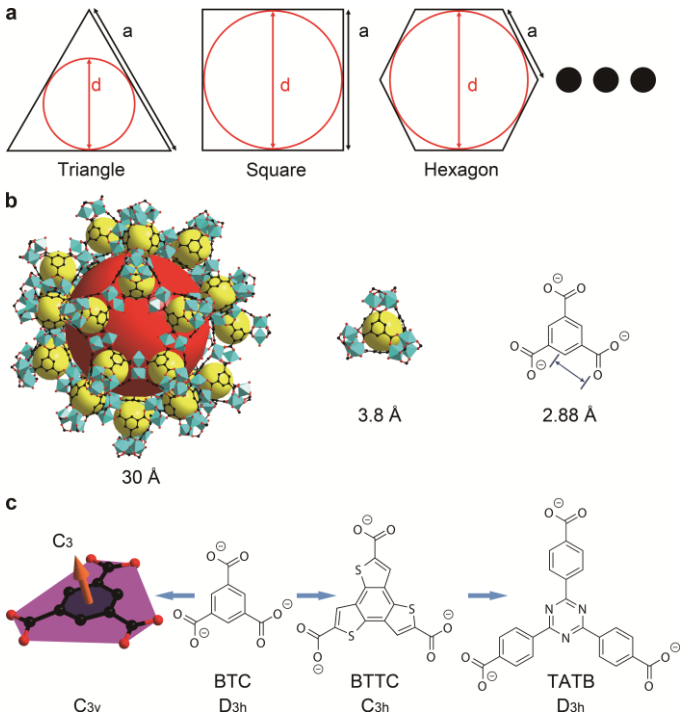

Figure 24. Pore expansion with preserved structure (the isoreticular approach): a. The relationship between the edge (*a*) and diameter (*d*) in regular polygons. b. The largest cage, super tetrahedral unit and organic linker in MIL-100. c. Idealized symmetries of BTC in MIL-100 and free BTC , BTTC and TATB.

If *a* is considered as the edge of a pore cross-section, then 1/tan(π/n) would be the magnification factor, which increases with *n* and determines how a certain change of *a* affects the overall pore diameter *d*. Therefore, by applying the isoreticular approach through ligand extension in MOFs, the pores with larger *n* values can be more efficiently enlarged than the pores with a smaller *n* value.

Hence, to construct MOFs with ultra-large cages and excellent chemical stability, we applied the isoreticular approach to the chemically highly stable mesoporous MOF, MIL-100.[138] The circular cross-section of the largest cage in MIL-100 is surrounded by twelve supertetrahedra, therefore *n* is very large (*n* = 12). In addition, MIL-100 is based on hard lewis acidic trivalent metal species (Al^{3+}, Fe^{3+}, Cr^{3+}, V^{3+}, Sc^{3+}), which interact strongly with carboxylates and give rise to the high stability of the framework in aqueous environments.[139-143]

Benzenetricarboxylate (BTC) (Figure. 24b), the organic linker in MIL-100, has idealized D_{3h} symmetry as a free anion. In the framework the ligand symmetry is reduced to C_{3v} by a bowl-shaped bending which increases the inherent energy of the ligand (the distance between the two planes is 0.288 Å). If the symmetry of the free linker were not D_{3h}, to form a similar structure, the energy of the linker would have been even higher in the framework, making the overall structure extremely energetically unfavored. To guarantee the formation of isoreticular structures of MIL-100, we selected two ligands which are most stable in a trigonal planar conformation, BTTC (benzo-tris-thiophene carboxylate) with a C_{3h} (pseudo-D_{3h} in crystallography) symmetry through the fused five member ring, and TATB (4,4',4''-s-triazine-2,4,6-triyl-tribenzoate), with idealized D_{3h} symmetry arised from ligand planarity, which is enforced by conjugation (Figgure 24c).

Solvothermal reactions of H_3BTTC or H_3TATB with MCl_3 (M= Al, Fe, V, Sc, In) afforded octahedral crystals of PCN-332(M) (M= Al, Fe, Sc, V, In) or PCN-333(M) (M= Al, Fe, Sc), respectively (Figure 25a, Fig 1-16). High resolution synchrotron powder X-

ray diffraction (PXRD) collected at 17-BM, Argonne National Laboratory shows that PCN-333 is cubic with $a \approx 127$ Å. This was further confirmed by 3D rotation electron diffraction (RED). The space group of PCN-333(Al) was determined to be *Fd*-3*m* by combining RED and high-resolution transmission electron microscopy (HRTEM) (Fig. 25c,). Structural models of PCN-333 and PCN-332 were built based on the isoreticular structure of MIL-100. The structural models of PCN-333(Al) and PCN-332(Fe) were further refined against the synchrotron PXRD data by Rietveld refinement with soft restraints for the M–O bond distances and rigid body for the ligands (Fig. 25b,). A 2D map is calculated by an inverse Fourier transformation from the amplitudes and phases of five symmetry-independent reflections with $d > 14$ Å extracted from the HRTEM image (Fig. 25), in which channels along the [111] direction with a size around 3.7 nm can be clearly visualized. Due to the beam damage of the sample and the damping effect of the objective lens (contrast transfer function), amplitudes obtained from the HRTEM image are attenuated. Replacing the amplitudes from the HRTEM image by those from the PXRD pattern gives an improved 2D map (Fig. 25f), which matches better the projected potential map of PCN-333(Al) calculated from the structural model (Fig. 25g). This strongly indicates that the structural model is correct.

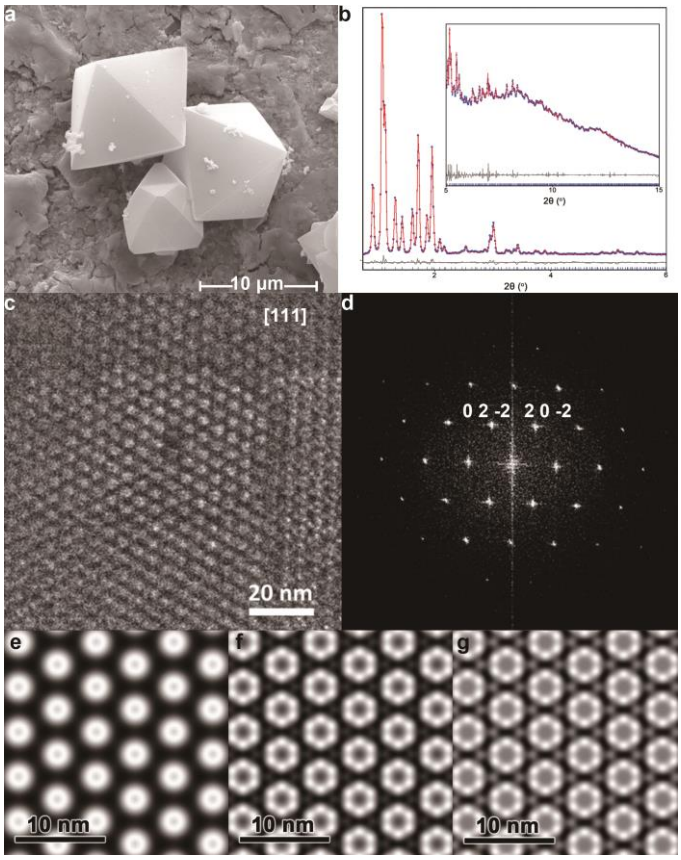

Figure 25. TEM and SEM anlyses of PCN-333(Al). a. SEM image of PCN-333(Al); b. Observed (blue), calculated (red) and difference (black) plot for the Rietveld refinement of PCN-333(Al); c. HRTEM image of PCN-333(Al) taken along the [111] direction, showing the pore with the size of about 3.7 nm in projection; d. Fourier transform of HRTEM image in c, from which the amplitudes and phases were extracted; e. Symmetry-averaged map after imposing the *p*6*mm* symmetry on the amplitudes and phases; f. Symmetry-averaged map (*p*6*mm*) calculated using the amplitudes from PXRD and phases from the HRTEM image; g. Projected electrostatic potential map calculated using the structure factor amplitudes and the phases from the structural model.

The structure of PCN-333 is built by sharing the vertices of the supertetrahedra, which consist of $M_3(\mu_3\text{-}O)(OH)(H_2O)_2$ units linked along the faces by the organic linkers (Fig. 26a). Consequently, two types of mesoporous cages, which can act as SMTs for encapsulation of an enzyme, are generated. A smaller dodecahedral cage is built of 20 supertetrahedra that are connected via vertex-sharing to construct a cavity with an

exclusive pentagonal window of 25.9 Å in diameter (Fig. 26b). A larger hexacaidecahedral (hexagonal truncated trapezohedral) cage is surrounded by 24 supertetrahedra that form a sphere with not only the pentagonal windows, but also hexagonal windows with a diameter of 30 Å (Fig. 26b). The inner diameter is 11 Å for the supertetrahedral cage, 34 Å for the dodecahedral cage, and 55 Å for the hexacaidecahedral cage. The largest cages in PCN-333 lie in a honeycomb arrangement in the [111] projection, which is consistent with the HRTEM result (Fig. 25). PCN-332 exhibits a similar structure as PCN-333, but with smaller cages due to the smaller linker (Fig. 26).

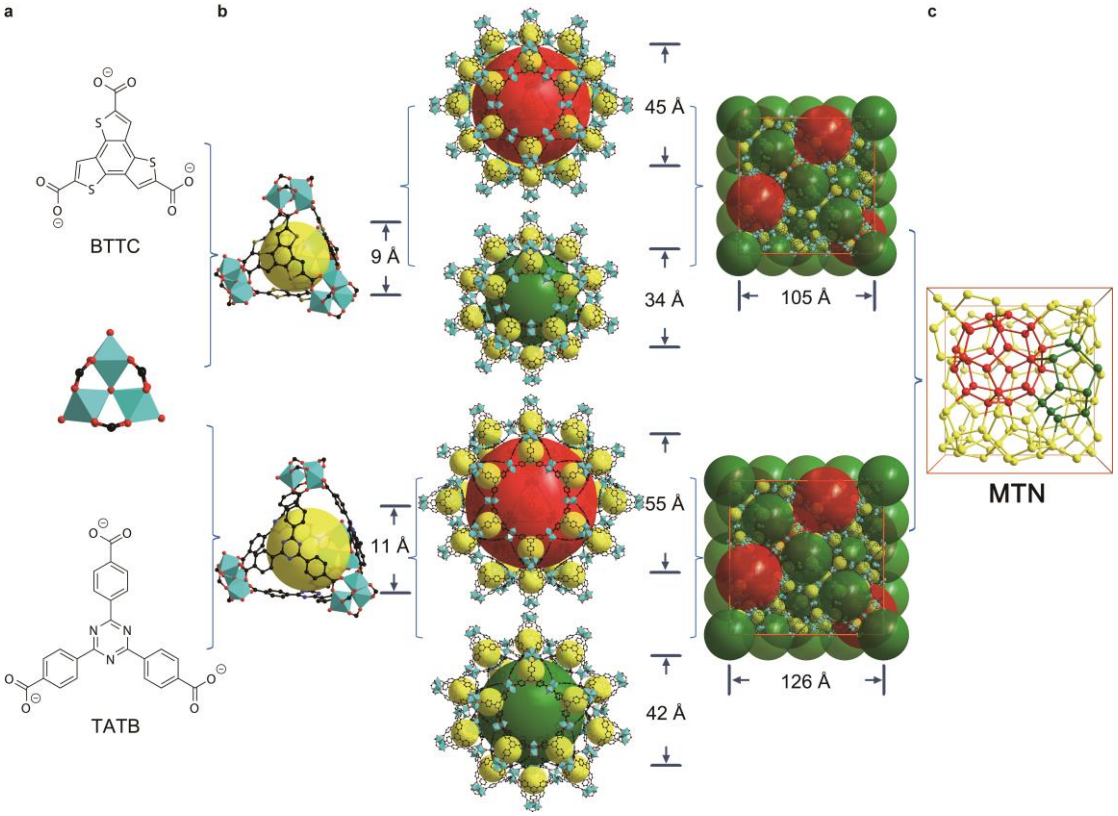

Figure 26. Structure illustrations of PCN-332 and PCN-333. a. Ligands used in PCN-332 and PCN-333. b. Three different cages in PCN-332 and PCN-333. c simplification of PCN-332 and PCN-333 into **MTN** topology.

Owing to the small ligand size and strong coordination bond between the organic linker and metal struts, both the PCN-332 and the PCN-333 series can be activated directly upon the removal of solvent, while many other MOFs with such high porosity must be carefully activated with supercritical CO_2. In order to assess the porosity of PCN-332 and PCN-333, we performed Ar sorption at 87 K and N_2 sorption at 77 K (Fig. 27a, 4b). PCN-333(Al) shows a total Ar sorption of 2950 cm^3g^{-1} and N_2 uptake of 2490 cm^3g^{-1}. The Brunauer-Emmett-Teller (BET) surface area is 4000 m^2g^{-1}. Two steep increases at $p/p_0 = 0.3$ and 0.5 on the Ar adsorption isotherm correspond to two types of mesoporous cages in PCN-333(Al). The experimental void volume of PCN-333(Al) is 3.81 cm^3g^{-1}, which is in good agreement with that calculated from the structural model (3.85 cm^3g^{-1}). Such high porosity is comparable to those of the most porous MOFs.[144-145] The porosity of PCN-333(Fe) is similar to that of PCN-333(Al), while the porosity of PCN-333(Sc) is slightly lower due to its poorer crystallinity. With an isoreticular structure but a smaller organic linker, the porosity and BET surface area of PCN-332 are significantly lower than those of PCN-333.

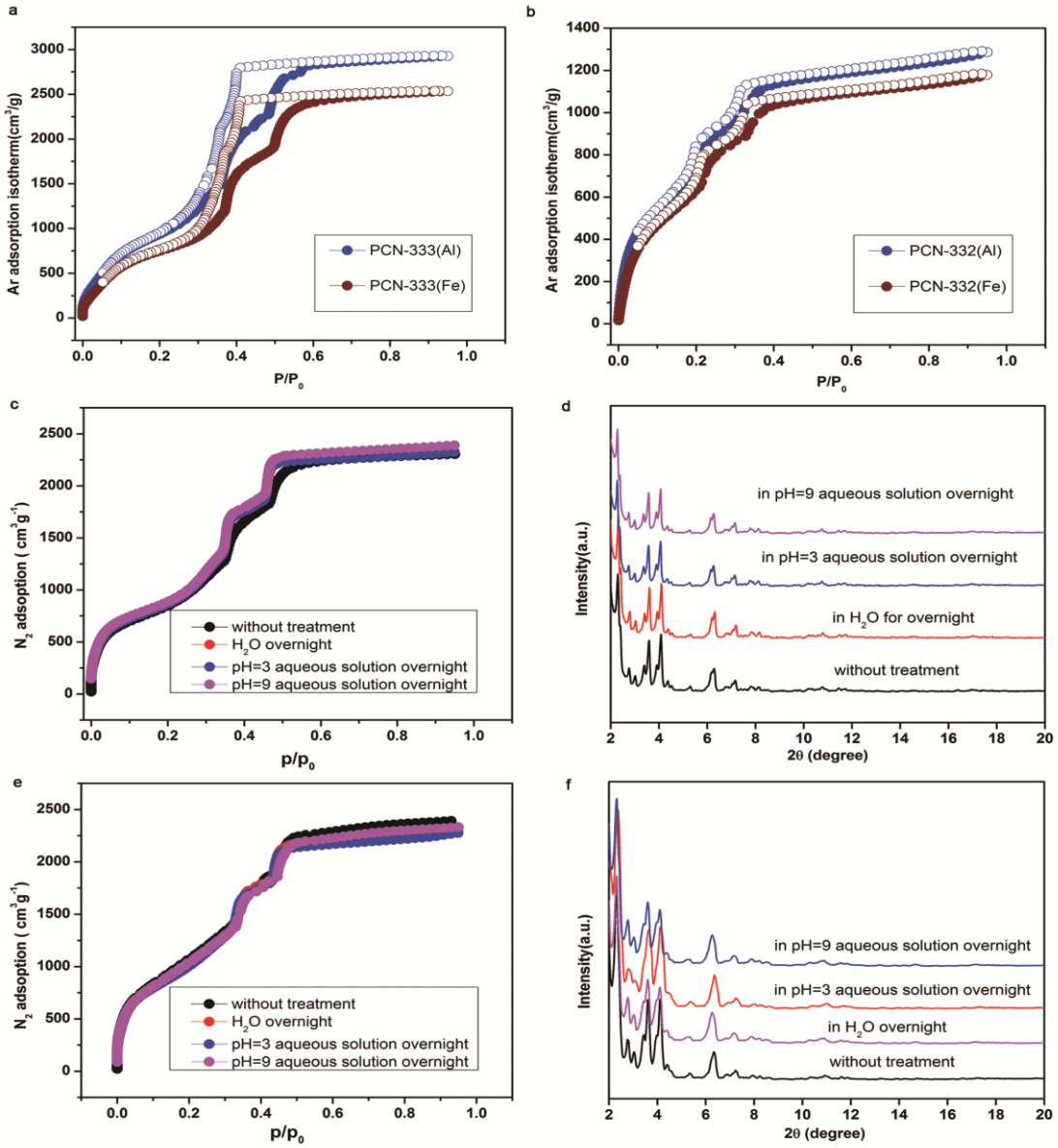

Figure 27. Porosity and stability characterization of PCN-333 and PCN-332. a. Ar sorption isotherms of PCN-333(Fe) and PCN-333(Al); b. Ar sorption isotherms of PCN-332(Fe) and PCN-332(Al); c, d. Stability tests of PCN-333(Al); e, f . Stability tests of PCN-333(Fe).

Despite its high porosity, PCN-333 still shows excellent stability in aqueous solutions. PXRD shows that PCN-333(Al) and PCN-333(Fe) remain intact without loss of crystallinity after immersion in pure H_2O and in aqueous solutions with pH of 3 and 9

(Fig. 27d and f). Furthermore, the N_2 sorption isotherms are almost completely maintained through those treatments (Fig. 27c and e), which further demonstrates the stability of these frameworks. The high positive charge density (Z/r) on small M^{3+} (Al^{3+}, Fe^{3+}) ions causes a strong electrostatic interaction between metal nodes and carboxylate linkers, which endows the frameworks with not only excellent stability towards attack by reactive species, but also high thermal stability

PCN-333(Al) as Support for Different Enzymes PCN-333 is an extraordinary example that meets most prerequisites as a promising enzyme support: the ultra-large cavities can act as SMTs for enzyme encapsulation; the ultrahigh porosity ensures high enzyme content after loading which guarantees the overall catalytic efficiency; and the SMTs can efficiently encapsulate enzymes, which can prevent both enzyme aggregation and leaching. In addition, it possesses excellent stability and is compatible with the working environment of an enzyme. A wide variety of enzymes, if smaller than the largest cage (5.5 nm) in PCN-333, can in principle be immobilized. If the enzyme is smaller than the cage, but the cage cannot accommodate two enzymes due to size limitation, a SEE can be achieved.

We have selected three commercially available enzymes that are smaller than the largest cage in PCN-333(Al), horseradish peroxidase (HRP), cytochrome-c (Cyt C), and microperoxidase-11 (MP-11), for the encapsulation experiment, and their catalytic performance and recyclability were also investigated.

To the best of our knowledge, all three enzymes have reached record-high loading among all enzyme immobilization cases. The maximum loading is 1.0 gg^{-1} (22.7 μ

molg^{-1}) for HRP, 0.95 gg^{-1} (77.0 μmolg^{-1}) for Cyt C, and 0.89 gg^{-1} (478 μmol/g) for MP-11 (Fig 28 and Table 10). Taking into account the size of each enzyme, HRP (size: 4.0 × 4.4 × 6.8 nm) can only be loaded into the large cage, while Cyt C (size: 2.6 × 3.2 × 3.3) is suitable for both the large cage and the medium cage and the small cage with an inner diameter of 1.1 nm will be empty, allowing diffusion of solvent molecules, reactants, and products. Assuming SEE, the maximum theoretical loading is 1.27 gg^{-1} for HRP (assuming only the large cage acts as a SMT) and 1.04 gg^{-1} for Cyt C (assuming both the large and medium cages act as SMTs), which are in good agreement with the experimental maximum loadings. For MP-11, considering its much smaller size (1.1 × 1.7 × 3.3 nm), multiple enzymes may enter each meso-cage, leading to a much higher molar concentration than the other two enzymes.

Due to the favorable interaction between the cage and the enzyme, to reach a saturated loading of each enzyme in PCN-333(Al) is rapid. HRP takes about 40 minutes; Cyt C takes 30 minutes while MP-11 takes about 10 minutes. However, for mesoporous silica, saturated enzyme loading usually takes at least several days to reach.[146-148] After loading of enzymes, the crystallinity, porosity and thermal stability of PCN-333(Al) samples were characterized, showing well maintained framework. Most importantly, the TEM-EDX elemental mapping of HRP@PCN-333(Al) sample indicates very well distributed HRP inside of the framework .

Enzyme leaching and loss of reactivity upon reuse are the major problems for all other enzyme supports.[5] After the immobilization of the three enzymes in PCN-333(Al), their catalytic activity was then evaluated with corresponding reactions.

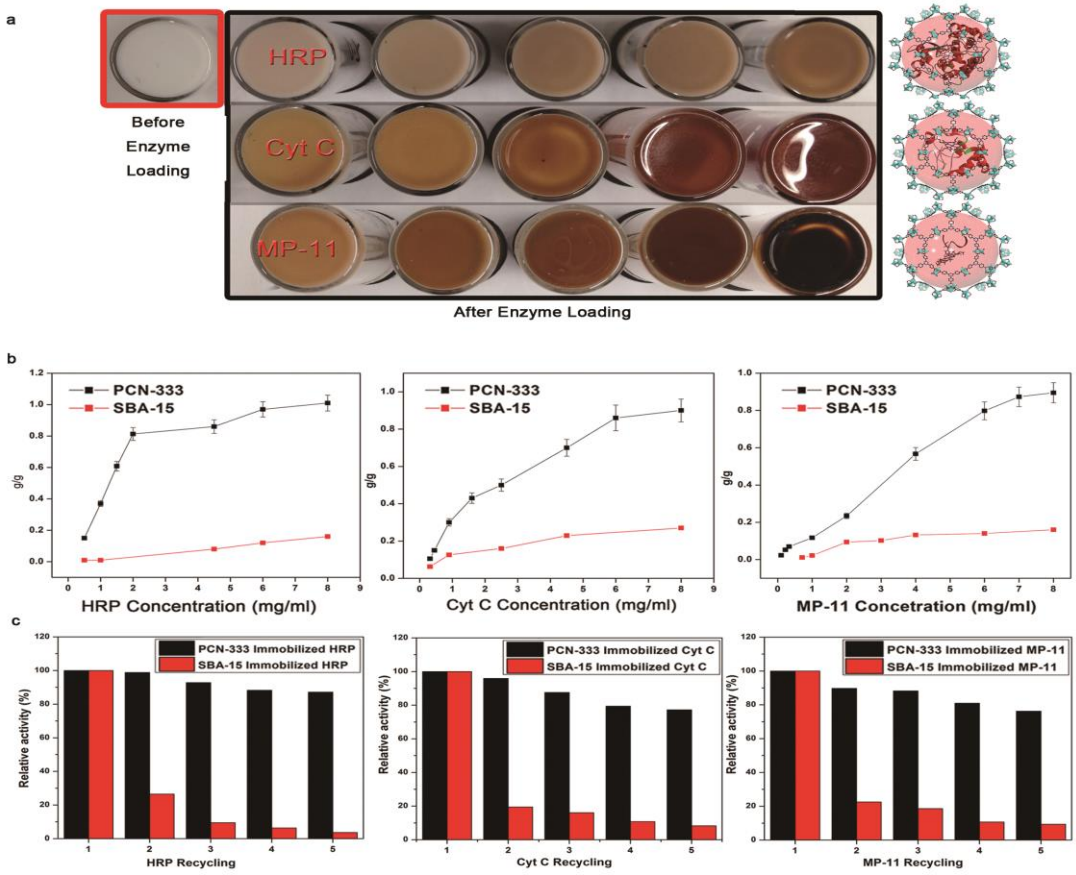

Figure 28. Enzyme loading and catalytic recycles of different enzymes. a. Color variations of PCN-333(Al) when loaded with different enzymes at different concentrations. b. Plots of the loading capacities of different enzymes in PCN-333(Al). c. Catalytic activity of immobilized enzymes in each recycle test.

Table 10. Comparison of different enzyme loadings in PCN-333(Al) and SBA-15.

Enzyme	Max-loading in PCN-333(Al) (gg^{-1})	Max-loading in PCN-333(Al) ($\mu molg^{-1}$)	Max-loading in SBA-15 ($\mu molg^{-1}$)
HRP	1.0	22.7	4.2
Cyt C	0.95	77.0	45
MP-11	0.89	478	20

Oxidation of o-Phenylenediamine (OPD) catalyzed by HRP and oxidation of 2-2'-azino-bis(3-ethylbenzthiazoline-6-sulfonic acid) (ABTS) catalyzed by Cyt C and MP-11 were performed respectively in acid-sodium citrate buffer with pH = 6 at room temperature. Compared with the free enzymes, enzymes immobilized in PCN-333(Al) show relatively smaller k_{cat} values, which may be caused by diffusion control. However, all three enzymes exhibit smaller K_m values, resulting in comparable k_{cat}/K_m values to the free enzymes (Table 11). The low K_m means that the enzyme requires a lower substrate concentration to achieve V_{max} and usually suggests that the enzyme may have a higher affinity with the substrate.

The free enzyme reacts more quickly than the encapsulated enzymes, though it requires significantly more concentration of substrate to reach its peak rate, under carefully controlled conditions designed to prevent it from being aggregated or denatured. However, in practical application, the reaction usually needs to be conducted in different media other than the buffer solution. Therefore, we measured the specific activity to investigate the catalytic activity of SEE and MEE in different media. Cyt C, which is of a suitable size to be incorporated into the two kinds of mesocages in a 1:1 ratio, has most likely undergone SEE, and shows fourteen times higher specific activity after immobilization in PCN-333(Al) than the free enzyme in water. In order to provide a more comprehensive comparison about the immobilized and free Cyt C, the kinetic parameters were investigated in this condition and the results indicate the immobilized Cyt C has a smaller K_m, and a higher K_{cat} and K_{cat}/K_m in water media (Table 12). Considering that Cyt C suffers severe self-aggregation or denaturation towards

temperature or pH variation,[149] such significant catalytic activity enhancement is evidence of SEE in PCN-333(Al). Immobilized HRP, which can also realize SEE, shows slightly higher specific activity in water. In comparison, MP-11, the size of which is much smaller than the mesocages, suitable for MEE, shows much decreased activity after immobilization. Moreover, in several different organic solvent mixtures, the immobilized HRP performs better than the free HRP. These results show the effectiveness of SEE under harsh reaction conditions.

After the completion of each catalytic reaction, the immobilized enzymes were then recycled by simple centrifuge. The catalytic reactivity remains almost unchanged for each PCN-333(Al) encapsulated enzyme after several cycles while very significant decrease of the activity is observed for the same enzymes immobilized in SBA-15, a well-known type of mesoporous silica (Fig 28c). The main reason for the excellent recyclability of PCN-333(Al) immobilized enzymes is the SEE or MEE of these enzymes: there is almost no leaching from these encapsulated enzymes during many cycles while high apparent leaching is observed in SBA-15. Leaching rate is usually thermodynamically related to the interaction strength between the enzyme and the support. Physisorption is usually much weaker than covalent immobilization. However, when there are many interaction sites such as in the case of encapsulation, the overall interaction strength can be stronger than a single covalent bond. Each large cage in PCN-333 is surrounded by many supertetrahedra containing not only highly concentrated metal sites with polarized coordinating water molecules, but also conjugated organic linkers, which generate an amphiphilic inner sphere inside the cage. The cage can

therefore act as a SMT, providing a strong trapping interaction to both the hydrophilic and hydrophobic parts of the enzyme, which explains the fast enzyme up-take and the negligible enzyme leaching after encapsulation. The strong interaction between the enzyme and the cages in PCN-333 indicates a large equilibrium constant if the loading process is considered as a reaction. The loading process is less reversible, which leads to fast completion of the forward reaction (enzyme loading). Additionally, the small window on each large cage can dynamically reduce the enzyme leaching. In comparison, SBA-15, which has one dimensional (1-D) channels with fully hydrophilic surfaces, can provide only limited interaction to immobilized enzymes and lead to very significant enzyme leaching during catalysis and recycling processes.

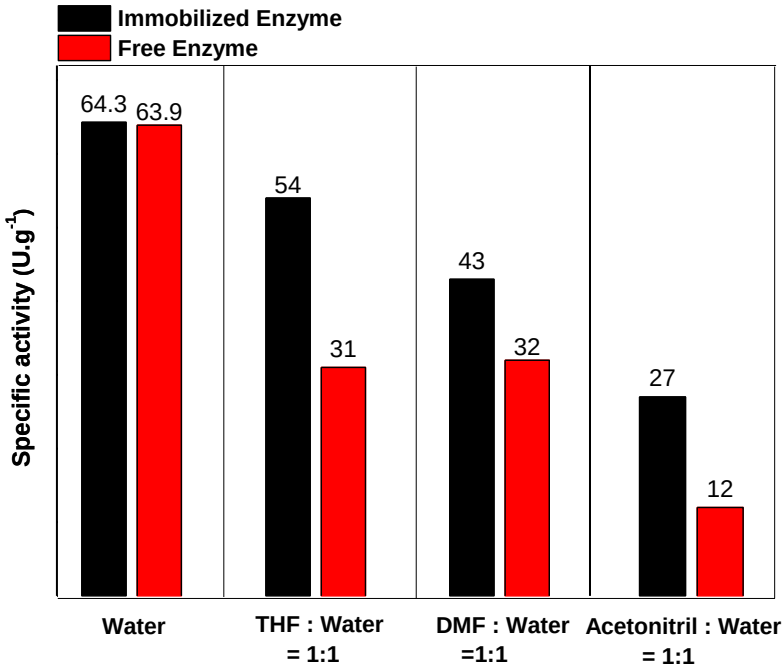

Figure 29. Specific activities of **PCN-333(Al)** immobilized HRP and free HRP in different organic solvent mixture.

After the encapsulation of enzymes in PCN-333(Al), enzymatic catalysis in organic solvents, an important field in the biotechnological applications of proteins,[150] can be conducted more easily by overcoming the solubility issues for both enzymes in organic media and substrates in aqueous media. The encapsulated HRP shows higher catalytic activity in THF-water media than it does in pure water, and much higher activity than free HRP under the same condition.

Table 11. Comparison of kinetic parameters for free and immobilized enzymes under buffered conditions.

Enzymes		K_m (mM)	k_{cat} (min^{-1})	k_{cat}/K_m (min^{-1}. mM^{-1})
HRP	PCN Immobilized	0.84	1.54×10^4	1.833×10^4
	Free	1.8	4.52×10^4	2.51×10^4
Cyt C	PCN Immobilized	14.9	32.2	2.16
	Free	48.3	65.8	1.36
MP-11	PCN Immobilized	2.15	27.9	12.98
	Free	3.28	80.2	24.45

Table 12. Comparison of kinetic parameters for free and immobilized Cyt C in aqueous media.

	K_m (mM)	k_{cat} (min^{-1})	k_{cat}/K_m (min^{-1}. mM^{-1})
PCN Immobilized Cyt C	6.8	197	28.97
Free Cyt C	109.4	109	1.00

3.4 Conclusions

In summary, by using an exceptionally water-stable MOF containing meso-cages that can act as single molecule traps for the encapsulation of a single enzyme molecule in one cage, essentially eliminating enzyme aggregation and leaching, immobilized enzymes with recyclability and high catalytic efficiency in harsh condition have been discovered. The single enzyme encapsulation concept will revolutionize the application of enzymes in industry, enabling the application of enzymes in fundamental processes such as nitrogen fixation, hydrogen production, and the conversion of natural gas into liquid fuels of high energy density with unprecedented efficiency.

4. KINETICALLY TUNED DIMENSIONAL AUGMENTATION AS A VERSATILE SYNTHETIC ROUTE TOWARDS ROBUST METAL–ORGANIC FRAMEWORKS *

4.1 Introduction

Metal-organic frameworks (MOFs) with good stability have been pursued for many years.[12-15] Chemically stable MOFs, which are resistant to reactive species, are of critical importance to a variety of applications, including gas storage, carbon capture, separations, and catalysis[4-10]. In particular, robust MOFs that are easy to scale up and moisture-resistant with high gas storage capacity are needed for automotive applications. However, making robust MOFs with desired structure, porosity, and internal surface properties has always been a challenge. Almost all MOFs, in particular moisture-resistant MOFs constructed with high-valence metal ions, have been made from the "one-pot" synthetic route, making it difficult to control the metal-containing nodes and therefore the topology of the MOF [16].

Problems arise when targeting chemically stable MOFs through conventional one-pot reactions: The overall design of novel MOFs with expected structures, even simple functionalization of existing MOFs for targeted applications, becomes very challenging

---

* Reproduced with permission from: Feng, D.; Wang, K.; Wei, Z.;Chen, Y.-P.; Simon, C. M.; Arvapally, R. K.; Martin, R. L.; Bosch, M.; Liu, T.-F.; Fordham, S.; Yuan, D.; Omary, M. A.; Haranczyk, M.; Smit, B.; Zhou, H.-C. "Kinetically tuned dimensional augmentation as a versatile synthetic route towards robust metal–organic frameworks" *Nature Comm*, **2014**, *5:5723* Copyright 2014 Nature Publishing Group.

because of the unpredictable *in situ* formation of inorganic building blocks; mixed phases often come out together due to the formation of diverse inorganic building blocks; polycrystalline or even amorphous products are prone to form [149], which not only bring challenges in structure determination, but also influence the properties of the targeted products. To address these problems, we present a general method, which is derived from the rationalization of the MOF growth process from both a kinetic and a thermodynamic perspective, of synthesizing Fe-MOF single crystals with preformed inorganic building blocks $[Fe_2M(\mu_3\text{-}O)(CH_3COO)_6]$ (M = $Fe^{2+,3+}$, Co^{2+}, Ni^{2+}, Mn^{2+}, Zn^{2+}). Overall, we synthesized large single crystals of thirty-four different Fe-MOFs with thirty different ligands and mixed ligands by rationally tuning the synthetic conditions. Among them, PCN-250(Fe_2Co) (PCN stands for porous coordination network), which is stable in H_2O for more than six months, exhibits not only one of the highest total CH_4 uptakes of 200 V STP /V at 35 bar and 298 K, but also one of the highest total H_2 volumetric uptakes of 60 gL^{-1} at 40 bar and 77 K.[150]

4.2 Experimental Section

General Information Unless otherwise mentioned, all the reagents were purchased and used without further purification. NMR spectra were recorded on MERCURY 300 (^1H 300 MHz). The following abbreviations were used to explain the multiplicities: s = singlet, d = doublet, t = triplet, q = quartet, m = multiplet, b = broad. The abbreviation for some solvent and reagent were listed here: p-Toluenesulfonate (*Tos*). 1,2-

Dimethoxyethane (DME). tris-*o*-tolylphosphine (P(o-Tolyl)$_3$). N-Methyl-2-pyrrolidone (NMP). The ligands used were purchased from Sigma Aldrich or VWR and used without further purification.

The Synthesis of PCN-233 L10 (15 mg), Fe_2Co (15 mg) and acetic acid (0.4ml) in 2 mL of DMF were ultrasonically dissolved in a Pyrex vial. The mixture was heated in 120 ºC oven for 12 h. After cooling down to room temperature, dark brown crystals were harvested by filtration.

The Synthesis of PCN-234 L11 (8 mg), Fe_3 (15 mg) and acetic acid (0.4 ml) in 2 mL of H_2O were ultrasonically dissolved in a Pyrex vial. The mixture was heated in 120 ºC oven for 12 h. After cooling down to room temperature, dark brown crystals were harvested by filtration.

The Synthesis of PCN-235 L11 (15 mg), Fe_2Co (15 mg) and acetic acid (0.2 ml) in 2 mL of DMF were ultrasonically dissolved in a Pyrex vial. The mixture was heated in 150 ºC oven for 24 h. After cooling down to room temperature, dark brown crystals were harvested by filtration.

The Synthesis of PCN-236 L13 (15 mg), Fe_2Co (15 mg) and acetic acid (0.1 ml) in 2 mL of DMF were ultrasonically dissolved in a Pyrex vial. The mixture was heated in 150 ºC oven for 12 h. After cooling down to room temperature, dark brown crystals were harvested by filtration.

The Synthesis of PCN-237 L12 (15 mg), Fe_2Co (15 mg) and acetic acid (0.2 ml) in 2 mL of NMP were ultrasonically dissolved in a Pyrex vial. The mixture was heated in

150 ºC oven for 12 h. After cooling down to room temperature, dark brown crystals were harvested by filtration.

The Synthesis of PCN-238 L14 (15 mg), Fe_2Co (15 mg) and acetic acid (0.1 ml) in 2 mL of NMP were ultrasonically dissolved in a Pyrex vial. The mixture was heated in 150 ºC oven for 12 h. After cooling down to room temperature, dark brown crystals were harvested by filtration.

The Synthesis of PCN-240 L3 (10mg), Fe_2Co (10 mg) and acetic acid (0.25 ml) in 2 mL of DEF and H_2O (v / v = 1 / 1) were ultrasonically dissolved in a Pyrex vial. The mixture was heated in 150 ºC oven for 24 h. After cooling down to room temperature, dark brown crystals were harvested by filtration.

The Synthesis of PCN-241 L4 (10mg), Fe_2Co (15 mg) and acetic acid (0.8 ml) in 2 mL of DMF were ultrasonically dissolved in a Pyrex vial. The mixture was heated in 150 ºC oven for 12 h. After cooling down to room temperature, dark brown crystals were harvested by filtration.

The Synthesis of PCN-242 L2 (10mg), Fe_3 (10 mg) and acetic acid (0.45 ml) in 2 mL of DMF were ultrasonically dissolved in a Pyrex vial. The mixture was heated in 150 ºC oven for 12 h. After cooling down to room temperature, dark brown crystals were harvested by filtration.

The Synthesis of PCN-243 L8 (10mg), Fe_3 (10 mg) and acetic acid (0.45 ml) in 2 mL of DMF were ultrasonically dissolved in a Pyrex vial. The mixture was heated in 150 ºC oven for 48 h. After cooling down to room temperature, dark brown crystals were harvested by filtration.

The Synthesis of PCN-245 L5 (10mg), Fe_3 (10 mg) and acetic acid (0.15 ml) in 2 mL of DMF were ultrasonically dissolved in a Pyrex vial. The mixture was heated in 150 ºC oven for 12 h. After cooling down to room temperature, dark brown crystals were harvested by filtration.

The Synthesis of PCN-246 L7 (10mg), Fe_3 (15 mg) and acetic acid (0.2ml) in 2 mL of DMF were ultrasonically dissolved in a Pyrex vial. The mixture was heated in 120 ºC oven for 12 h. After cooling down to room temperature, dark brown crystals were harvested by filtration.

The Synthesis of PCN-247 L6 (10 mg), Fe_3 (15 mg) and acetic acid (0.35 ml) in 2 mL of DMF were ultrasonically dissolved in a Pyrex vial. The mixture was heated in 150 ºC oven for 12 h. After cooling down to room temperature, dark brown crystals were harvested by filtration.

The Synthesis of PCN-248 L9 (10mg), Fe_2Co or Fe_3 (10 mg) and acetic acid (0.25 ml) in 2 mL of NMP were ultrasonically dissolved in a Pyrex vial. The mixture was heated in 150 ºC oven for 24 h. After cooling down to room temperature, dark brown crystals were harvested by filtration.

The Synthesis of PCN-250 L22 (10 mg), Fe_2M (Mn,Fe,Co,Ni,Zn) (15 mg) and acetic acid (1 ml) in 2 mL of DMF were ultrasonically dissolved in a Pyrex vial. The mixture was heated in 140 ºC oven for 12 h. After cooling down to room temperature, dark brown crystals were harvested by filtration.

Figure 30. Large scale synthesis of PCN-250(Fe_2Co).

The Synthesis of PCN-250' L22 (10 mg), Fe_2M(Mn,Fe,Co,Ni,Zn) (15 mg) and acetic acid (1 ml) in 2 mL of NMP were ultrasonically dissolved in a Pyrex vial. The mixture was heated in 140 ºC oven for 12 h. After cooling down to room temperature, dark brown crystals were harvested by filtration.

The Synthesis of PCN-251 L22 (10 mg), Fe_2M (Mn,Fe,Co,Ni,Zn) (15 mg) and acetic acid (1 ml) in 2 mL of NMP were ultrasonically dissolved in a Pyrex vial. The mixture was heated in 140 ºC oven for 12 h. After cooling down to room temperature, dark brown crystals were obtained.

The Synthesis of PCN252 L23 (10 mg), Fe_2M (Mn,Fe,Co,Ni, Zn) (10 mg) and acetic acid (0.8 ml) in 2 mL of NMP were ultrasonically dissolved in a Pyrex vial. The mixture was heated in 150 ºC oven for 12 h. After cooling down to room temperature, dark brown crystals were harvested by filtration.

Single-Crystal X-ray Crystallography The data frames were collected using the program APEX2 and processed using the program SAINT routine within APEX2. The data were corrected for absorption and beam corrections based on the multi-scan technique as implemented in SADABS. The structure was solved by direct methods using the SHELXS program of the SHELXTL package and refined by full-matrix least-squares methods with SHELXL. Metal atoms were located from the E-maps and other non-hydrogen atoms were refined with anisotropic displacement parameters during the final cycles. Hydrogen atoms were placed in calculated positions with isotropic displacement parameters set to 1.2 × Ueq of the attached atom. The solvent molecules are highly disordered, and attempts to locate and refine the solvent peaks were unsuccessful. Contributions to scattering due to these solvent molecules were removed using the SQUEEZE routine of PLATON; structures were then refined again using the data generated. The contents of the solvent region are not represented in the unit cell contents in the crystal data.

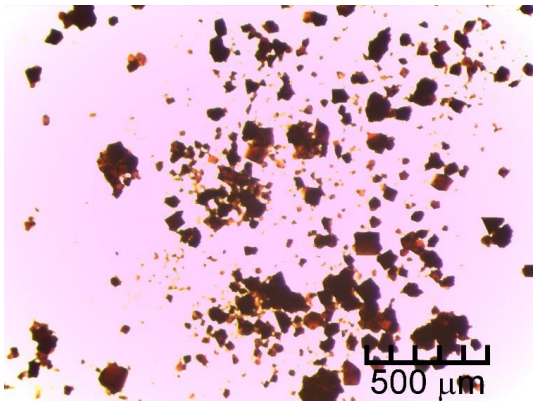

(a)

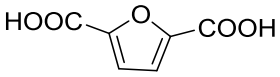

(b)

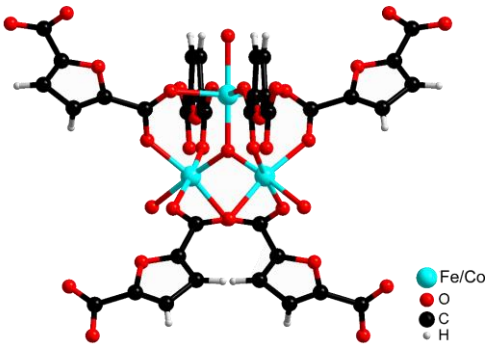

(c)

Figure 31. (a) Optical microscope image of solvated PCN-233. (b) Ligand used in PCN-233. (c) Fragment structure of PCN-233.

Table 13. Crystal data and structure refinements for PCN-233. (CCDC 975771)

Compound PCN-233		Absolute structure parameter : 0.24(3)	
Formula	$Fe_2 Co_1 C_{18} H_6 O_{19}$	$\mu(mm^{-1})$	0.960
Fw	696.86	*F*(000)	690
Color/Shape	Brown Square	θ_{max} [deg]	26.73
Crystal system	Monoclinic	Completeness	98.2%
Space group	*C*2	Collected reflections	9633
a (Å)	16.697(9)	Unique reflections	4977
b (Å)	13.848(9)	Parameters	182
c (Å)	10.873(5)	Restraints	8
α ( )	90.00	R_{int}	0.0802
β ( )	101.62(5)	*R*1 [I > 2σ(I)]	0.0615
γ ( )	90.00	*wR*2 [I > 2σ(I)]	0.1083
V ($Å^3$)	2463(2)	*R*1 (all data)	0.1031
Z	2	*wR*2 (all data)	0.1147
T (*K*)	110(2)	GOF on F^2	0.958
$d_{calcd.}$ (g/cm^3)	0.940	$\Delta\rho_{max}$/ $\Delta\rho_{min}$ [$e \cdot Å^3$]	0.762 / -0.480

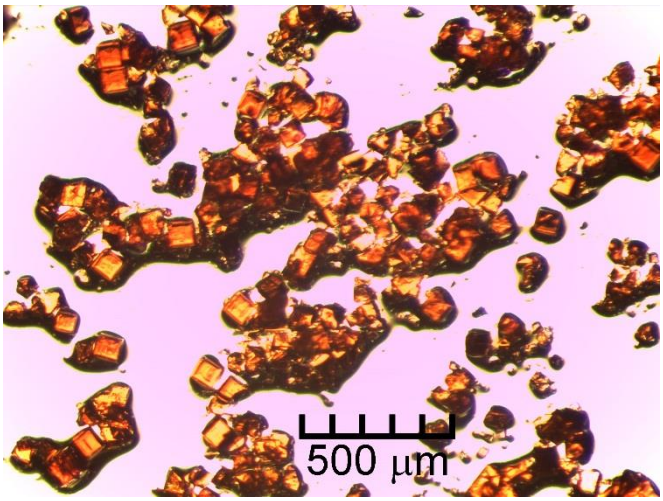

(a)

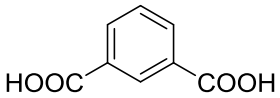

(b)

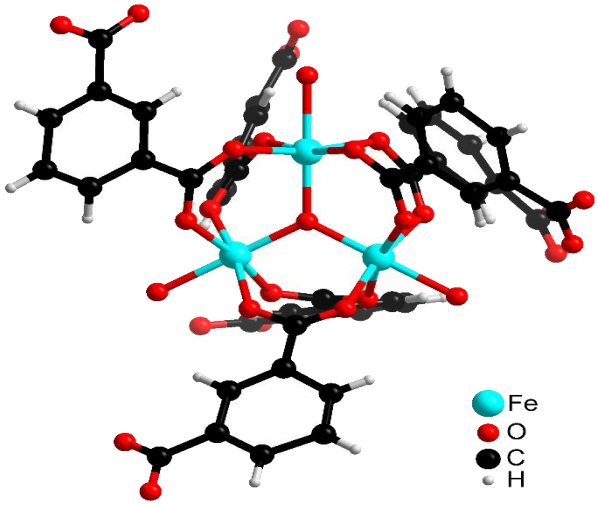

(c)

Figure 32. (a) Optical microscope image of solvated PCN-234. (b) Ligand used in PCN-234. (c) Fragment structure of PCN-234.

Table 14. Crystal data and structure refinements for PCN-234. (CCDC 975772)

Compound PCN-234			
Formula	$Fe_3 C_{24} H_{13} O_{16}$	$\mu(mm^{-1})$	1.284
Fw	724.89	*F*(000)	2904
Color/Shape	Orange Cube	θ_{max} [deg]	23.98
Crystal system	Cubic	Completeness	99.4%
Space group	$Pa\bar{3}$	Collected reflections	58247
a (Å)	19.153(3)	Unique reflections	1824
b (Å)	19.153(3)	Parameters	82
c (Å)	19.153(3)	Restraints	12
α (°)	90.00	R_{int}	0.1253
β (°)	90.00	*R*1 [I > 2σ(I)]	0.1687
γ (°)	90.00	*wR*2 [I > 2σ(I)]	0.3399
V (Å^3)	7026.6(19)	*R*1 (all data)	0.1968
Z	8	*wR*2 (all data)	0.3534
T (*K*)	110(2)	GOF on F^2	1.008
$d_{calcd.}$ (g/cm^3)	1.370	$\Delta\rho_{max}$/ $\Delta\rho_{min}$ [e·Å^3]	0.952 / -1.243

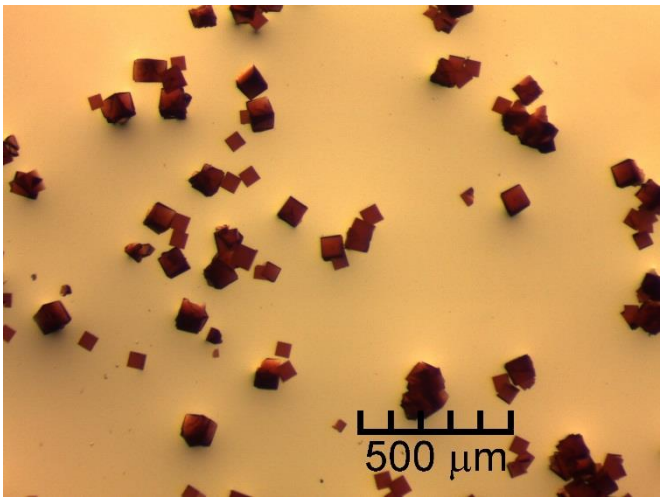

(a)

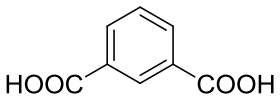

(b)

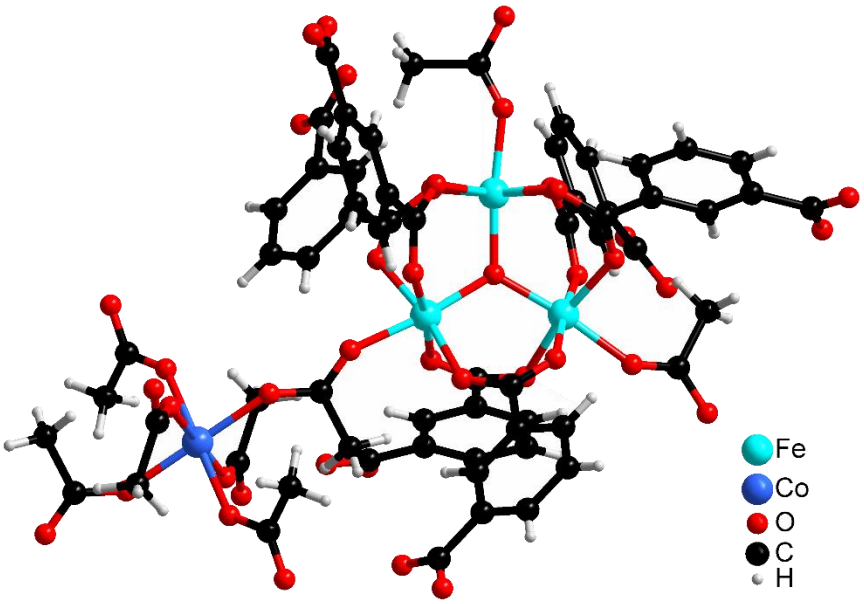

(c)

Figure 33. (a) Optical microscope image of solvated PCN-235. (b) Ligand used in PCN-235. (c) Fragment structure of PCN-235.

Table 15. Crystal data and structure refinements for PCN-235. (CCDC 975773)

Compound PCN-235			
Formula	Fe_6 Co C_{60} H_{44} O_{38}	μ(mm^{-1})	1.423
Fw	1766.98	*F*(000)	3564
Color/Shape	Brown Cube	θ_{max} [deg]	25.88
Crystal system	Cubic	Completeness	99.9%
Space group	*Pa* $\bar{3}$	Collected reflections	54302
a (Å)	19.627(7)	Unique reflections	2451
b (Å)	19.627(7)	Parameters	155
c (Å)	19.627(7)	Restraints	1
α (°)	90.00	R_{int}	0.1276
β (°)	90.00	*R*1 [I > 2σ(I)]	0.0671
γ (°)	90.00	*wR*2 [I > 2σ(I)]	0.1668
V ($Å^3$)	7561(5)	*R*1 (all data)	0.0899
Z	4	*wR*2 (all data)	0.1817
T (*K*)	110(2)	GOF on F^2	1.002
$d_{calcd.}$ (g/cm^3)	1.552	$\Delta\rho_{max}$/ $\Delta\rho_{min}$ [$e \cdot Å^3$]	0.828 / -2.060

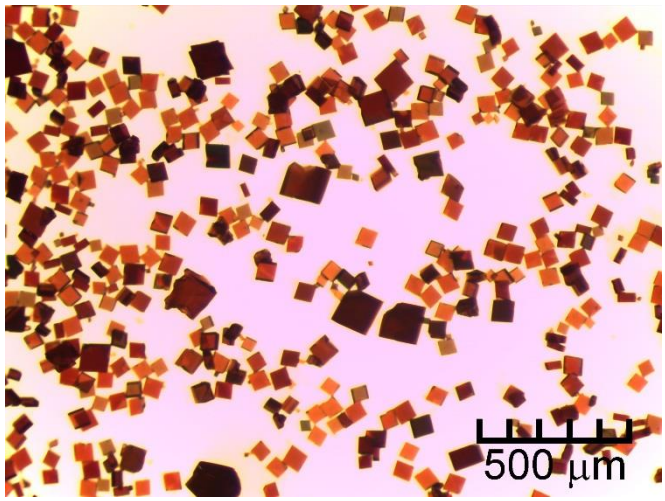

(a)

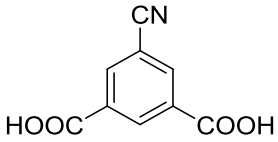

(b)

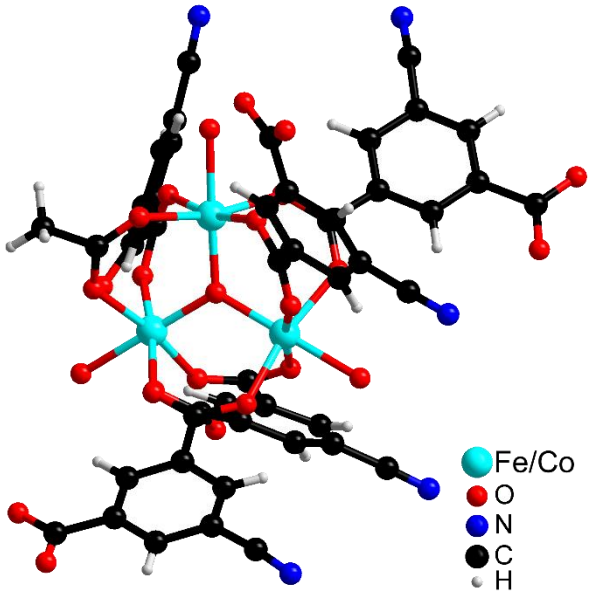

(c)

Figure 34. (a) Optical microscope image of solvated PCN-236. (b) Ligand used in PCN-236. (c) Fragment structure of PCN-236.

Table 16. Crystal data and structure refinements for PCN-236. (CCDC 975774)

Compound PCN-236			
Formula	Fe_4 Co_2 $C_{49}H_{21}$ N_5 O_{32}	μ(mm^{-1})	0.748
Fw	1532.97	*F*(000)	3056
Color/Shape	Brown Square	θ_{max} [deg]	26.59
Crystal system	Orthorhombic	Completeness	99.5%
Space group	*Pnna*	Collected reflections	132886
a (Å)	19.635(3)	Unique reflections	13207
b (Å)	36.750(6)	Parameters	320
c (Å)	17.556(3)	Restraints	48
α (°)	90.00	R_{int}	0.1102
β (°)	90.00	*R*1 [I > 2σ(I)]	0.0699
γ (°)	90.00	*wR*2 [I > 2σ(I)]	0.1822
V ($Å^3$)	12668(3)	*R*1 (all data)	0.1699
Z	4	*wR*2 (all data)	0.2057
T (*K*)	110(2)	GOF on F^2	1.001
$d_{calcd.}$ (g/cm^3)	0.804	$\Delta\rho_{max}$/ $\Delta\rho_{min}$ [$e \cdot Å^3$]	0.638 / -0.576

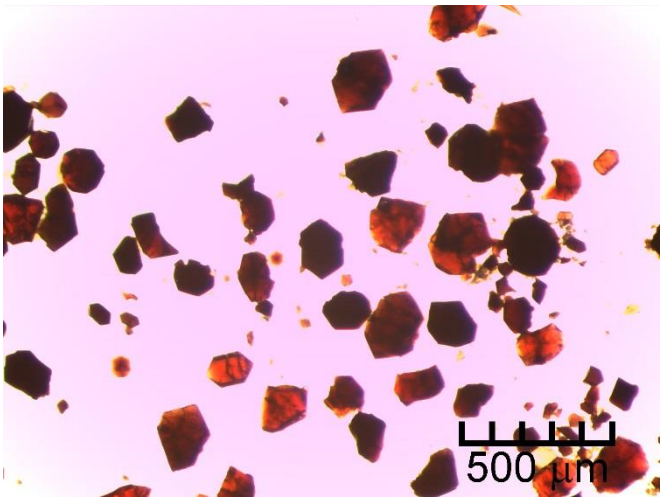

(a)

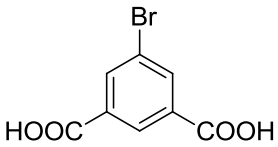

(b)

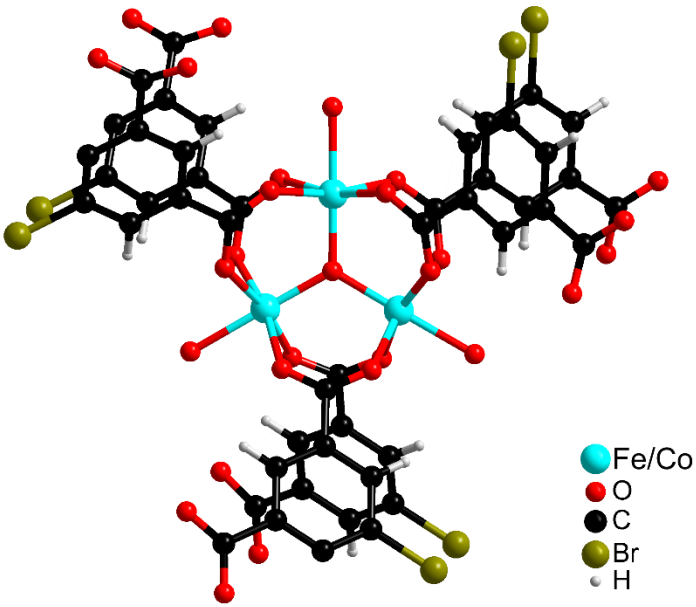

(c)

Figure 35. (a) Optical microscope image of solvated PCN-237. (b) Ligand used in PCN-237. (c) Fragment structure of PCN-237.

Table 17. Crystal data and structure refinements for PCN-237. (CCDC 975775)

Compound PCN-237		Absolute structure parameter : 0.02(5)	
Formula	$Fe_2\ Co_1\ C_{24}\ H_9\ Br_3\ O_{16}$	$\mu(mm^{-1})$	3.279
Fw	963.67	*F*(000)	930
Color/Shape	Brown Hexagon	θ_{max} [deg]	27.14
Crystal system	Hexagonal	Completeness	99.5%
Space group	$P\bar{6}2c$	Collected reflections	15835
a (Å)	15.392(4)	Unique reflections	1974
b (Å)	15.392(4)	Parameters	96
c (Å)	12.425(3)	Restraints	31
α (°)	90.00	R_{int}	0.0674
β (°)	90.00	*R*1 [I > 2σ(I)]	0.0741
γ (°)	120.00	*wR*2 [I > 2σ(I)]	0.1530
V (Å^3)	2549.4(12)	*R*1 (all data)	0.1032
Z	2	*wR*2 (all data)	0.1635
T (*K*)	110(2)	GOF on F^2	1.010
$d_{calcd.}$ (g/cm^3)	1.255	$\Delta\rho_{max}$/ $\Delta\rho_{min}$ [e·Å^3]	1.144 / -0.504

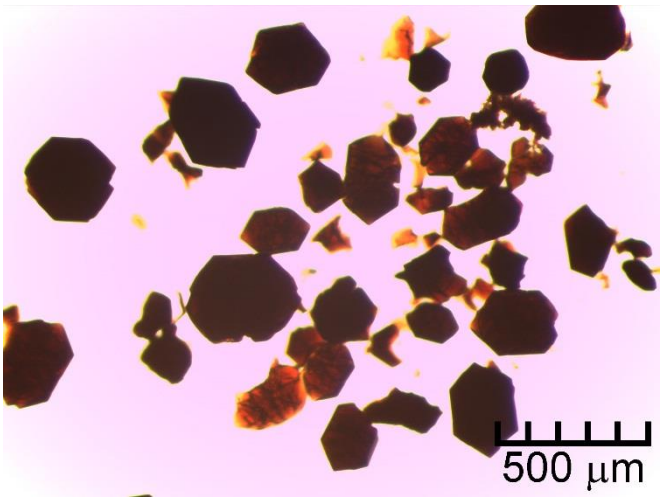

(a)

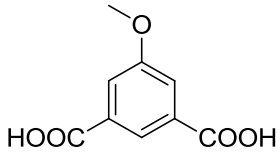

(b)

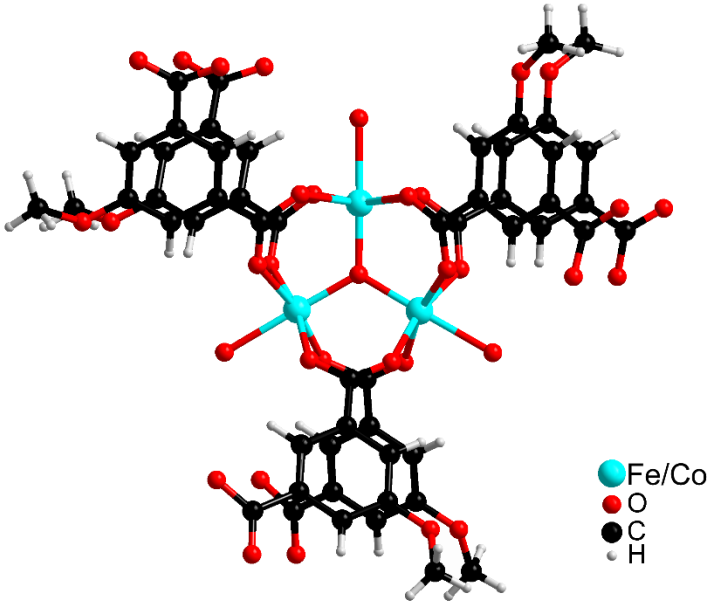

(c)

Figure 36. (a) Optical microscope image of solvated PCN-238. (b) Ligand used in PCN-238. (c) Fragment structure of PCN-238.

Table 18. Crystal data and structure refinements for PCN-238. (CCDC 975776)

Compound PCN-238		Absolute structure parameter : 0.05(11)	
Formula	Fe_2 Co_1 C_{27} H_{18} O_{19}	μ(mm^{-1})	0.924
Fw	817.04	*F*(000)	822
Color/Shape	Brown Hexagon	θ_{max} [deg]	24.65
Crystal system	Hexagonal	Completeness	99.3%
Space group	$P\bar{6}2c$	Collected reflections	21511
a (Å)	15.460(4)	Unique reflections	1524
b (Å)	15.460(4)	Parameters	75
c (Å)	12.475(14)	Restraints	29
α (°)	90.00	R_{int}	0.1164
β (°)	90.00	*R*1 [I > 2σ(I)]	0.1213
γ (°)	120.00	*wR*2 [I > 2σ(I)]	0.2296
V ($Å^3$)	2582(3)	*R*1 (all data)	0.1591
Z	2	*wR*2 (all data)	0.2475
T (*K*)	110(2)	GOF on F^2	1.013
$d_{calcd.}$ (g/cm^3)	1.051	$\Delta\rho_{max}$/ $\Delta\rho_{min}$ [$e \cdot Å^3$]	0.832 / -0.398

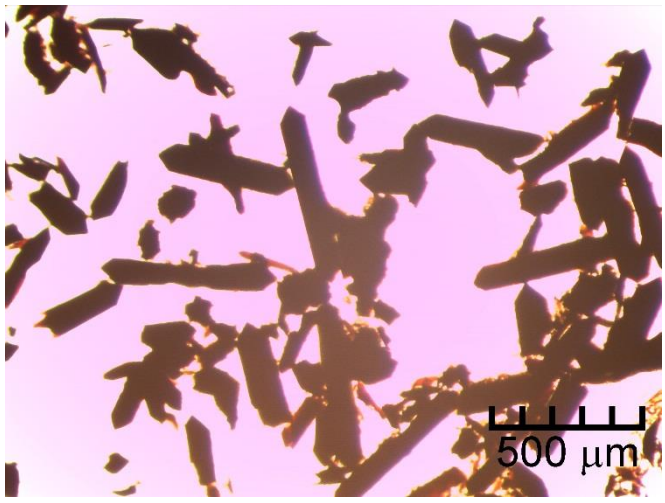

(a)

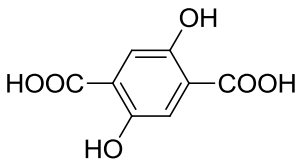

(b)

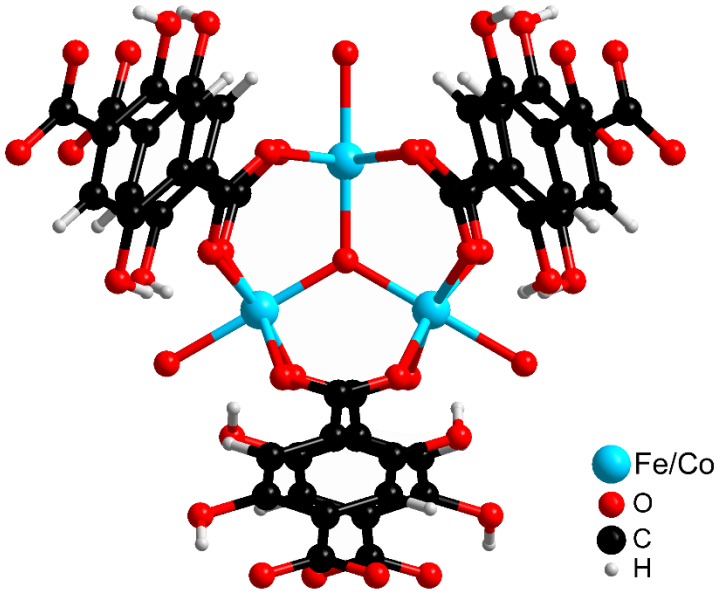

(c)

Figure 37. (a) Optical microscope image of solvated PCN-240. (b) Ligand used in PCN-240. (c) Fragment structure of PCN-240.

Table 19. Crystal data and structure refinements for PCN-240. (CCDC 975777)

Compound PCN-240			
Formula	Fe_2 Co C_{24} H_{12} O_{22}	μ(mm^{-1})	0.767
Fw	822.97	*F*(000)	822
Color/Shape	Brown Rod	θ_{max} [deg]	24.55
Crystal system	Hexagonal	Completeness	99.9%
Space group	*P* 63 /*mmc*	Collected reflections	28022
a (Å)	14.392(3)	Unique reflections	1029
b (Å)	14.392(3)	Parameters	52
c (Å)	17.416(5)	Restraints	0
α ( )	90.00	R_{int}	0.1240
β ( )	90.00	*R*1 [I > 2σ(I)]	0.0625
γ ( )	120.00	*wR*2 [I > 2σ(I)]	0.1447
V ($Å^3$)	3124.1(13)	*R*1 (all data)	0.0865
Z	2	*wR*2 (all data)	0.1563
T (*K*)	110(2)	GOF on F^2	1.006
$d_{calcd.}$ (g/cm^3)	0.875	$\Delta\rho_{max}$/ $\Delta\rho_{min}$ [e·$Å^3$]	1.025 / -0.468

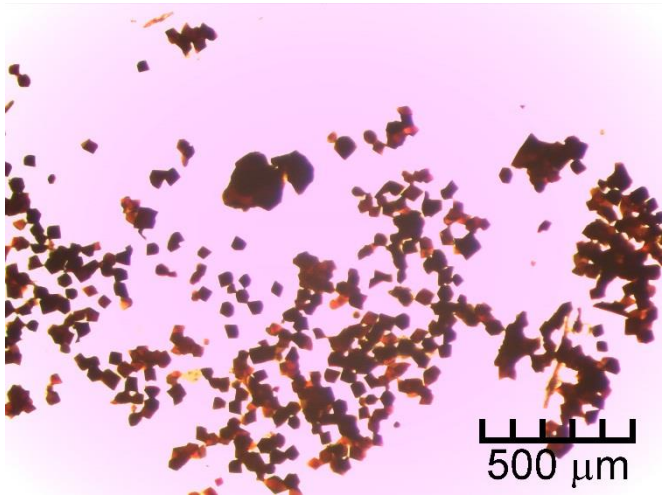

(a)

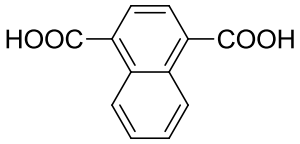

(b)

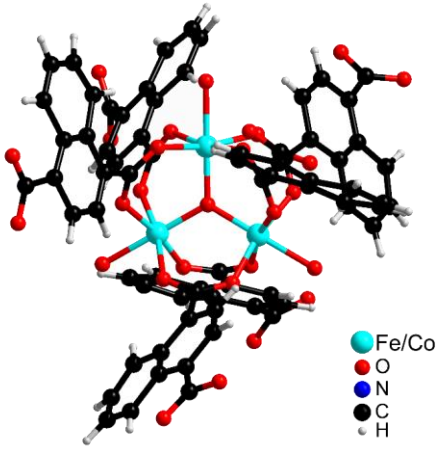

(c)

Figure 38. (a) Optical microscope image of solvated PCN-241. (b) Ligand used in PCN-241. (c) Fragment structure of PCN-241.

Table 20. Crystal data and structure refinements for PCN-241. (CCDC 975778)

Compound PCN-241		Absolute structure parameter : 0.09(5)	
Formula	Fe_2 Co C_{45} H_{39} N_3 O_{16}	μ(mm^{-1})	0.967
Fw	1048.42	*F*(000)	1074
Color/Shape	Brown Sheet	θ_{max} [deg]	24.8
Crystal system	Hexagonal	Completeness	99.9%
Space group	*P* 31*c*	Collected reflections	22992
a (Å)	12.493(2)	Unique reflections	2886
b (Å)	12.493(2)	Parameters	207
c (Å)	18.533(3)	Restraints	1
α ( )	90.00	R_{int}	0.0771
β ( )	90.00	*R*1 [I > 2σ(I)]	0.0690
γ ( )	120.00	*wR*2 [I > 2σ(I)]	0.1869
V ($Å^3$)	2504.9(7)	*R*1 (all data)	0.0739
Z	2	*wR*2 (all data)	0.1912
T (*K*)	110(2)	GOF on F^2	1.006
$d_{calcd.}$ (g/cm^3)	1.390	$\Delta\rho_{max}$/ $\Delta\rho_{min}$ [$e \cdot Å^3$]	0.799 / -0.618

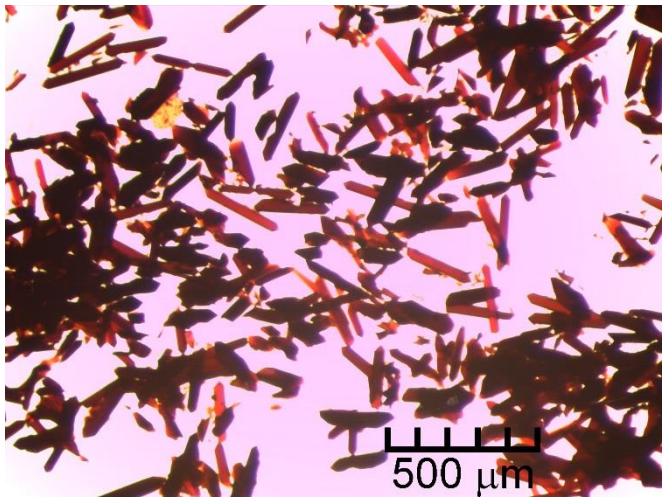

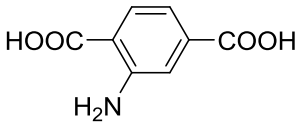

(a) (b)

Figure 39. (a) Optical microscope image of solvated PCN-242. (b) Ligand used in PCN-242.

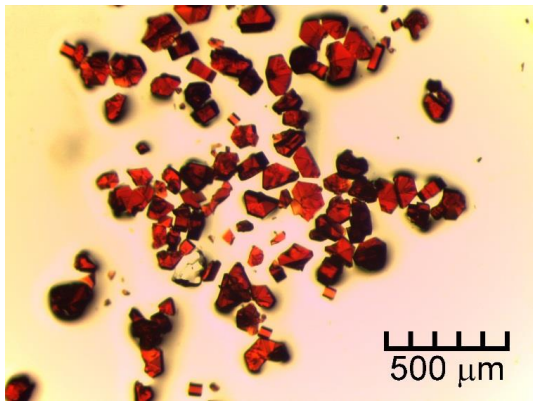

(a)

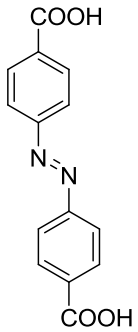

(b)

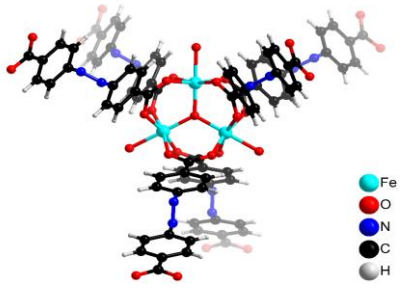

(c)

Figure 40. (a) Optical microscope image of solvated PCN-243. (b) Ligand used in PCN-243. (c) Fragment structure of PCN-243.

Table 21. Crystal data and structure refinements for PCN-243. (CCDC 975779)

Compound PCN-243		Absolute structure parameter: 0.47(15)	
Formula	Fe_6 C_{84} H_{48} N_{12} O_{32}	μ(mm^{-1})	0.797
Fw	2072.44	*F*(000)	3144
Color/Shape	Red Hexagonal Prism	θ_{max} [deg]	23.29
Crystal system	Hexagonal	Completeness	99.9%
Space group	$P6_3mc$	Collected reflections	71186
a (Å)	18.6996(8)	Unique reflections	4662
b (Å)	18.6996(8)	Parameters	153
c (Å)	28.8572(18)	Restraints	84
α ( )	90.00	R_{int}	0.0353
β ( )	90.00	*R*1 [I > 2σ(I)]	0.1487
γ ( )	120.00	*wR*2 [I > 2σ(I)]	0.2802
V ($Å^3$)	8738.8(8)	*R*1 (all data)	0.1589
Z	3	*wR*2 (all data)	0.2849
T (*K*)	110 (2)	GOF on F^2	0.842
$d_{calcd.}$ (g/cm^3)	1.181	$\Delta\rho_{max}$/ $\Delta\rho_{min}$ [$e \cdot Å^3$]	2.284 / -1.561

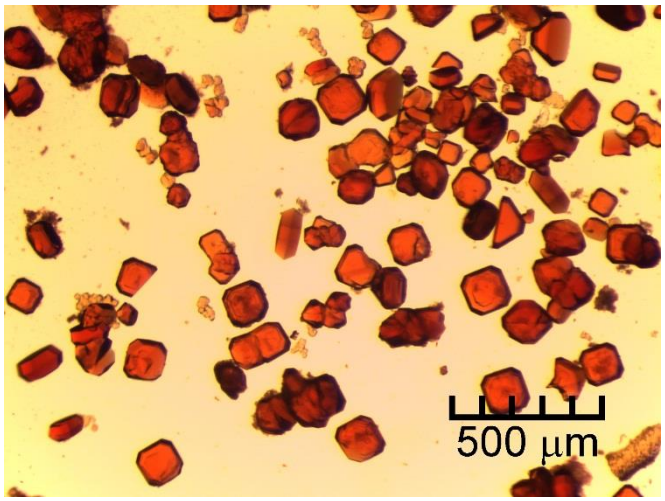

(a)

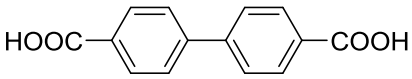

(b)

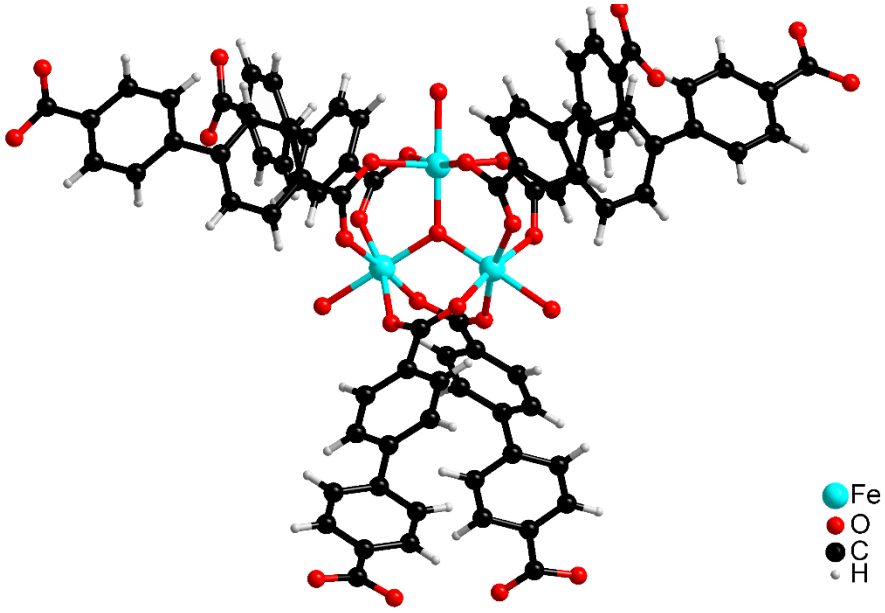

(c)

Figure 41. (a) Optical microscope image of solvated PCN-245. (b) Ligand used in PCN-245. (c) Fragment structure of PCN-245.

Table 22. Crystal data and structure refinements for PCN-245. (CCDC 975780)

Compound PCN-245		Absolute structure parameter : 0.04(3)	
Formula	$Fe_3 C_{42} H_{24} O_{16}$	$\mu(mm^{-1})$	0.550
Fw	952.16	*F*(000)	3856
Color/Shape	Orange Square Bulk	θ_{max} [deg]	21.77
Crystal system	Tetragonal	Completeness	99.0%
Space group	$P4_32_12$	Collected reflections	60402
a (Å)	21.757(11)	Unique reflections	9857
b (Å)	21.757(11)	Parameters	245
c (Å)	35.299(18)	Restraints	0
α ( )	90.00	R_{int}	0.1889
β ( )	90.00	*R*1 [I > 2σ(I)]	0.0639
γ ( )	90.00	*wR*2 [I > 2σ(I)]	0.1337
V ($Å^3$)	16709(14)	*R*1 (all data)	0.0961
Z	8	*wR*2 (all data)	0.1423
T (*K*)	110(2)	GOF on F^2	1.000
$d_{calcd.}$ (g/cm^3)	0.757	$\Delta\rho_{max}$/ $\Delta\rho_{min}$ [$e \cdot Å^3$]	0.583 / -0.404

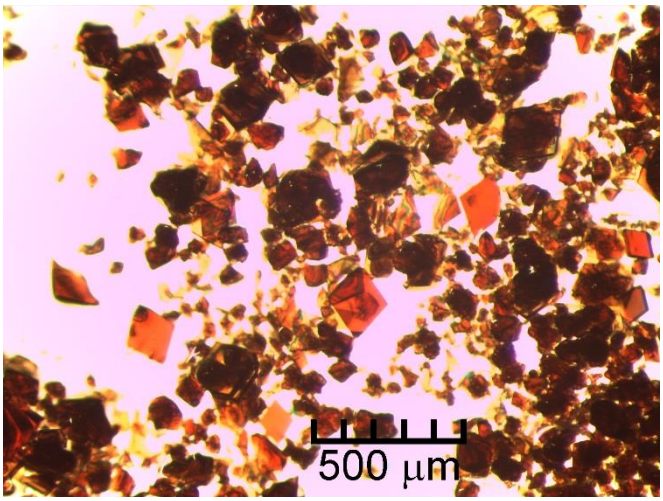

(a)

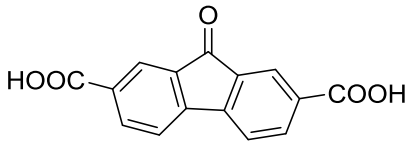

(b)

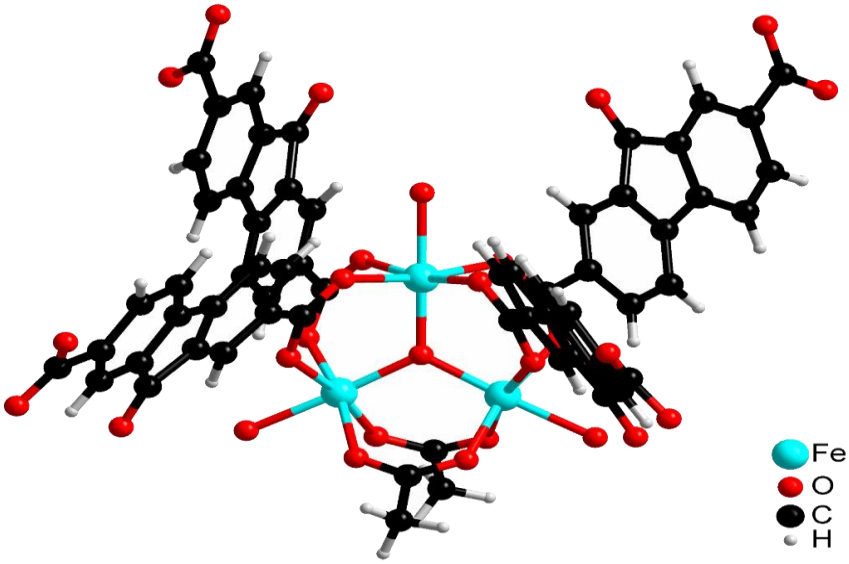

(c)

Figure 42. (a) Optical microscope image of solvated PCN-246. (b) Ligand used in PCN-246. (c) Fragment structure of PCN-246.

Table 23. Crystal data and structure refinements for PCN-246. (CCDC 975781)

Compound PCN-246			
Formula	$Fe_3 C_{34} H_{21} O_{18}$	$\mu(mm^{-1})$	0.618
Fw	885.06	*F*(000)	1788
Color/Shape	Orange Slice	θ_{max} [deg]	26.46
Crystal system	Orthorhombic	Completeness	99.7%
Space group	*Pnma*	Collected reflections	78031
a (Å)	18.358(2)	Unique reflections	7907
b (Å)	15.888(2)	Parameters	266
c (Å)	25.435(3)	Restraints	2
α ( )	90.00	R_{int}	0.0807
β ( )	90.00	*R*1 [I > 2σ(I)]	0.0460
γ ( )	90.00	*wR*2 [I > 2σ(I)]	0.1069
V ($Å^3$)	7418.6(17)	*R*1 (all data)	0.0721
Z	4	*wR*2 (all data)	0.1127
T (*K*)	110(2)	GOF on F^2	1.000
$d_{calcd.}$ (g/cm^3)	0.792	$\Delta\rho_{max}/ \Delta\rho_{min}$ [$e \cdot Å^3$]	0.997 / -0.409

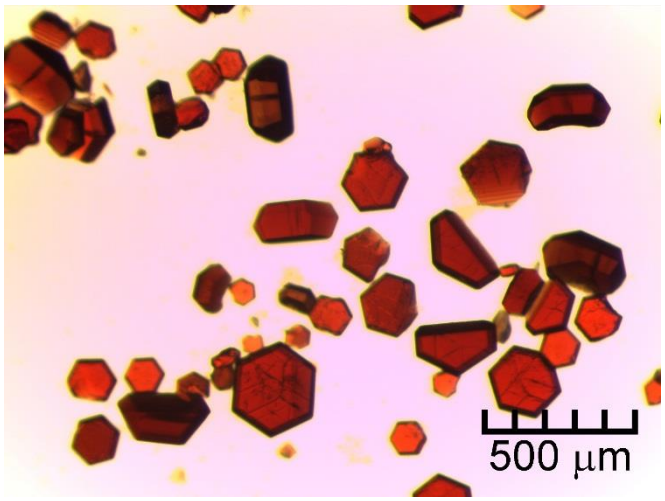

(a)

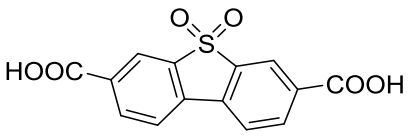

(b)

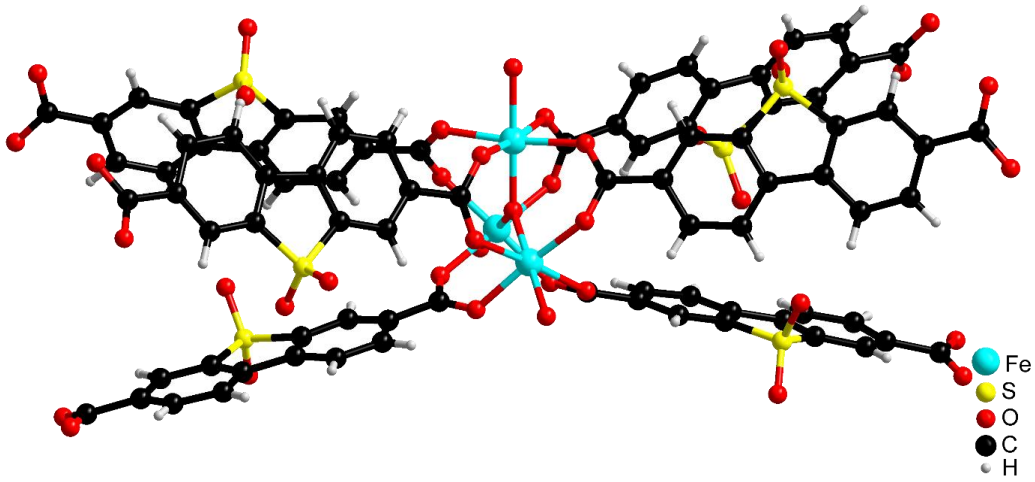

(c)

Figure 43. (a) Optical microscope image of solvated PCN-247. (b) Ligand used in PCN-247. (c) Fragment structure of PCN-247.

Table 24. Crystal data and structure refinements for PCN-247. (CCDC 975782)

Compound PCN-247		Absolute structure parameter : 0.51(5)	
Formula	$Fe_3 C_{42} H_{19} O_{22} S_3$	$\mu(mm^{-1})$	0.739
Fw	1139.30	*F*(000)	1146
Color/Shape	Orange Hexagon	θ_{max} [deg]	26.44
Crystal system	Hexagonal	Completeness	99.7%
Space group	$P6_322$	Collected reflections	29673
a (Å)	12.3081(8)	Unique reflections	2494
b (Å)	12.3081(8)	Parameters	102
c (Å)	27.375(4)	Restraints	0
α ( )	90.00	R_{int}	0.0556
β ( )	90.00	*R*1 [I > 2σ(I)]	0.0601
γ ( )	120.00	*wR*2 [I > 2σ(I)]	0.1320
V ($Å^3$)	3591.4(6)	*R*1 (all data)	0.0691
Z	2	*wR*2 (all data)	0.1364
T (*K*)	110(2)	GOF on F^2	1.002
$d_{calcd.}$ (g/cm^3)	1.054	$\Delta\rho_{max}/ \Delta\rho_{min}$ [$e \cdot Å^3$]	0.598 / -0.516

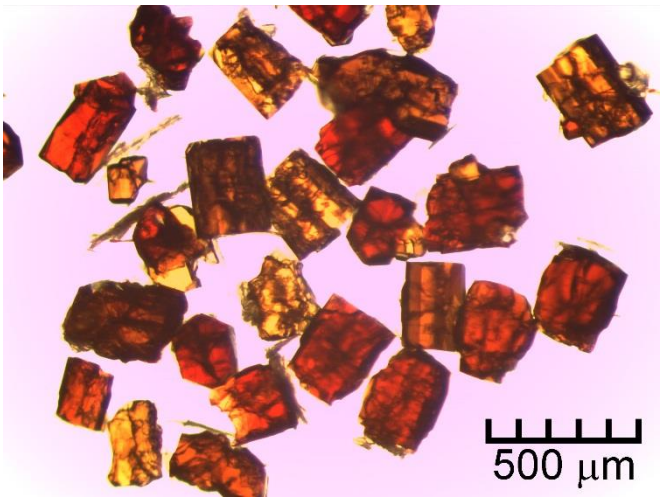

(a)

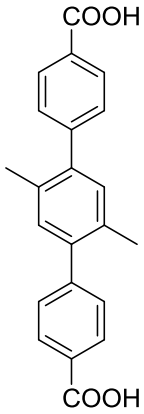

(b)

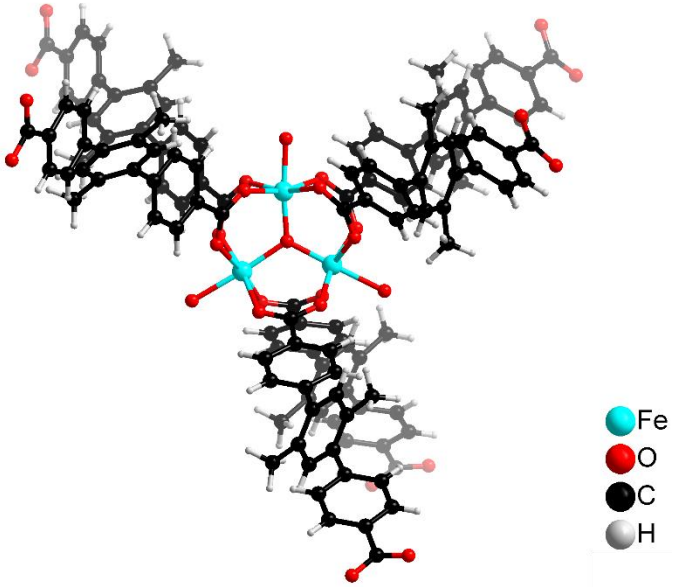

(c)

Figure 44. (a) Optical microscope image of solvated PCN-248. (b) Ligand used in PCN-248. (c) Fragment structure of PCN-248.

Table 25. Crystal data and structure refinements for PCN-248. (CCDC 975783)

Compound PCN-248		Absolute structure parameter :	
Formula*	$Fe_3\ C_{66}\ H_{48}\ O_{16}\ S$	$\mu(mm^{-1})$	0.535
Fw	1296.65	*F*(000)	2664
Color/Shape	Red Bulk	θ_{max} [deg]	24.69
Crystal system	Orthorhombic	Completeness	98.2%
Space group	*Pnma*	Collected reflections	81621
a (Å)	11.870(6)	Unique reflections	7833
b (Å)	31.338(15)	Parameters	266
c (Å)	24.763(12)	Restraints	97
α ( )	90.00	R_{int}	0.1452
β ( )	90.00	*R*1 [I > 2σ(I)]	0.1006
γ ( )	120.00	*wR*2 [I > 2σ(I)]	0.2197
V ($Å^3$)	9211(8)	*R*1 (all data)	0.1398
Z	4	*wR*2 (all data)	0.2365
T (*K*)	110(2)	GOF on F^2	1.002
$d_{calcd.}$ (g/cm^3)	0.935	$\Delta\rho_{max}/\ \Delta\rho_{min}$ [$e\cdot Å^3$]	2.668 / -2.574

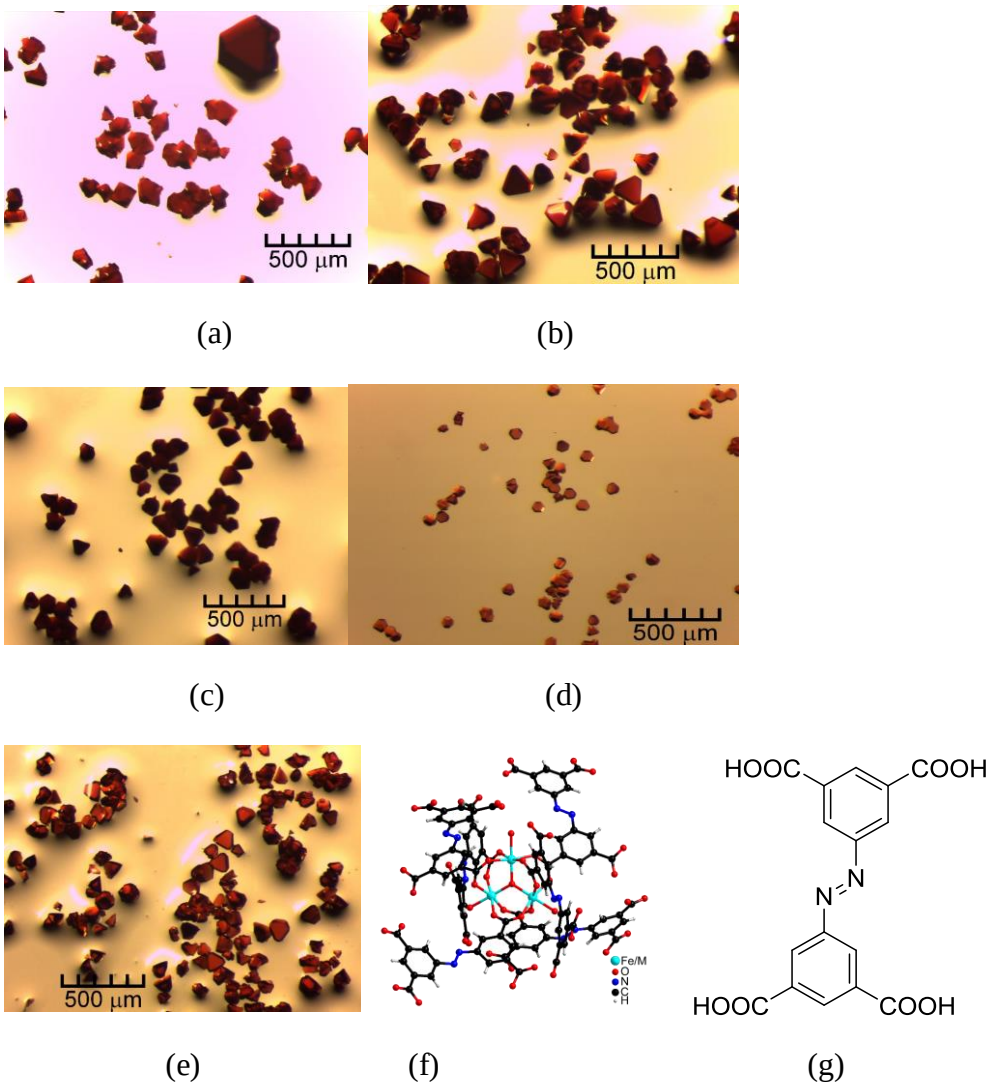

(a) (b)

(c) (d)

(e) (f) (g)

Figure 45. Optical microscope images of solvated (a) PCN-250(Fe_2Co), (b) PCN-250(Fe_3), (c) PCN-250(Fe_2Mn), (d) PCN-250(Fe_2Ni), (e) PCN-250(Zn). (f) Ligand used in PCN-250. (g) Fragment structure of PCN-250(Fe_3).

Table 26. Crystal data and structure refinements for PCN-250 (Fe_3). (CCDC 975784)

Compound PCN-250 (Fe_3)		Absolute structure parameter : 0.51(2)	
Formula	$Fe_6\ C_{48}\ H_{20}\ N_6\ O_{32}$	μ(mm^{-1})	0.855
Fw	1527.80	*F*(000)	3048
Color/Shape	Orange Triangle	θ_{max} [deg]	26.41
Crystal system	Cubic	Completeness	99.9%
Space group	$P\bar{4}3n$	Collected reflections	109367
a (Å)	21.966(3)	Unique reflections	3644
b (Å)	21.966(3)	Parameters	143
c (Å)	21.966(3)	Restraints	1
α (°)	90.00	R_{int}	0.1061
β (°)	90.00	*R*1 [I > 2σ(I)]	0.0332
γ (°)	90.00	*wR*2 [I > 2σ(I)]	0.0837
V ($Å^3$)	10599(2)	*R*1 (all data)	0.0381
Z	4	*wR*2 (all data)	0.0856
T (*K*)	110(2)	GOF on F^2	1.000
$d_{calcd.}$ (g/cm^3)	0.957	$\Delta\rho_{max}$/ $\Delta\rho_{min}$ [$e \cdot Å^3$]	0.317 / -0.214

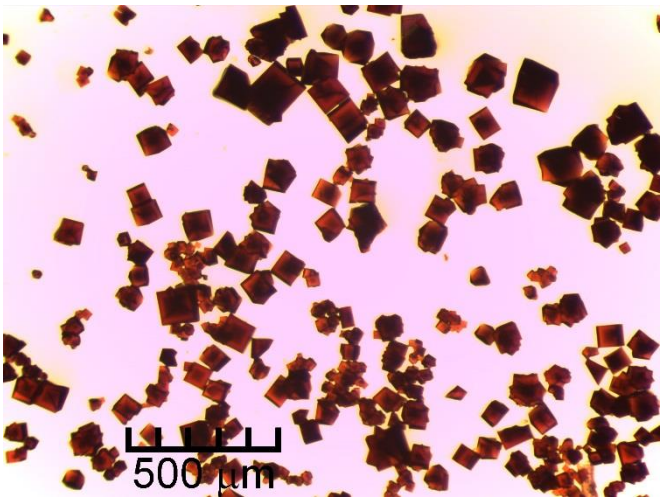

(a)

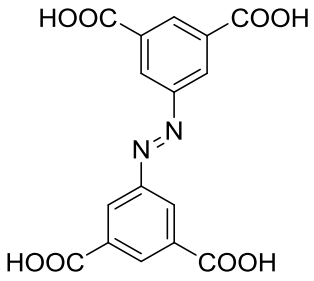

(b)

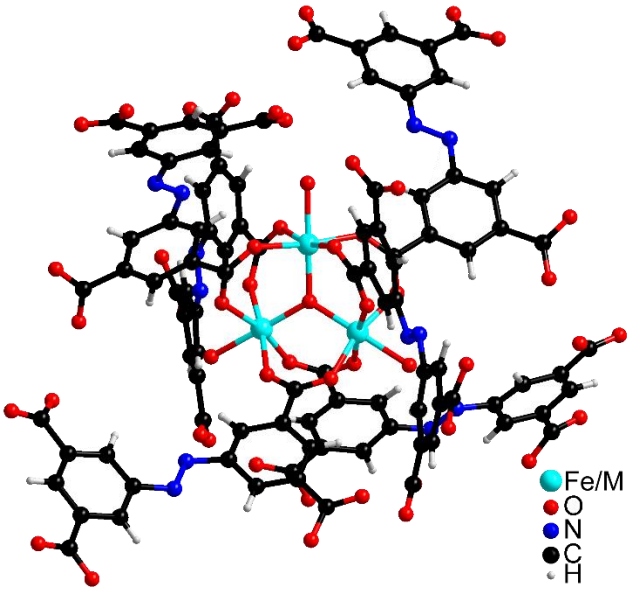

(c)

Figure 46. (a) Optical microscope image of solvated PCN-250'. (b) Ligand used in PCN-250'. (c) Fragment structure of PCN-250'.

Table 27. Crystal data and structure refinements for PCN-250'. (CCDC 975785)

Compound PCN-250'			
Formula	$Fe_4 Co_2 C_{48} H_{18} N_6 O_{32}$	μ(mm^{-1})	0.888
Fw	1531.94	*F*(000)	24384
Color/Shape	Red Triangle	θ_{max} [deg]	24.77
Crystal system	Cubic	Completeness	99.6%
Space group	$Ia\bar{3}$	Collected reflections	246510
a (Å)	44.043(17)	Unique reflections	12181
b (Å)	44.043(17)	Parameters	233
c (Å)	44.043(17)	Restraints	0
α (°)	90.00	R_{int}	0.2013
β (°)	90.00	*R*1 [I > 2σ(I)]	0.1827
γ (°)	90.00	*wR*2 [I > 2σ(I)]	0.3782
V ($Å^3$)	85433(56)	*R*1 (all data)	0.2463
Z	32	*wR*2 (all data)	0.4110
T (*K*)	110(2)	GOF on F^2	1.080
$d_{calcd.}$ (g/cm^3)	0.953	$\Delta\rho_{max}$/ $\Delta\rho_{min}$ [$e \cdot Å^3$]	1.933 / -1.185

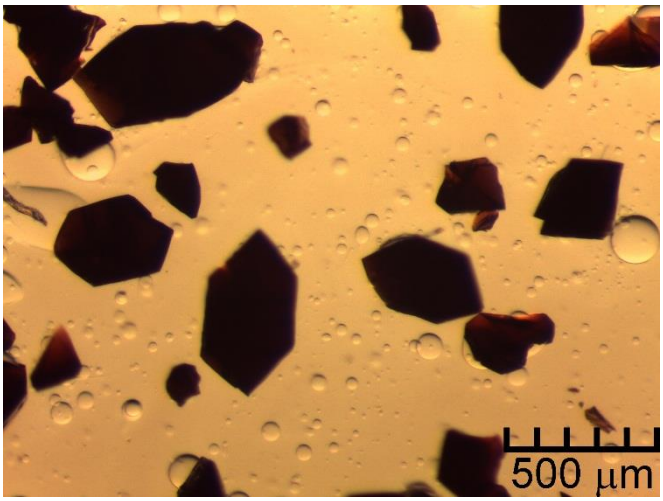

(a)

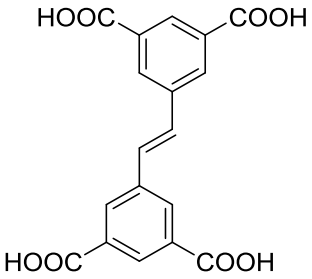

(b)

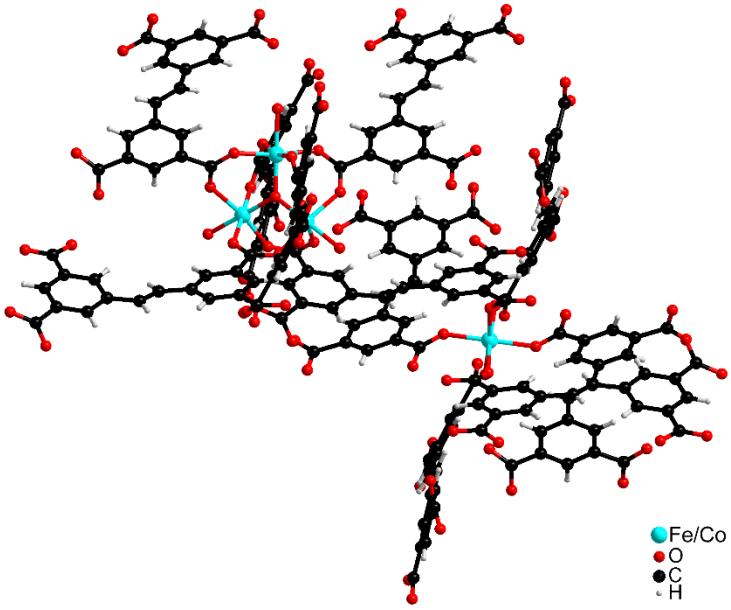

(c)

Figure 47. (a)Optical microscope image of solvated PCN-252. (b) Ligand used in PCN-252. (c) Fragment structure of PCN-252.

Table 28. Crystal data and structure refinements for PCN-252. (CCDC 975786)

Compound PCN-252			
Formula	Fe_7 Co_3 C_{108} H_{51} O_{60}	μ(mm^{-1})	0.834
Fw	2876.23	*F*(000)	8652
Color/Shape	Brown Hexagon	θ_{max} [deg]	26.40
Crystal system	Hexagonal	Completeness	99.9%
Space group	$R\bar{3}c$	Collected reflections	100751
a (Å)	32.839(8)	Unique reflections	6506
b (Å)	32.839(8)	Parameters	262
c (Å)	30.571(7)	Restraints	0
α (°)	90.00	R_{int}	0.0539
β (°)	90.00	*R*1 [I > 2σ(I)]	0.0580
γ (°)	120.00	*wR*2 [I > 2σ(I)]	0.1410
V ($Å^3$)	28551(12)	*R*1 (all data)	0.0675
Z	6	*wR*2 (all data)	0.1454
T (*K*)	110(2)	GOF on F^2	1.007
$d_{calcd.}$ (g/cm^3)	1.004	$\Delta\rho_{max}$/ $\Delta\rho_{min}$ [$e \cdot Å^3$]	2.364 / -1.752

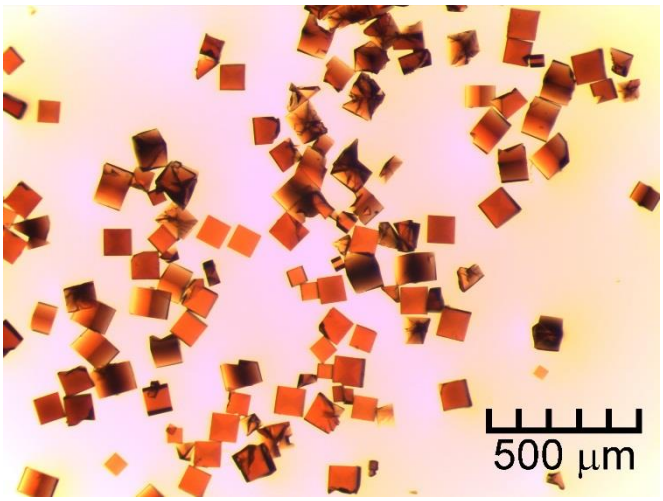

(a)

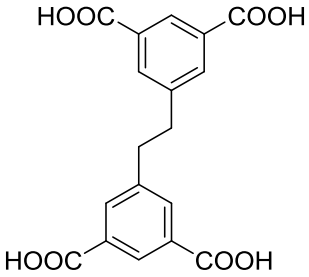

(b)

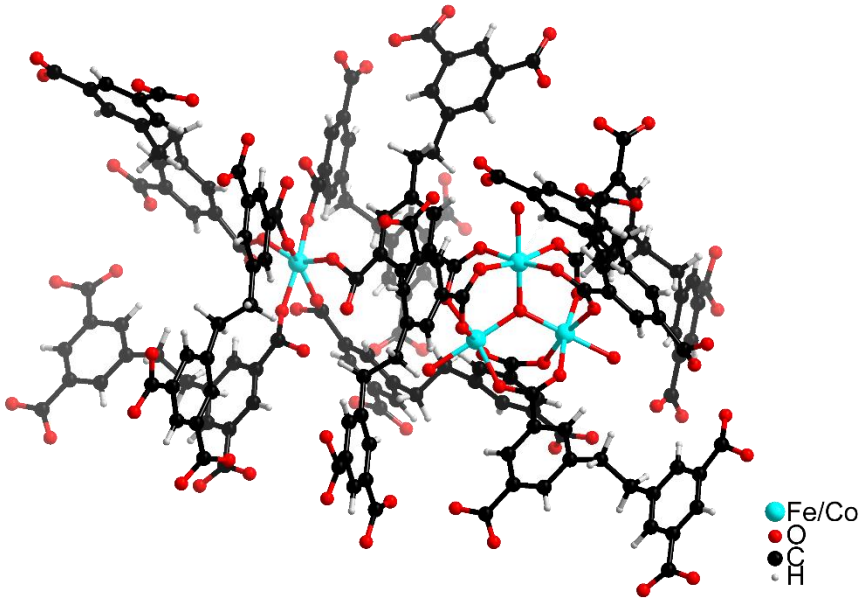

(c)

Figure 48. (a)Optical microscope image of solvated PCN-253. (b) Ligand used in PCN-253. (c) Fragment structure of PCN-253.

Table 29. Crystal data and structure refinements for PCN-253. (CCDC 975787)

Compound PCN-253			
Formula	Fe_7 Co_3 C_{108} H_{63} O_{60}	μ(mm^{-1})	0.813
Fw	2888.32	*F*(000)	8724
Color/Shape	Orange Cube	θ_{max} [deg]	24.65
Crystal system	Hexagonal	Completeness	99.1%
Space group	$R\bar{3}c$	Collected reflections	63421
a (Å)	32.00(6)	Unique reflections	5474
b (Å)	32.00(6)	Parameters	272
c (Å)	33.04(6)	Restraints	60
α ( )	90.00	R_{int}	0.2034
β ( )	90.00	*R*1 [I > 2σ(I)]	0.0690
γ ( )	120.00	*wR*2 [I > 2σ(I)]	0.1684
V ($Å^3$)	29303(89)	*R*1 (all data)	0.1511
Z	6	*wR*2 (all data)	0.1896
T (*K*)	110(2)	GOF on F^2	1.008
$d_{calcd.}$ (g/cm^3)	0.982	$\Delta\rho_{max}$/ $\Delta\rho_{min}$ [$e \cdot Å^3$]	0.710 / -0.543

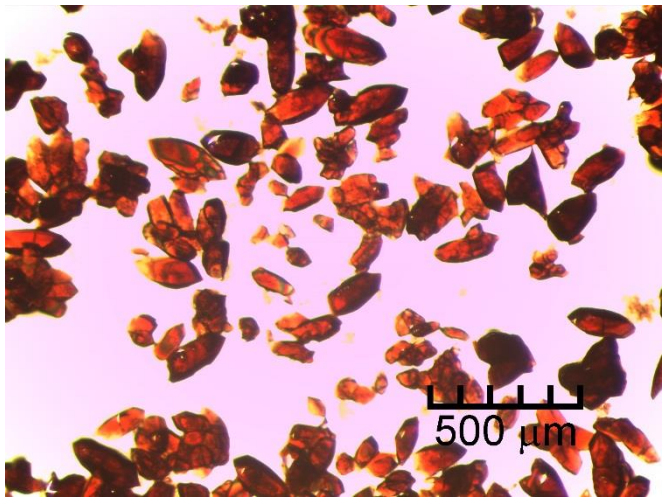

(a)

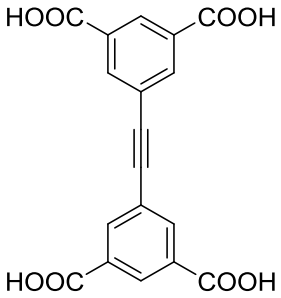

(b)

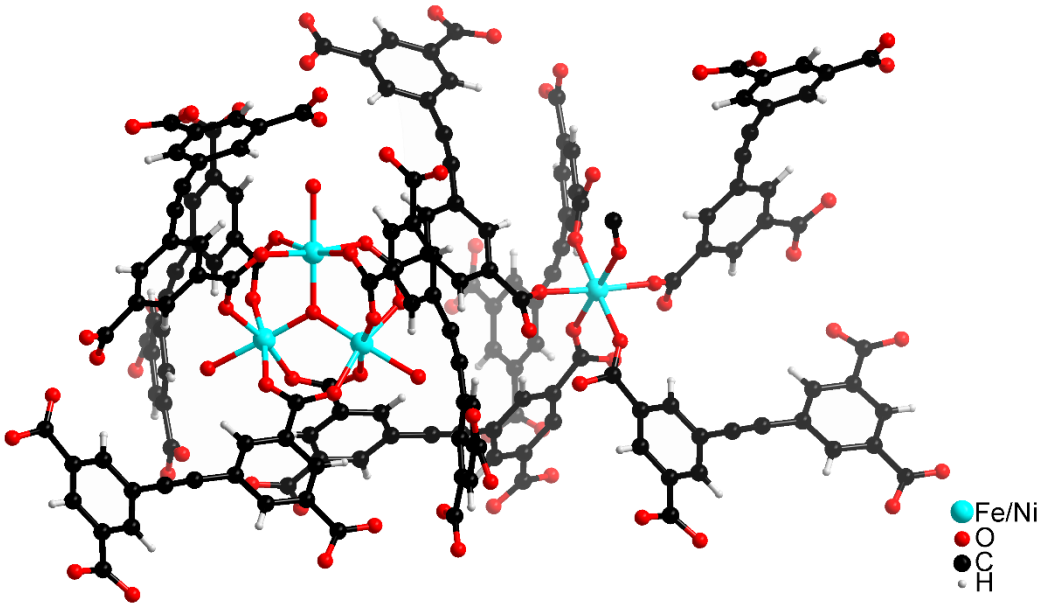

(c)

Figure 49. (a)Optical microscope image of solvated PCN-254. (b) Ligand used in PCN-254. (c) Fragment structure of PCN-254.

Table 30. Crystal data and structure refinements for PCN-254. (CCDC 975788)

Compound PCN-254			
Formula	Fe_7 Ni_3 C_{108} H_{39} O_{60}	μ(mm^{-1})	0.820
Fw	2863.47	*F*(000)	8598
Color/Shape	Red Bulk	θ_{max} [deg]	24.43
Crystal system	Hexagonal	Completeness	99.8%
Space group	$R\bar{3}c$	Collected reflections	67399
a (Å)	32.356(7)	Unique reflections	5557
b (Å)	32.356(7)	Parameters	268
c (Å)	33.363(7)	Restraints	0
α (°)	90.00	R_{int}	0.1530
β (°)	90.00	*R*1 [I > 2σ(I)]	0.0621
γ (°)	120.00	*wR*2 [I > 2σ(I)]	0.1559
V ($Å^3$)	30248(11)	*R*1 (all data)	0.1000
Z	6	*wR*2 (all data)	0.1674
T (*K*)	110(2)	GOF on F^2	1.001
$d_{calcd.}$ (g/cm^3)	0.943	$\Delta\rho_{max}$/ $\Delta\rho_{min}$ [$e \cdot Å^3$]	1.905 / -0.491

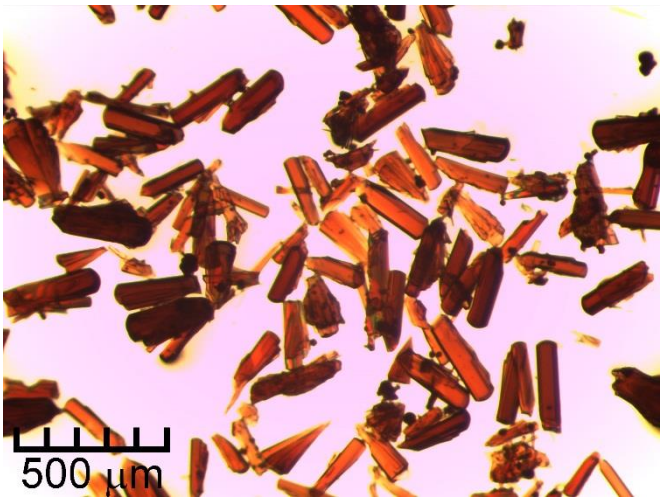

(a)

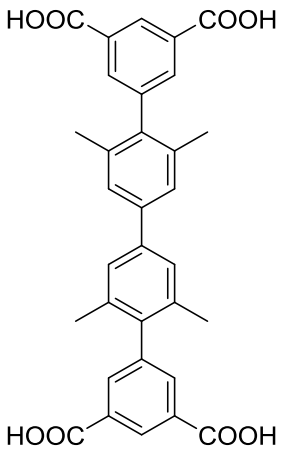

(b)

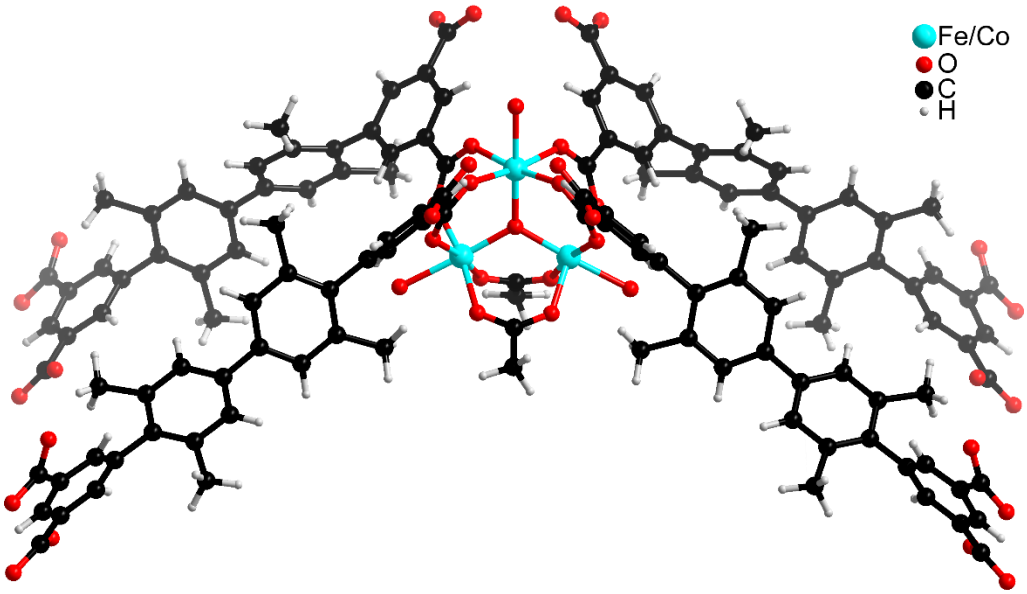

(c)

Figure 50. (a)Optical microscope image of solvated PCN-255. (b) Ligand used in PCN-255. (c) Fragment structure of PCN-255.

Table 31. Crystal data and structure refinements for PCN-255. (CCDC 975789)

Compound PCN-255			
Formula	Fe_2 Co C_{36} H_{28} O_{16}	μ(mm^{-1})	0.748
Fw	887.21	*F*(000)	5412
Color/Shape	Orange Rod	θ_{max} [deg]	24.64
Crystal system	Hexagonal	Completeness	99.3%
Space group	*P*6 /*mcc*	Collected reflections	167141
a (Å)	25.898(12)	Unique reflections	5495
b (Å)	25.898(12)	Parameters	236
c (Å)	32.995(19)	Restraints	46
α ( )	90.00	R_{int}	0.2159
β ( )	90.00	*R*1 [I > 2σ(I)]	0.1010
γ ( )	120.00	*wR*2 [I > 2σ(I)]	0.1890
V ($Å^3$)	19165(17)	*R*1 (all data)	0.1795
Z	12	*wR*2 (all data)	0.2258
T (*K*)	110(2)	GOF on F^2	1.008
$d_{calcd.}$ (g/cm^3)	0.922	$\Delta\rho_{max}$/ $\Delta\rho_{min}$ [$e \cdot Å^3$]	1.503 / -0.769

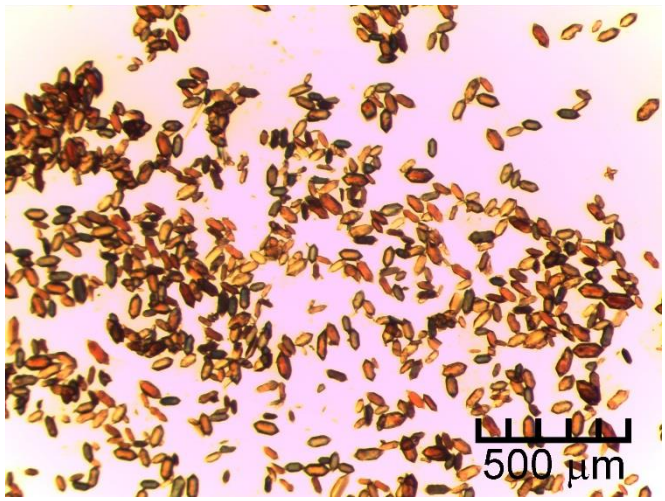

(a)

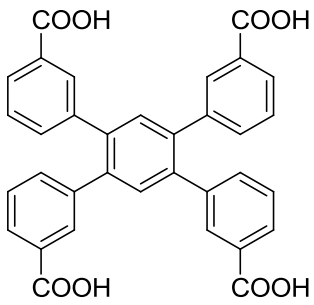

(b)

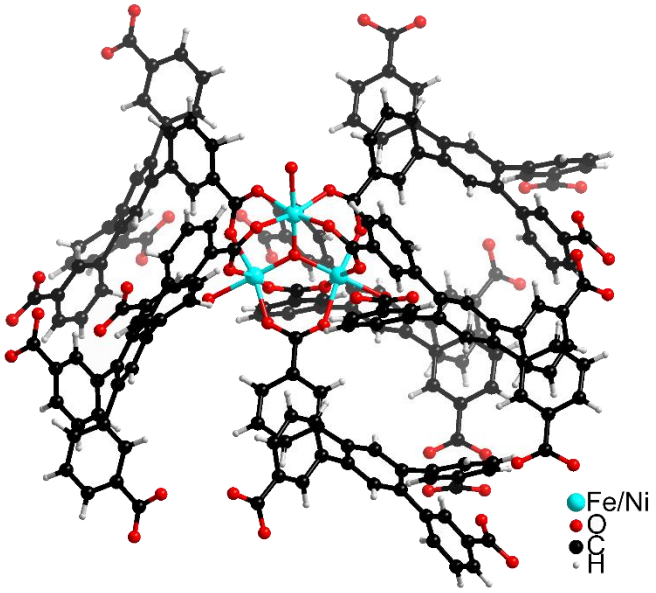

(c)

Figure 51. (a) Optical microscope image of solvated PCN-256. (b) Ligand used in PCN-256. (c) Fragment structure of PCN-256.

Table 32. Crystal data and structure refinements for PCN-256. (CCDC 975790)

Compound PCN-256			
Formula	$Fe_6C_{102}H_{54}O_{32}$	μ(mm^{-1})	0.569
Fw	2126.55	*F*(000)	2156
Color/Shape	Orange Hexagon	θ_{max} [deg]	24.58
Crystal system	Orthorhombic	Completeness	99.6%
Space group	*Cmma*	Collected reflections	36653
a (Å)	15.290(18)	Unique reflections	3654
b (Å)	24.48(3)	Parameters	169
c (Å)	21.79(3)	Restraints	18
α (°)	90.00	R_{int}	0.1400
β (°)	90.00	*R*1 [I > 2σ(I)]	0.0862
γ (°)	90.00	*wR*2 [I > 2σ(I)]	0.1925
V ($Å^3$)	8156(17)	*R*1 (all data)	0.1606
Z	2	*wR*2 (all data)	0.2139
T (*K*)	110(2)	GOF on F^2	1.002
$d_{calcd.}$ (g/cm^3)	0.866	$\Delta\rho_{max}$/ $\Delta\rho_{min}$ [$e\cdot Å^3$]	0.550 / -0.446

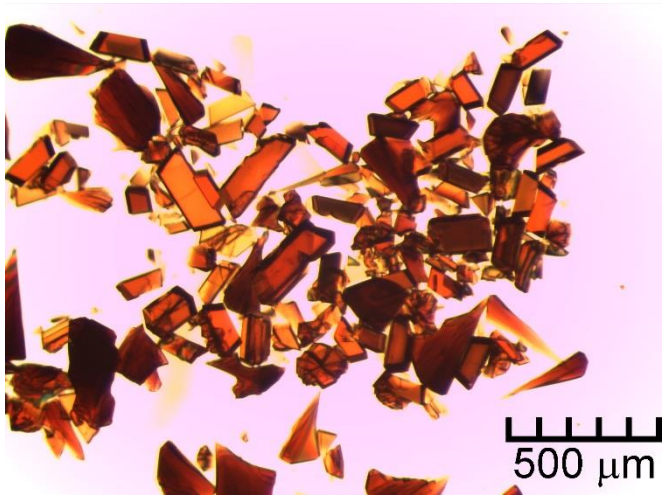

(a)

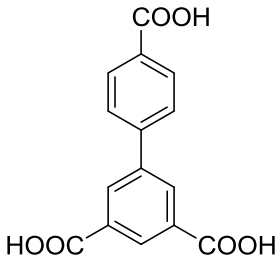

(b)

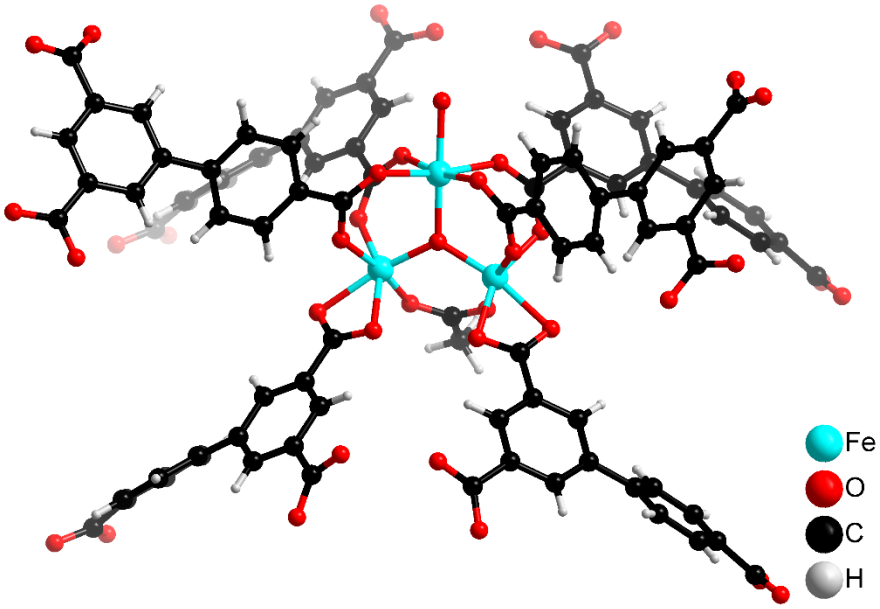

(c)

Figure 52. (a) Optical microscope image of solvated PCN-257. (b) Ligand used in PCN-257. (c) Fragment structure of PCN-257.

Table 33. Crystal data and structure refinements for PCN-257. (CCDC 975791)

Compound PCN-257		Absolute structure parameter: 0.036(14)	
Formula	$Fe_3 C_{32} H_{17} O_{16}$	$\mu(mm^{-1})$	0.635
Fw	825.01	*F*(000)	830
Color/Shape	Red Column	θ_{max} [deg]	24.81
Crystal system	Orthorhombic	Completeness	99.7%
Space group	$Pmn2_1$	Collected reflections	33286
a (Å)	23.570(3)	Unique reflections	6342
b (Å)	9.8918(11)	Parameters	240
c (Å)	15.3668(18)	Restraints	31
α (°)	90.00	R_{int}	0.0636
β (°)	90.00	*R*1 [I > 2σ(I)]	0.0356
γ (°)	90.00	*wR*2 [I > 2σ(I)]	0.0715
V ($Å^3$)	3582.8(7)	*R*1 (all data)	0.0422
Z	2	*wR*2 (all data)	0.0729
T (*K*)	110(2)	GOF on F^2	1.003
$d_{calcd.}$ (g/cm^3)	0.765	$\Delta\rho_{max}/ \Delta\rho_{min}$ [$e \cdot Å^3$]	0.350 / -0.374

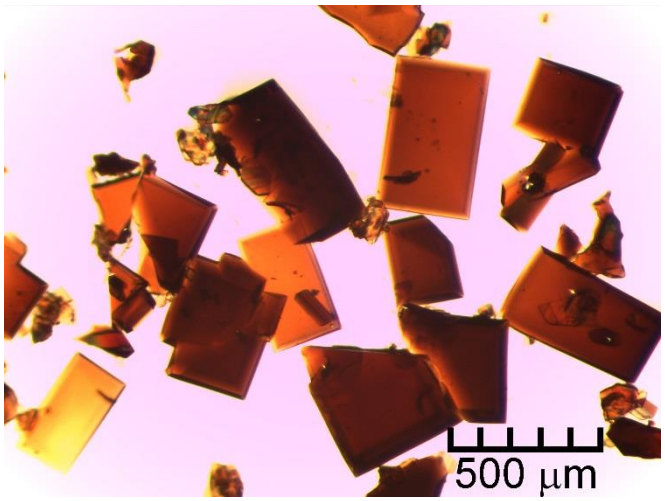

(a)

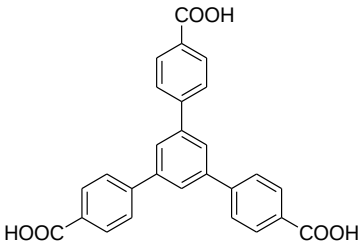

(b)

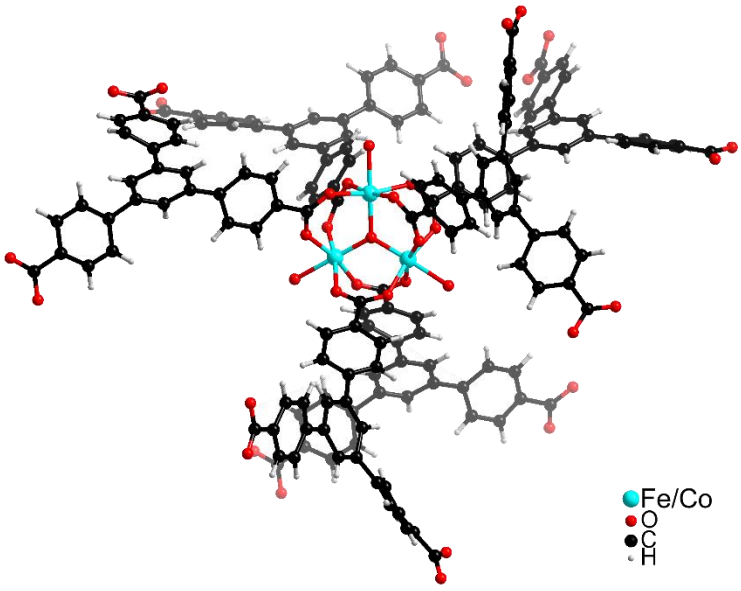

(c)

Figure 53. (a) Optical microscope image of solvated PCN-260. (b) Ligand used in PCN-260. (c) Fragment structure of PCN-260.

Table 34. Crystal data and structure refinements for PCN-260. (CCDC 975820)

Compound PCN-260		Absolute structure parameter : 0.453(11)	
Formula	Fe_2 Co C_{54} H_{30} O_{16}	μ(mm^{-1})	0.297
Fw	1105.41	*F*(000)	4488
Color/Shape	Orange Rectangle	θ_{max} [deg]	24.78
Crystal system	Orthorhombic	Completeness	99.8%
Space group	*Pca*2_1	Collected reflections	303240
a (Å)	36.155(4)	Unique reflections	56026
b (Å)	18.566(2)	Parameters	830
c (Å)	48.725(6)	Restraints	1
α ( )	90.00	R_{int}	0.0733
β ( )	90.00	*R*1 [I > 2σ(I)]	0.0630
γ ( )	90.00	*wR*2 [I > 2σ(I)]	0.1264
V ($Å^3$)	32707(6)	*R*1 (all data)	0.0914
Z	8	*wR*2 (all data)	0.1339
T (*K*)	110(2)	GOF on F^2	1.000
$d_{calcd.}$ (g/cm^3)	0.449	$\Delta\rho_{max}$/ $\Delta\rho_{min}$ [$e \cdot Å^3$]	0.793 / -0.688

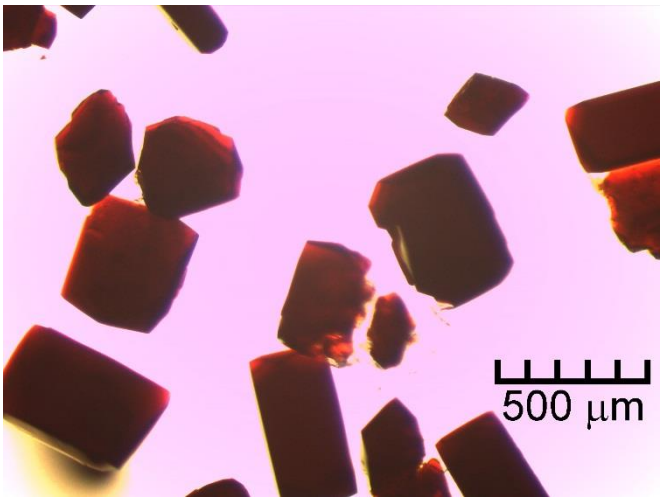

(a)

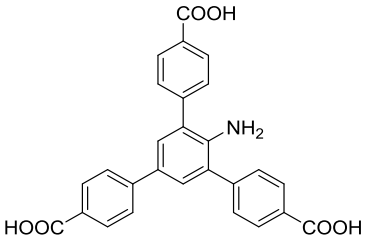

(b)

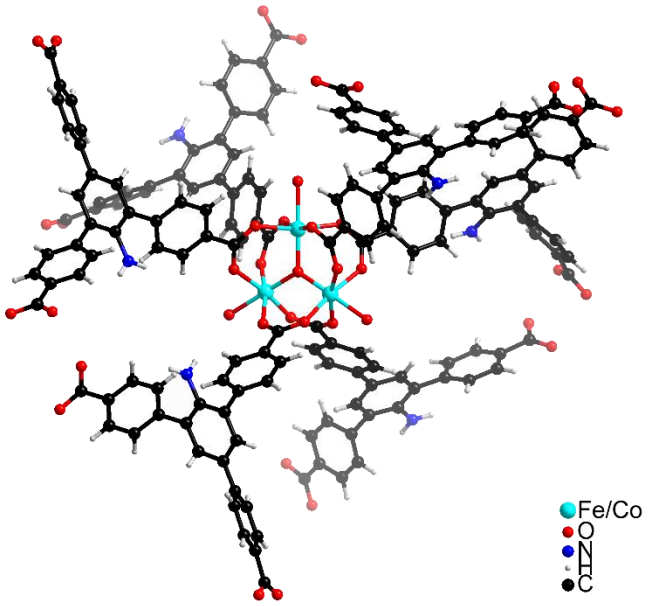

(c)

Figure 54. (a) Optical microscope image of solvated PCN-261. (b) Ligand used in PCN-261. (c) Fragment structure of PCN-261.

Table 35. Crystal data and structure refinements for PCN-261. (CCDC 975821)

Compound PCN-261			
Formula	Fe_2 Co C_{54} H_{32} N_2 O_{16}	μ(mm^{-1})	0.271
Fw	1135.45	*F*(000)	2308
Color/Shape	Red Rectangle	θ_{max} [deg]	26.00
Crystal system	Monoclinic	Completeness	99.8%
Space group	$P2_1/c$	Collected reflections	141021
a (Å)	27.005(4)	Unique reflections	35362
b (Å)	18.564(3)	Parameters	553
c (Å)	36.389(5)	Restraints	0
α ( )	90.00	R_{int}	0.0951
β ( )	98.848(2)	*R*1 [I > 2σ(I)]	0.0583
γ ( )	90.00	*wR*2 [I > 2σ(I)]	0.1172
V ($Å^3$)	18025(5)	*R*1 (all data)	0.1533
Z	4	*wR*2 (all data)	0.1259
T (*K*)	110(2)	GOF on F^2	1.007
$d_{calcd.}$ (g/cm^3)	0.418	$\Delta\rho_{max}$/ $\Delta\rho_{min}$ [$e \cdot Å^3$]	0.494 / -0.421

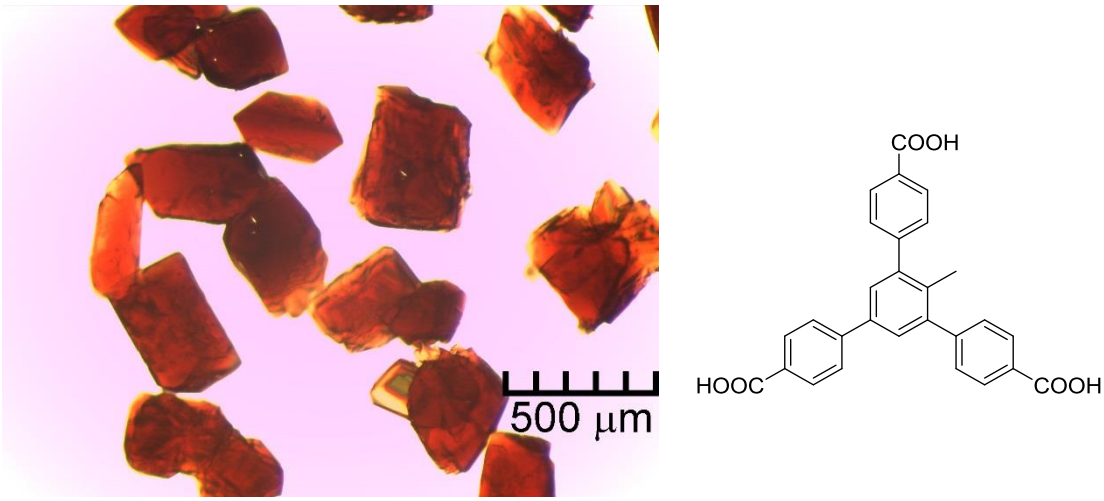

(a) (b)

Figure 55. (a) Optical microscope image of solvated PCN-261(Me). (b) Ligand used in PCN-261(Me).

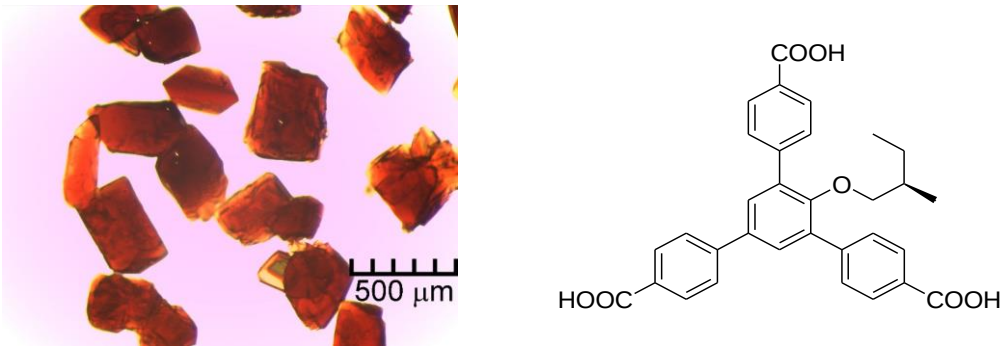

(a) (b)

Figure 56 . (a) Optical microscope image of solvated PCN-261(chiral). (b) Ligand used in PCN-261(chiral).

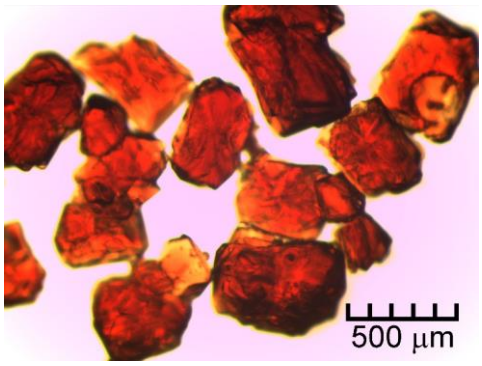

(a)

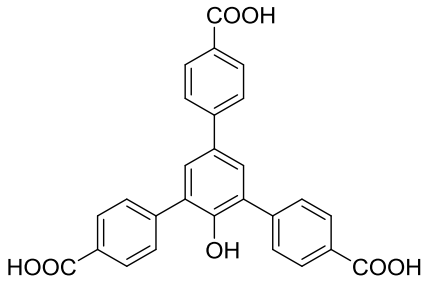

(b)

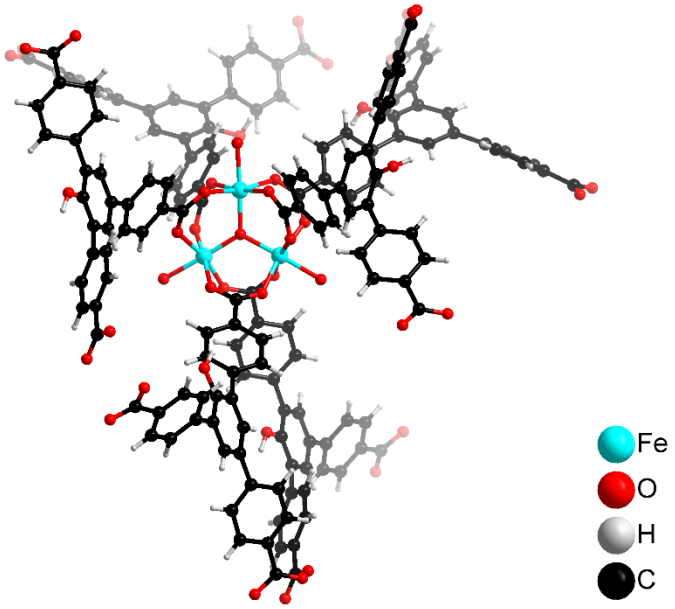

(c)

Figure 57. (a) Optical microscope image of solvated PCN-262. (b) Ligand used in PCN-262. (c) Fragment structure of PCN-262.

.

Table 36. Crystal data and structure refinements for PCN-262. (CCDC 975822)

Compound PCN-262			
Formula	$Fe_3 C_{54} H_{30} O_{18}$	$\mu(mm^{-1})$	0.292
Fw	1134.33	*F*(000)	2304
Color/Shape	Orange Bulk	θ_{max} [deg]	24.52
Crystal system	Monoclinic,	Completeness	99.5%
Space group	$P2_1/c$	Collected reflections	143677
a (Å)	24.688(4)	Unique reflections	26567
b (Å)	18.375(3)	Parameters	438
c (Å)	35.257(6)	Restraints	144
α ( )	90.00	R_{int}	0.0697
β ( )	90.345(2)	*R*1 [I > 2σ(I)]	0.0632
γ ( )	90.00	*wR*2 [I > 2σ(I)]	0.1321
V ($Å^3$)	15994(4)	*R*1 (all data)	0.1117
Z	4	*wR*2 (all data)	0.1399
T (*K*)	110(2)	GOF on F^2	1.000
$d_{calcd.}$ (g/cm^3)	0.471	$\Delta\rho_{max}/\Delta\rho_{min}$ [$e \cdot Å^3$]	0.663 / -0.341

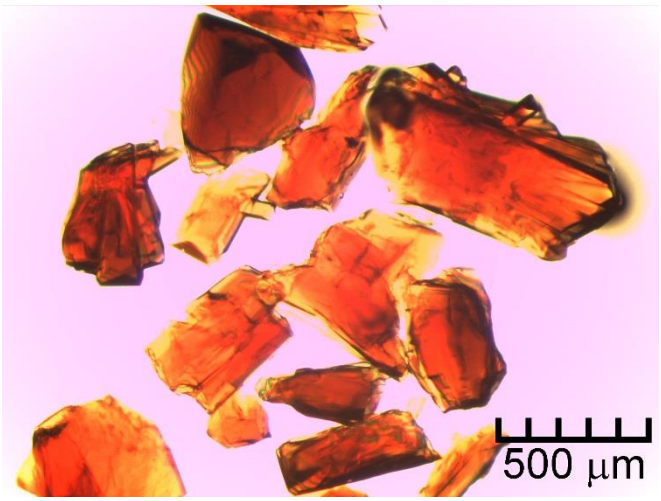

(a)

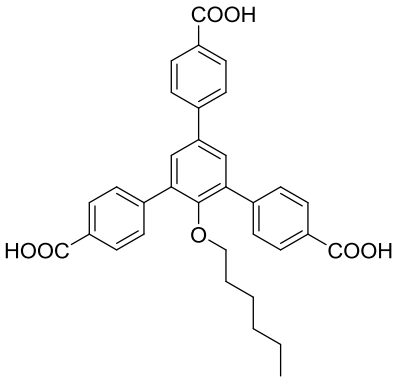

(b)

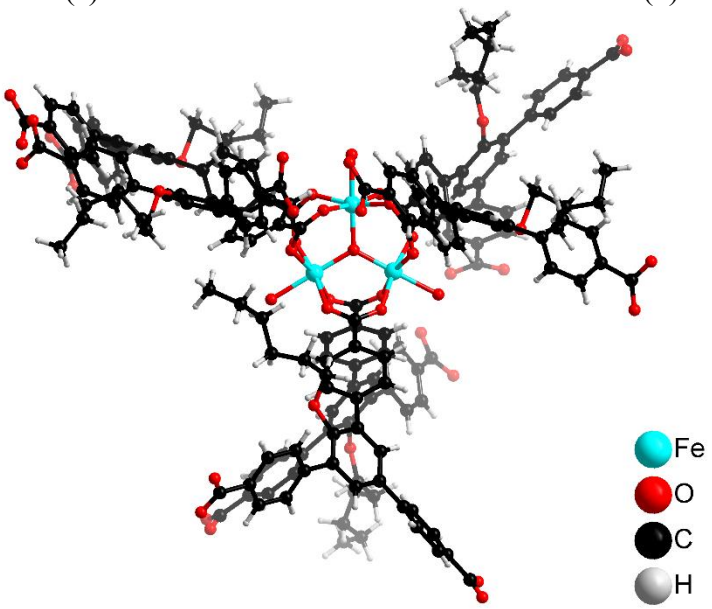

(c)

Figure 58. (a) Optical microscope image of solvated PCN-263. (b) Ligand used in PCN-263. (c) Fragment structure of PCN-263.

Table 37. Crystal data and structure refinements for PCN-263. (CCDC 975823)

Compound PCN-263			
Formula	$Fe_3 C_{66} H_{54} O_{18}$	$\mu(mm^{-1})$	0.287
Fw	1302.64	*F*(000)	2688
Color/Shape	Orange Bulk	θ_{max} [deg]	26.00
Crystal system	Monoclinic	Completeness	99.9%
Space group	$P2_1/c$	Collected reflections	130129
a (Å)	25.085(3)	Unique reflections	32434
b (Å)	18.549(3)	Parameters	628
c (Å)	35.494(5)	Restraints	19
α (°)	90.00	R_{int}	0.1060
β (°)	91.607(2)	*R*1 [I > 2σ(I)]	0.0575
γ (°)	90.00	*wR*2 [I > 2σ(I)]	0.1214
V ($Å^3$)	16509(4)	*R*1 (all data)	0.1546
Z	4	*wR*2 (all data)	0.1253
T (*K*)	110(2)	GOF on F^2	0.996
$d_{calcd.}$ (g/cm^3)	0.524	$\Delta\rho_{max}$/ $\Delta\rho_{min}$ [$e \cdot Å^{-3}$]	0.429 / -0.327

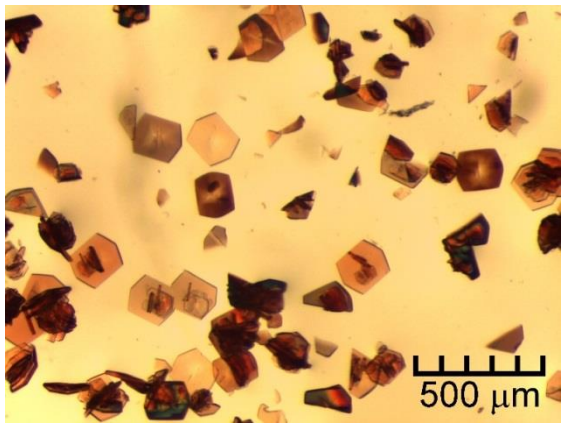

(a)

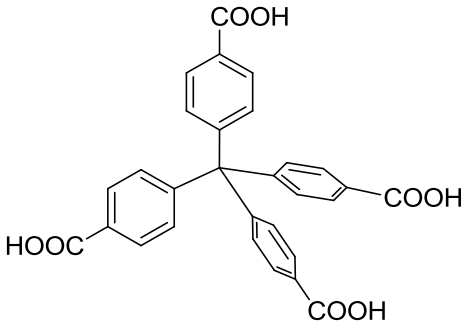

(b)

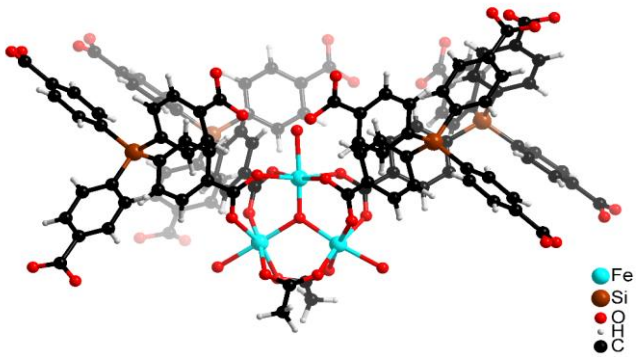

(c)

Figure 59. (a) Optical microscope image of solvated PCN-264. (b) Ligand used in PCN-264. (c) Fragment structure of PCN-264.

Table 38. Crystal data and structure refinements for PCN-264. (CCDC 975824)

Compound PCN-264			
Formula	$Fe_6\ C_{64}\ H_{46}\ O_{32}\ Si_2$	$\mu(mm^{-1})$	0.719
Fw	1718.29	*F*(000)	3480
Color/Shape	Peach Plate	θ_{max} [deg]	23.06
Crystal system	Monoclinic	Completeness	98.6%
Space group	$P2_1/c$	Collected reflections	56104
a (Å)	24.24(2)	Unique reflections	13876
b (Å)	23.09(2)	Parameters	475
c (Å)	23.97(2)	Restraints	38
α (°)	90	R_{int}	0.1466
β (°)	104.274(8)	*R*1 [I > 2σ(I)]	0.1503
γ (°)	90	*wR*2 [I > 2σ(I)]	0.3554
V ($Å^3$)	13002(19)	*R*1 (all data)	0.2459
Z	4	*wR*2 (all data)	0.3790
T (*K*)	150(2)	GOF on F^2	1.003
$d_{calcd.}$ (g/cm^3)	0.878	$\Delta\rho_{max}/\ \Delta\rho_{min}$ [$e\cdot Å^3$]	1.459 / -0.758

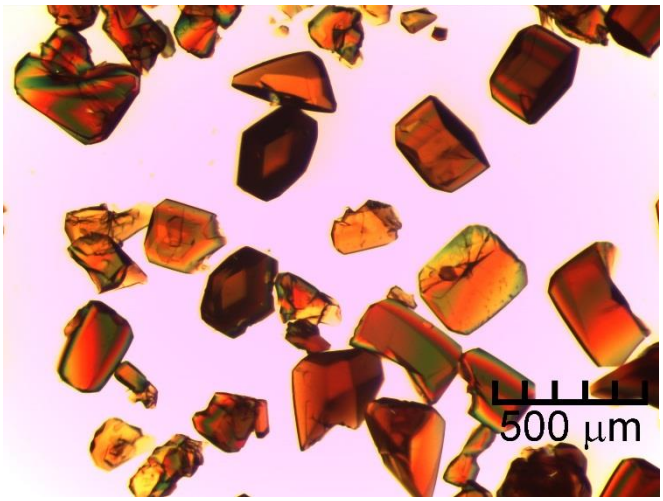

(a)

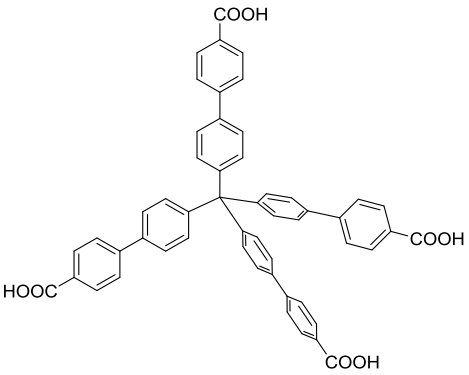

(b)

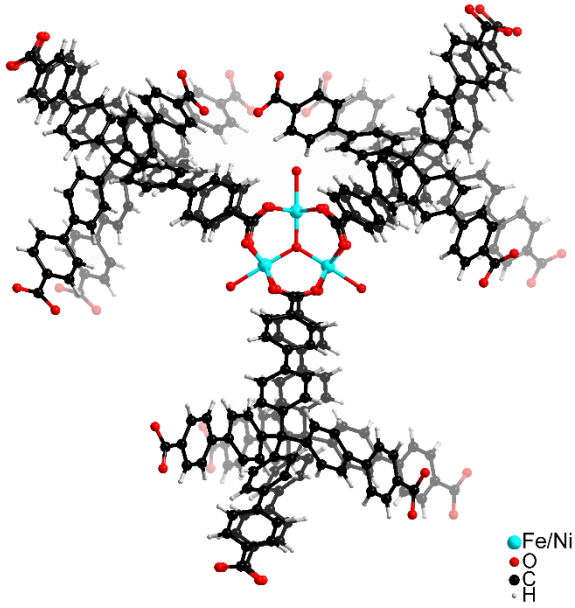

(c)

Figure 60. (a) Optical microscope image of solvated PCN-265. (b) Ligand used in PCN-265. (c) Fragment structure of PCN-265.

Table 39. Crystal data and structure refinements for PCN-265. (CCDC 975825)

Compound PCN-265			
Formula	Fe_2 Ni C_{106} H_{64} O_{20}	μ(mm^{-1})	0.362
Fw	1827.98	*F*(000)	3760
Color/Shape	Orange Rectangle	θ_{max} [deg]	26.51
Crystal system	Orthorhombic	Completeness	99.6%
Space group	*Pbcm*	Collected reflections	145895
a (Å)	11.519(4)	Unique reflections	15639
b (Å)	33.385(10)	Parameters	512
c (Å)	38.702(12)	Restraints	0
α ( )	90.00	R_{int}	0.0907
β ( )	90.00	*R*1 [I > 2σ(I)]	0.0726
γ ( )	90.00	*wR*2 [I > 2σ(I)]	0.2058
V ($Å^3$)	14883(8)	*R*1 (all data)	0.1304
Z	4	*wR*2 (all data)	0.2265
T (*K*)	110(2)	GOF on F^2	1.006
$d_{calcd.}$ (g/cm^3)	0.816	$\Delta\rho_{max}$/ $\Delta\rho_{min}$ [$e \cdot Å^3$]	1.182 / -0.503

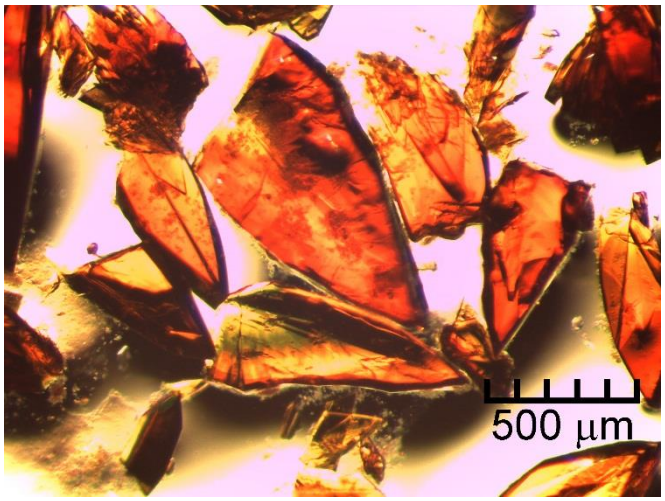

(a)

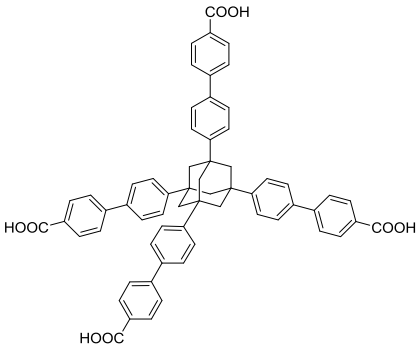

(b)

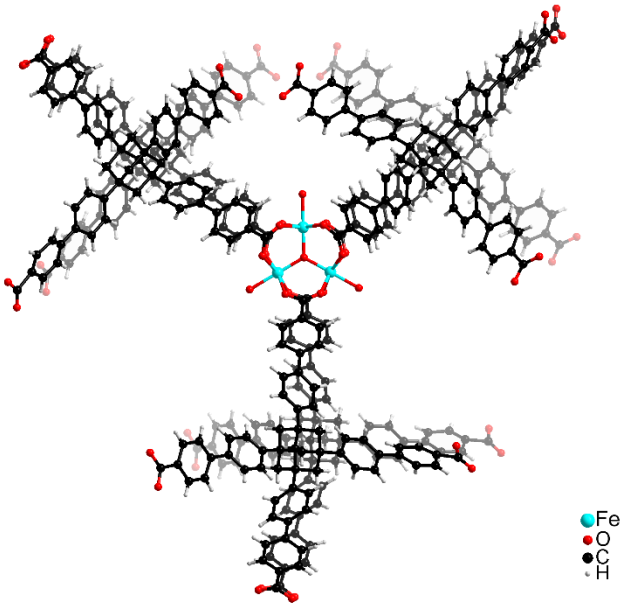

(c)

Figure 61. (a) Optical microscope image of solvated PCN-266. (b) Ligand used in PCN-266. (c) Fragment structure of PCN-266.

Table 40. Crystal data and structure refinements for PCN-266. (CCDC 975826)

Compound PCN-266			
Formula	$Fe_3 C_{124} H_{88} O_{20}$	$\mu(mm^{-1})$	0.213
Fw	2065.49	*F*(000)	4280
Color/Shape	Red Bulk	θ_{max} [deg]	24.21
Crystal system	Orthorhombic	Completeness	99.3%
Space group	*Pbcm*	Collected reflections	207656
a (Å)	14.9208(14)	Unique reflections	19245
b (Å)	41.280(4)	Parameters	565
c (Å)	38.398(3)	Restraints	1
α (°)	90.00	R_{int}	0.0772
β (°)	90.00	*R*1 [I > 2σ(I)]	0.0949
γ (°)	90.00	*wR*2 [I > 2σ(I)]	0.2025
V ($Å^3$)	23651(4)	*R*1 (all data)	0.1562
Z	4	*wR*2 (all data)	0.2255
T (*K*)	296(2)	GOF on F^2	1.002
$d_{calcd.}$ (g/cm^3)	0.580	$\Delta\rho_{max}/ \Delta\rho_{min}$ [$e \cdot Å^3$]	0.906 / -0.472

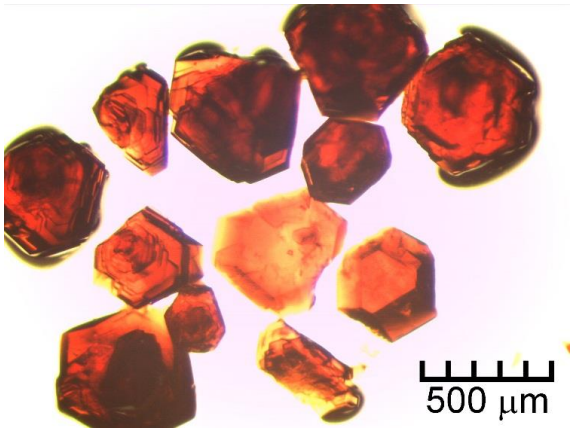

(a)

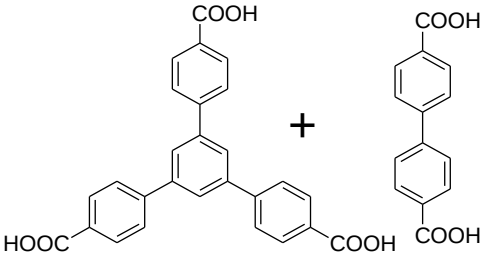

(b)

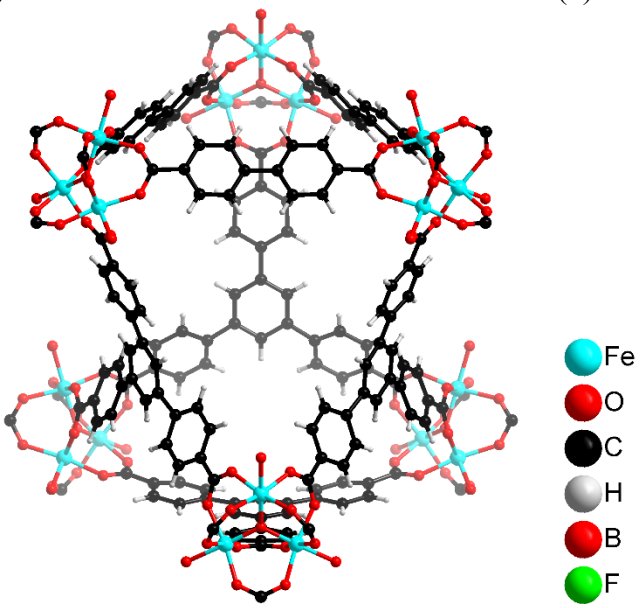

(c)

Figure 62. (a) Optical microscope image of solvated PCN-280. (b) Ligand used in PCN-280. (c) Fragment structure of PCN-280.

Table 41. Crystal data and structure refinements for PCN-280. (CCDC 975827)

Compound PCN-280		Absolute structure parameter: 0.11(2)	
Formula	$Fe_9\ C_{150}\ H_{84}\ O_{48}$	$\mu(mm^{-1})$	0.484
Fw	3156.82	*F*(000)	4806
Color/Shape	Red Truncated Triangle	θ_{max} [deg]	24.49
Crystal system	Hexagonal	Completeness	99.9%
Space group	*R*3*m*	Collected reflections	46734
a (Å)	33.020(16)	Unique reflections	8359
b (Å)	33.020(16)	Parameters	214
c (Å)	22.796(11)	Restraints	107
α ( )	90.00	R_{int}	0.1077
β ( )	90.00	*R*1 [I > 2σ(I)]	0.0552
γ ( )	120.00	*wR*2 [I > 2σ(I)]	0.1327
V ($Å^3$)	21525(18)	*R*1 (all data)	0.0856
Z	3	*wR*2 (all data)	0.1414
T (*K*)	110 (2)	GOF on F^2	1.000
$d_{calcd.}$ (g/cm^3)	0.731	$\Delta\rho_{max}/\ \Delta\rho_{min}$ [$e \cdot Å^3$]	0.560 / -0.394

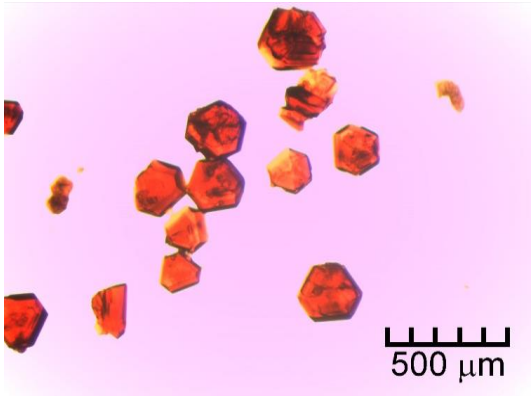

(a)

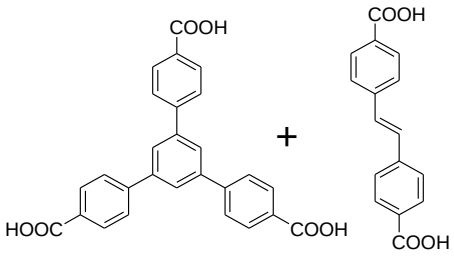

(b)

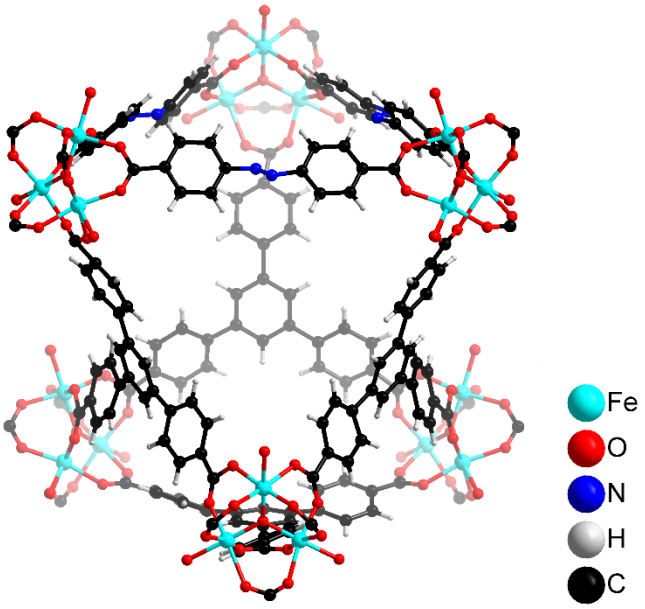

(c)

Figure 63. (a) Optical microscope image of solvated PCN-285. (b) Ligand used in PCN-285. (c) Fragment structure of PCN-285.

Table 42. Crystal data and structure refinements for PCN-285. (CCDC 975828)

Compound PCN-285		Absolute structure parameter: 0.267(16)	
Formula	Fe_9 C_{150} H_{84} N_6 O_{48}	$\mu(mm^{-1})$	0.225
Fw	3240.88	*F*(000)	4932
Color/Shape	Red Truncated Triangle	θ_{max} [deg]	24.34
Crystal system	Hexagonal	Completeness	98.4%
Space group*	*R*3	Collected reflections	132298
a (Å)	34.663(15)	Unique reflections	32920
b (Å)	34.663(15)	Parameters	329
c (Å)	44.712(19)	Restraints	133
α (°)	90.00	R_{int}	0.1806
β (°)	90.00	*R*1 [I > 2σ(I)]	0.0733
γ (°)	120.00	*wR*2 [I > 2σ(I)]	0.1472
V ($Å^3$)	46526(34)	*R*1 (all data)	0.1719
Z	3	*wR*2 (all data)	0.1813
T (*K*)	110 (2)	GOF on F^2	0.661
$d_{calcd.}$ (g/cm^3)	0.347	$\Delta\rho_{max}$/ $\Delta\rho_{min}$ [$e \cdot Å^3$]	0.349 / -0.200

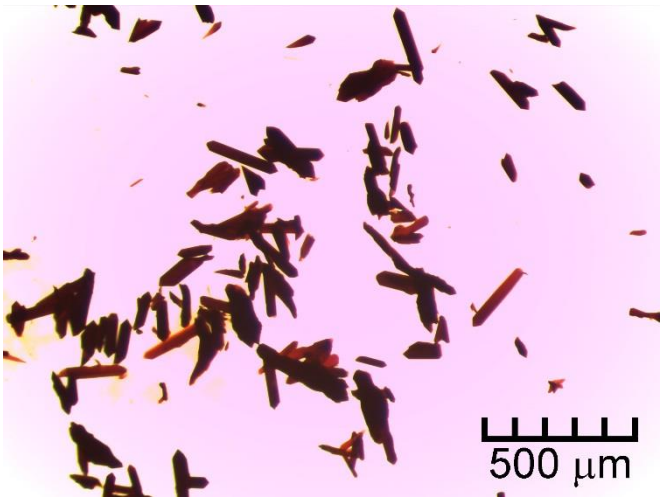

(a)

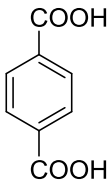

(b)

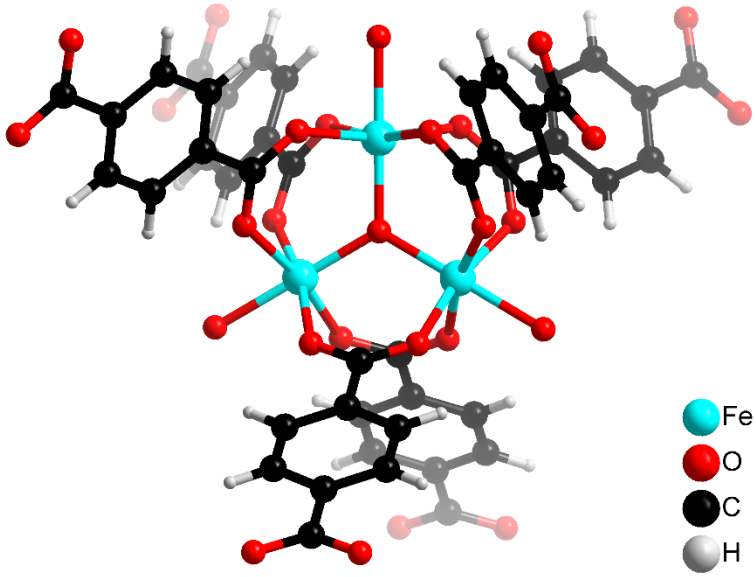

(c)

Figure 64. (a) Optical microscope image of solvated MIL-88. (b) Ligand used in MIL-88. (c) Fragment structure of MIL-88.

Table 43. Crystal data and structure refinements for MIL-88.

Compound MIL-88			
Formula	$Fe_3 C_{24} H_{12} O_{16}$	$\mu(mm^{-1})$	0.693
Fw	723.89	*F*(000)	724
Color/Shape	Red Rod	θ_{max} [deg]	25.01
Crystal system	Hexagonal	Completeness	99.9%
Space group	$P6_3/mmc$	Collected reflections	30162
a (Å)	14.8778(10)	Unique reflections	1123
b (Å)	14.8778(10)	Parameters	41
c (Å)	16.964(2)	Restraints	0
α ( )	90.00	R_{int}	0.0965
β ( )	90.00	*R*1 [I > 2σ(I)]	0.0540
γ ( )	120.00	*wR*2 [I > 2σ(I)]	0.1295
V ($Å^3$)	3251.9(5)	*R*1 (all data)	0.0754
Z	2	*wR*2 (all data)	0.1388
T (*K*)	110 (2)	GOF on F^2	1.001
$d_{calcd.}$ (g/cm^3)	0.739	$\Delta\rho_{max}/\Delta\rho_{min}$ [$e \cdot Å^3$]	0.413 / -0.334

Gas Adsorption Measurements Before sorption experiment, as-synthesized PCN-250(Fe_2Co) samples were washed with dry DMF for several times and immersed in DMF for 2 days to remove unreacted starting ligands, inorganic species and acetic acid. After that, DMF is decanted and washed with dry methanol for several times and immersed in methanol at 65^oC. This is repeated for 2 days to completely substitute the coordinating molecule. After that, methanol is decanted and sample is washed with dry CH_2Cl_2 for several times and then CH_2Cl_2 solvent exchange is conducted under well sealed vial at 60^oC for 3 days. After that, removed the solvent on the vacuum line and transport the samples in the glove box to prevent the re-adsorption of H_2O from the air. Then the sample was activated again by using the 'outgas' function of the adsorption instrument for 12 h at 190 ℃ prior to gas adsorption/desorption measurement.

For the stability test, samples from the same batch are treated with different aqueous solution for the listed period. After that, the activation process is repeated as the above procedure and N_2 adsorption at 77K is measured.

Simulation and Computation Methods Hypothetical metal-organic frameworks were enumerated based on the Fe_2Co secondary building unit (SBU) with trigonal prismatic coordination (i.e., six-connected). This SBU was combined separatelywith each linker from a set of 120 linear dicarboxylic acids from the eMolecules.com commercial database, which had been previously utilized in the assembly of MOF-5 analogues (i.e., structures exhibiting the pcu net, and based on a Zn4O SBU). The combination of linear linkers and the trigonal prismatic Fe2Co SBU yields the acs net, and as such these hypothetical materials are isostructural to MIL-88. In total, 105

structure models were produced; 15 linkers produced no valid structure due to collision between the building blocks. The structure models were not relaxed.

We model the energetic interactions of a gas (hydrogen or methane) molecule between the solid and another gas molecule with Lennard-Jones potentials. Both methane and hydrogen are modeled as uncharged, united atoms (i.e. a single sphere with a Lennard-Jones potential). The Lennard-Jones parameters for the solid atoms are taken from the Universal Force Field, for methane are taken from TraPPE, and for hydrogen are taken from Ref. (S9). Ref (S9) implicitly includes the partial charges of hydrogen by fitting the Lennard-Jones parameters to the virial coefficients obtained experimentally (. TraPPE parameters for methane reproduce its critical properties and vapor−liquid coexistence curve. Lorentz-Berthelot mixing rules yield the Lennard-Jones parameters for interactions between two atoms of different identities. This force field for methane and hydrogen is generally good for modeling adsorption in MOFs. We approximate the Lennard-Jones potential to be zero beyond a critical radius of 12.5 A. This allows us to apply periodic boundary conditions to mimic an infinite crystal. The crystal is considered rigid during our calculations. To predict the equilibrium adsorption isotherms for both hydrogen and methane, we performed Monte Carlo simulations of the grand canonical ensemble. The Peng-Robinson equation of state was used to relate the pressure in experiment to the fugacity (chemical potential). The simulated isotherms are the total adsorption (not excess).

4.3 Results and Discussion

Most chemically stable MOFs are constructed with hard Lewis acidic metal ions such as Fe^{3+}, Al^{3+}, and Zr^{4+} when carboxylate ligands (hard bases) are used. Due to the strong electrostatic interaction between the metal nodes and organic linkers, the frameworks are relatively resistant to the attack of H_2O and acidic or basic reactants. However, the stronger coordination bond is also more difficult to dissociate during the MOF growth process, which results in insufficient structure reorganization or defect reparation. As a result, highly crystalline stable MOFs are extremely difficult to synthesize under normal conditions.

The MOF crystal growth process is essentially ligand substitution on metal ions or clusters. Since most substitution reactions of octahedral complexes go through a dissociative mechanism, ligand substitution reactions(X: initial coordinating ligand, L: bridging ligand) on each individual inorganic building block during MOF growth can be modeled as the stepwise substitution on metal or metal clusters (M) (Scheme 3).

$$MX_6 \underset{k_{-1}}{\overset{k_1}{\rightleftharpoons}} MX_5 + X \quad (1)$$

$$MX_5 + L \underset{k_{-2}}{\overset{k_2}{\rightleftharpoons}} MX_5L$$

$$MX_5L \underset{k_{-3}}{\overset{k_3}{\rightleftharpoons}} MX_4L + X \quad (2)$$

$$MX_4L + L \underset{k_{-4}}{\overset{k_4}{\rightleftharpoons}} MX_4L_2$$

$$MX_4L_2 \underset{k_{-5}}{\overset{k_5}{\rightleftharpoons}} MX_3L_2 + X \quad (3)$$

...

Scheme 3. Stepwise substitution through a dissociative mechanism. M represents metal or metal cluster building block in MOFs, X represents the initial coordinating ligand and L represents the bridging ligand (organic linker).

The model in Scheme 3 illustrates how we can tune the synthesis conditions to promote the flux of ligands on and off a metal cluster and hence facilitate defect reparation and structure reorganization. Consider a metal cluster fully bound to only initial coordinating ligands. The rate of substitution for one of the initial coordinating ligands with a bridging ligand (r_{s1})

$$r_{s1} = k_2[\mathrm{MX_5}][\mathrm{L}]$$

At steady state

$$r_{s1} = \frac{k_2 k_1[\mathrm{MX_6}][\mathrm{L}]}{k_{-1}[\mathrm{X}]+k_2[\mathrm{L}]}$$

Thus, **X** behaves as a competitor to L, and we can slow the rate of bridging ligand attachment by increasing the concentration of **X**. For the dissociation process of the bridging ligand, the reaction rate is

$$r_{d1} = k_{-2}[\mathrm{MX_5L}] \quad (k = Ae^{-\frac{E_a}{RT}})$$

For relatively soft lewis acidic species such as Cu^{2+} and Zn^{2+}, interactions with hard basic carboxylates are relatively weak, so the activation energy E_a for the dissociation process is small, which means a large k_{-2} and a fast dissociation process. Meanwhile, the excess of solvent molecules could serve as an **X** ligand to compete with the bridging ligand **L**, which slows down the ligand substitution process. Consequently, ligand substitution and dissociation rates are comparable, allowing sufficient structure reorganization and defect reparation to form long-range ordered structures under moderate conditions.

For hard Lewis acidic species such as Fe^{3+}, Al^{3+}, and Zr^{4+}, their strong electrostatic interaction with the hard basic carboxylate give rise to a much larger E_a and smaller k_{-2}.

Even if solvent molecules act as an **X** ligand, the much larger k_1 value still causes unbalanced substitution and dissociation reaction rates. As a result, direct synthesis of those MOFs usually results in long-range disordered (amorphous) product due to the lack of structural reorganization. Since E_a is determined by the nature of the metal and the coordinating ligand, increasing the synthetic temperature **T** is an approach to raise k_{-2} and facilitate the ligand dissociation process. Unfortunately, higher temperature also accelerates the substitution process and an unbalanced substitution-dissociation process still exists. To accelerate the ligand dissociation process at higher temperature and maintain a slow ligand substitution process, an extra competing reagent **X**, which binds more strongly to the metal (smaller k_1) than the solvent molecule is necessary. With the assistance from the extra competing reagent **X**, reversible ligand rearrangement could be tuned to facilitate the crystallization process. Because it is actually the carboxylate and not the acid doing the substitution, when the deprotonation process is taken into account, extra acetic acid could simultaneously inhibit the deprotonation of the ligand, which further slows down the substitution reaction and aids the crystallization process.

As $M_3(\mu_3\text{-}O)(COO)_6$ (M=Fe, Cr, Al, Sc, V, In) is one of the most comment building block in the reported trivalent metal species containing MOFs , to test our hypothesis, we used $[Fe_2M(\mu_3\text{-}O)(CH_3COO)_6]$ as the starting material and acetic acid (acetate after deprotonation) as the competing reagent to grow Fe-MOFs with many different ligands . $[Fe_2M(\mu_3\text{-}O)(CH_3COO)_6]$ as isolated basic carboxylates have been reported for decades [25,] . Excellent solubility of these clusters increases their feasibility as a starting material. Meanwhile, due to the strong electrostatic interaction between Fe^{3+}

and μ_3-O^{2-}, the cluster is inherently robust enough to preserve the integrity of the core while going through carboxylate substitution on the periphery under solvothermal conditions. Moreover, the D_{3h} cluster itself possesses six carboxylate arms in a trigonal prismatic arrangement, which allows facile construction of three dimensional (3-D) frameworks through simple bridging. When $[Fe_2M(\mu_3\text{-}O)(CH_3COO)_6]$ is used as a starting material, direct synthesis of Fe-MOFs can be considered as a pure ligand substitution process and the framework growth can be rationalized by a traditional stepwise ligand substitution reaction model. Therefore, the addition of extra competing reagent can tune both ligand substitution and dissociation processes directly via concentration variation.

Consequently, with the assistance of acetic acid as a competing reagent, we obtained large single crystals of 34 Fe-MOFs containing the $[Fe_2M(\mu_3\text{-}O)]$ building block.

Even though the ligands shown in Fig. 65b vary in symmetry, functionality, connectivity and size, the structure of the $[Fe_2M(\mu_3\text{-}O)]$ building block is maintained in these frameworks. Thus, the new synthetic strategy can be viewed as a dimensional augmentation process from 0-D metal containing nodes of $[Fe_2M(\mu_3\text{-}O)]$ to 3-D nets. Partial substitution on the $[Fe_2M(\mu_3\text{-}O)]$ clusters has also occurred when complete substitution becomes incompatible with some of the ligands because of symmetry requirements or steric hindrance.

To demonstrate the versatility of the kinetically tuned dimensional augmentation (KTDA) strategy, MOFs with distinct structural features are discussed in detail.

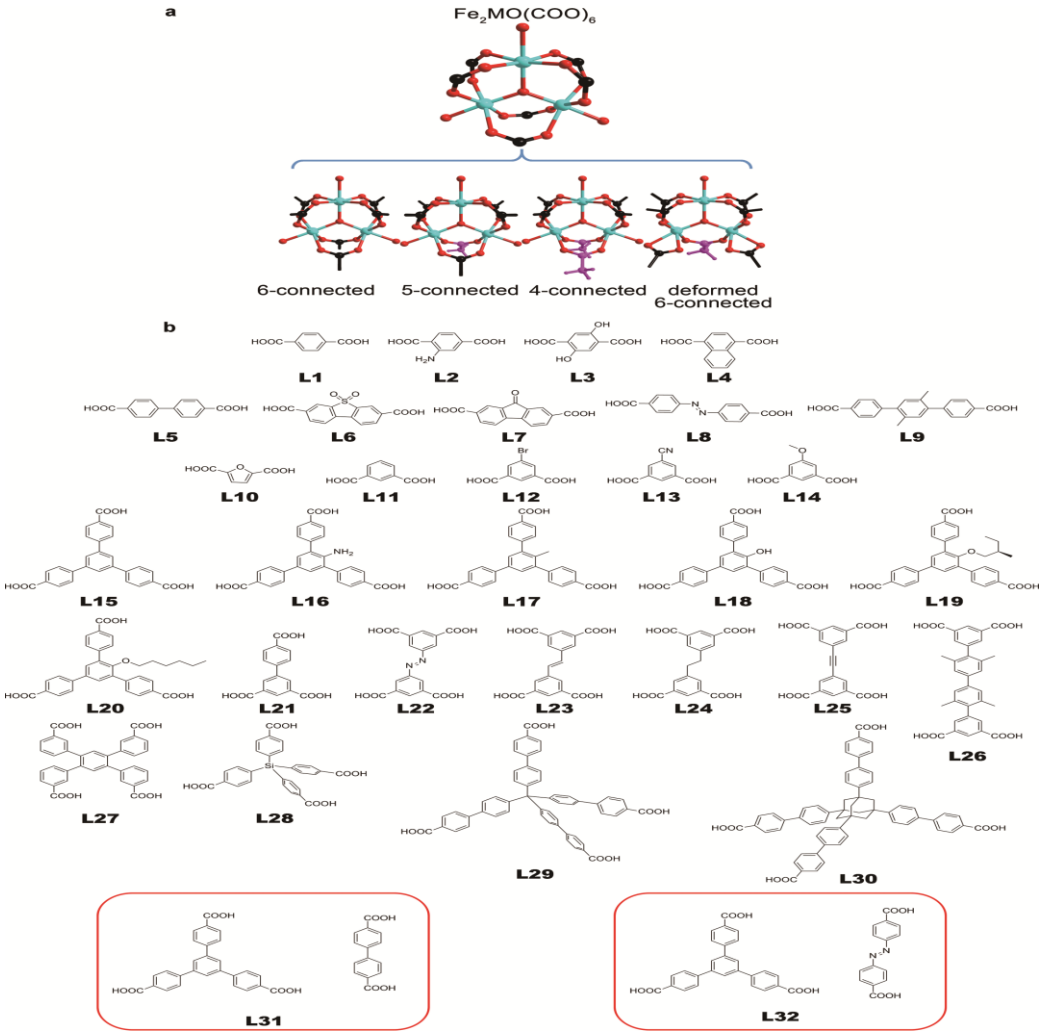

Figure 65. Organic linkers used in synthesis of [$Fe_2M(\mu_3\text{-}O)$] containing MOFs and different connecting modes. a, Four different connecting modes of the [$Fe_2M(\mu_3\text{-}O)$] cluster. Carboxylates on ligands and terminal acetates are represented by black and purple respectively. b, Thirty different ligands and two types of mixed ligands used in constructing Fe-MOFs.

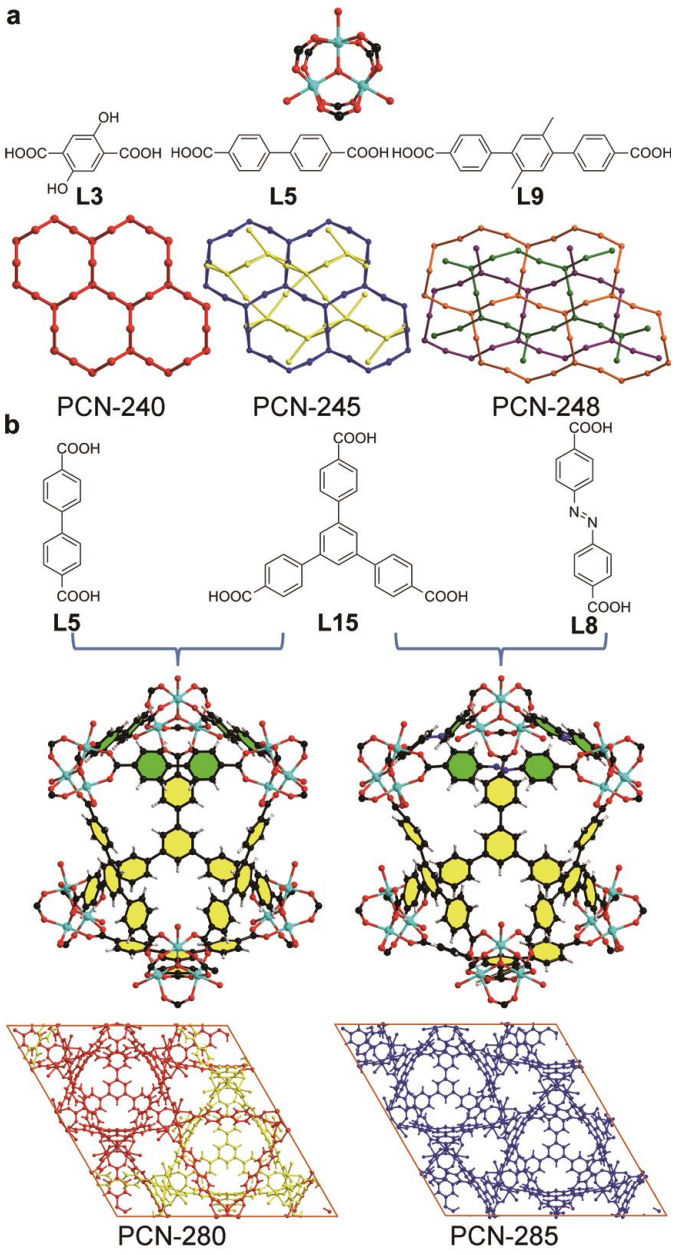

Figure 66. Functionalization, interpenetration and mixed-ligands in Fe-MOFs a, Functionalized MIL-88 isostructure, 2-fold and 3-fold self-interpenetration. b, PCN-280(interpenetrated) and PCN-285(non-interpenetrated) constructed from mixed ligands

PCN-240, constructed from **L3**, is isostructural to MIL-88 with the acs-a topology (Fig. 66a). Usually, **L3** tends to form the MOF-74 structure with two hydroxyl groups

participating in coordination. However, when starting from $[Fe_2M(\mu_3\text{-}O)(COOCH_3)_6]$, the in situ formation of the one dimensional chain can be avoided and only a simple substitution reaction occurs between carboxylates, leaving two hydroxyl groups free for other potential modifications. With elongated ligands **L5** and **L9**, which allows sufficient space for catenation, 2-fold perpendicular interpenetration and 3-fold parallel interpenetration have been observed, respectively. Interestingly, the interpenetration restricts the flexibility in each single net and therefore stabilizes the framework and generates permanent porosity (Fig. 66a). The mixed ligand strategy is challenging due to the high probability of obtaining mixed phases, especially for MOFs based on high-valence metals whose structure determination relied almost exclusively on powder x-ray diffraction. When starting with pre-assembled metal clusters, the interference from side reactions generating different inorganic building blocks is eliminated. The mixed ligand MOFs can be more easily synthesized with the KTDA strategy, which allows for growing single crystals instead of powders. Using the combinations of **L15** and **L5** as well as **L15** and **L8**, we obtained large single crystals of PCN-280 and PCN-285 (Fig. 66b).

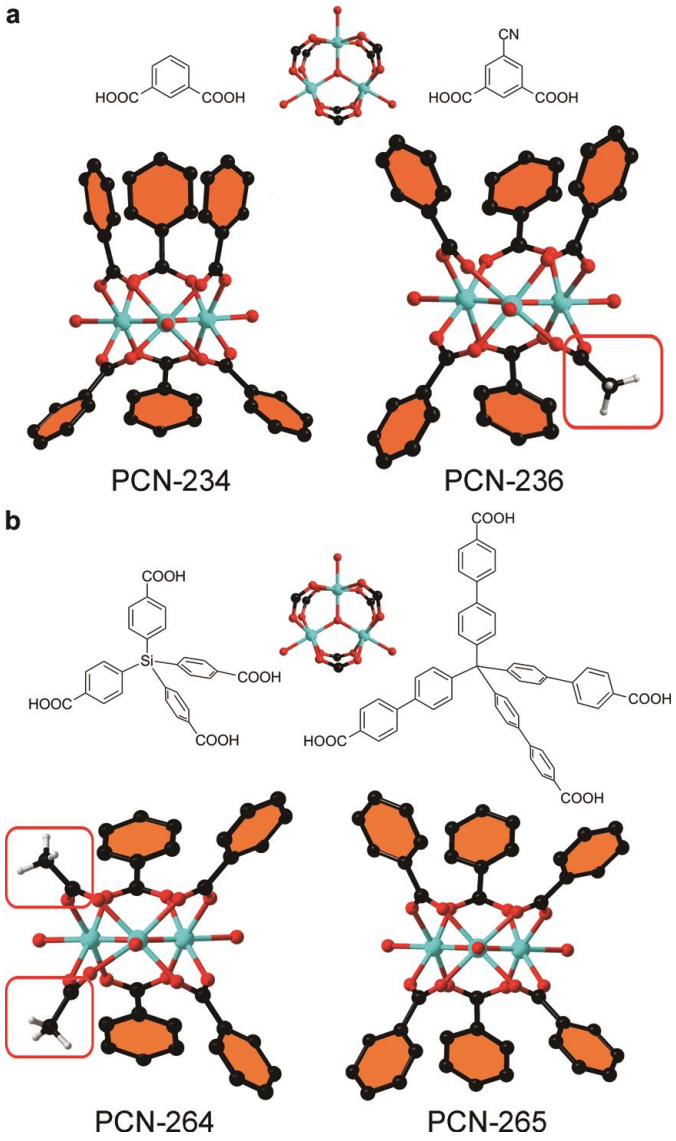

Figure 67. Partially substituted [$Fe_2M(\mu_3\text{-}O)$] in Fe-MOFs a, Bulky group induced partial substitution in PCN-236. b, Rigidity induced partial substitution in PCN-264.

PCN-234 is isostructural to MIL-59 with the CaB_6 net (Fig. 67a) [151]. When the ligand is functionalized by bulky groups like -CN, the limited distance between each ligand prevents complete substitution on the [$Fe_2M(\mu_3\text{-}O)$] cluster and forces the formation of a 5-connected cluster with acetic acid as the remaining terminal ligand (Fig.

67b), giving rise to PCN-236. This connectivity reduction also occurs with the tetrahedral ligands: in PCN-265, **L29** slightly stretches from the ideal T_d symmetry to D_{2d} symmetry to form a 6-connected [$Fe_2M(\mu_3$-O)] containing framework, while the smaller tetrahedral ligand **L28** is too rigid to bend and maintains the original T_d symmetry in PCN-264. Complete substitution on the [$Fe_2M(\mu_3$-O)] core is unable to form a long range ordered structure with T_d symmetric **L28**, so the connectivity of the [$Fe_2M(\mu_3$-O)] cluster is reduced to four (Fig. 67c). This reduced connectivity on the [$Fe_2M(\mu_3$-O)] cluster is first discovered here in these Fe-MOFs, which is also evidence of the substitution reaction of the preformed basic carboxylate.

Although all the Fe-MOFs are synthesized under similar conditions, the optimal concentration of acetic acid for each one varies greatly. According to our rationalization, extra acetic acid should slow down the substitution reaction rate, which shows the kinetic influence. When the concentration of acetic acid was much lower than the optimal value, gels or amorphous products were obtained, which suggests insufficient control of the substitution and dissociation balance. When the concentration of acetic acid is too high, solutions remain clear with no solid products even after a long period, which suggests a thermodynamic equilibrium in the solution. If MOF formation is expressed as an equilibrium and the formation of clear solution is treated as the point of a positive Gibbs free energy, then the amount of acetic acid is actually an indication of relative values for the framework's free energy of formation. The entropic effects can be clearly observed from the synthetic conditions. For ligands with similar size and connectivity, MOFs containing Fe_2MO clusters with lower connectivity always need a

lower concentration of acetic acid as the competing reagent. Meanwhile, for Fe_2MO clusters with the same connectivity, ligands with higher connecting numbers always need more acetic acid. Assuming these MOFs have similar enthalpies of formation, the concentration change of acetic acid is consistent with the entropy change. Moreover, even if the connectivity of clusters and ligands are the same, the amount of acetic acid for those MOFs still varies (Table 45), which could be attributed to an enthalpic effect.

Table 44. Entropy effect reflected from the synthetic conditions.

Ligand	Connectivity of ligand	CN on cluster	Acetic acid in 2mL solvent		
			Gel	Single crystal	Clear solution
L13	2	5	<<	~ 0.10mL	>>
L14	2	5	<<	~ 0.10mL	>>
L11	2	6	<<	~ 0.20mL	>>
L5	2	6	<<	~ 0.15mL	>>
L15	3	6	<<	~0.25mL	>>
L29	4	6	<<	~0.40mL	>>

Table 45. Enthalpy effect reflected from the synthetic conditions.

Ligand	Topics of Ligand	CN on cluster	Acetic acid in 2mL solvent		
			Gel	Single crystal	Clear solution
L22	4	6	<<	~ 1.00mL	>>
L26	4	6	<<	~ 0.50mL	>>
L29	4	6	<<	~0.40mL	>>

Methane uptake is highly related to the structure of the porous material used (*19*). Due to the structural diversity of these Fe-MOFs, we turned to computational methods to quickly rationalize and predict their performance. To identify the best materials for methane uptake, we utilize an *in silico* approach to predict a set of new structures and their methane uptake. Fig 68a shows the simulated deliverable capacities of our predicted structures and those structures that have been synthesized together with the experimental data of PCN-250(Fe_3) and PCN-250(Fe_2Co). Our simulations suggest that PCN-250 is indeed an outlying structure for vehicular methane storage using a 35 - 1 bar pressure swing. Interestingly, our screening predicts that several of the synthesized Fe-MOFs have very high deliverable capacities using a 65 - 5.8 bar pressure swing. Also, our simulations confirm that PCN-250 has the highest 35 bar loading of all structures considered in this analysis.

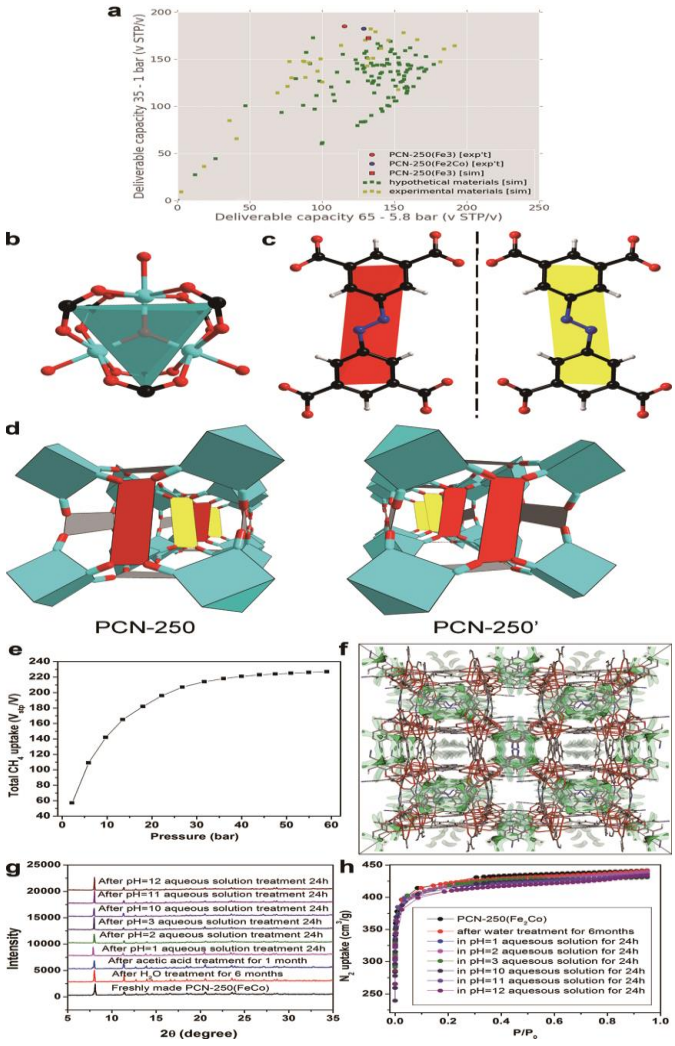

Figure 68. Simulated CH_4 adsorption of all Fe-MOFs and property of the best performers a ,Accelerating Materials Discovery through Computation. Performance plot of deliverable capacities with two different pressure swings. Shown are the predictions for the Fe-MOFs synthesized here (yellow) and in-silico predicted structures (green). Red and blue points show PCN-250.b,c and d, Structures of PCN-250 and PCN-250 ´. e, Total CH_4 adsorption uptake at 298K and f, contours of the computed potential energy surface of adsorbed CH_4 in PCN-250. g, Powder X-ray patterns and h, N_2 adsorption isotherms of PCN-250(Fe_2Co) after stability tests.

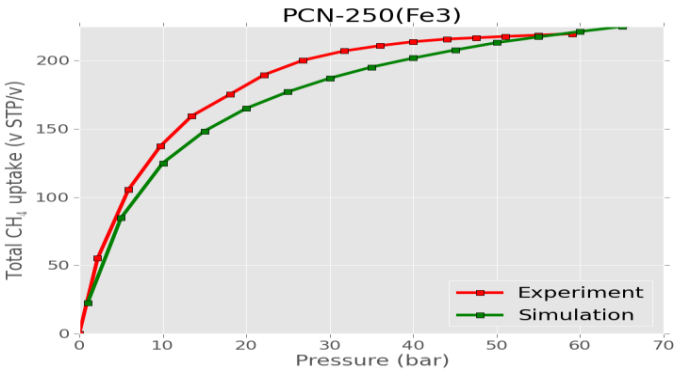

Figure 69. Our models accurately predict methane uptake in PCN-250(Fe_3). Simulated and experimental methane adsorption isotherm for PCN-250(Fe_3).

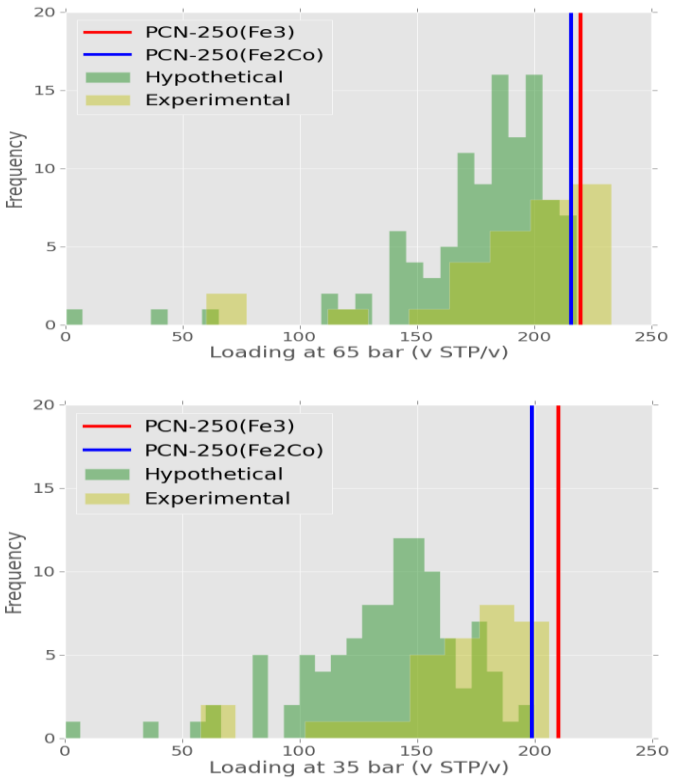

Figure 70. Histograms of loadings**.** Frequency of loadings at 65 bar (a) and 35 bar (b) of experimental and hypothetical structures in this work. For reference, the experimentally measured loadings for PCN-250(Fe_2Co) and PCN-250(Fe_3) are shown with blue and red vertical lines, respectively.

PCN-250 consists of 6-connected [$Fe_2M(\mu_3\text{-}O)$] building blocks and rectangular tetratopic **L22** (Fig.68, b, c and d), which is isostructural to the reported indium MOF. [152] Interestingly, PCN-250′, another framework isomer of PCN-250, is found under different synthetic conditions. Along one axis, ligands constructing the same cube in PCN-250 adopt mirror configurations and are alternatively arranged. In PCN-250′, ligands adopt the same configuration in the one cube and mirror configuration in the adjacent cubes along any axis. Experimental results show PCN-250(Fe_2Co) that possesses total CH_4 uptake of 210V/V at 35 bar and 298K (Fig. 68 e), which is one of the highest among all the reported MOFs. PCN-250(Fe_2Co) has a record high H_2 uptake of 3.07wt% and 28g/L at 1.2 bar and 77K. It also has one of the highest total volumetric H_2 uptakes, 60g/L , at high pressure due to its high crystal density.

From the potential energy calculation, both high uptake of H_2 and CH_4 can be attributed to suitable size of the cage in PCN-250 and the well dispersed, highly charged open metal sites (Fig. 68 f). Each cube in PCN-250 is faced by **L22** and the channels between each cube are surrounded by high valent open metal sites. Therefore, all of the void space is provided with adsorption sites which can strongly interact with both H_2 and CH_4 molecules. This results in efficient space utilization to reach a high volumetric uptake, and leads to an induced polarization of gas molecules by high-valence metal cations through charge-induced-dipole interaction. This high-valence metal ion and induced dipole interaction can polarize additional layers of gas molecules, allowing multiple layers of gas to adsorb without significant drop in the adsorption enthalpy. The heat of adsorption is relatively low compared to a single-site adsorption by orbital

interaction, such as the Kubas binding of hydrogen molecules. However, it is far-reaching, making it nearly flat over a wide uptake range.

Even after the insertion of the softer Lewis acid M(II) in the μ_3-oxo trimmer, the PCN-250 series still shows extraordinary chemical stability. The powder patterns of PCN-250(Fe_2Co) remained unaltered upon immersion in glacial acetic acid and pH=1 to pH=11 aqueous solutions for 24h (Fig 68, g and h). The framework of PCN-250(Fe_2Co) remained stable under H_2O after 6 months. Moreover, the N_2 adsorption isotherms of PCN-250(Fe_2Co) remain constant after all these treatments, which suggests no phase transition or framework decomposition during all treatments. A combination of high uptake and chemical stability is quite rare for MOFs, and this combination can guarantee the reusability of the sorbent for industrial applications. With its high gas uptake, extraordinary stability, and excellent scalability, PCN-250 is a viable candidate for natural gas storage for automotive applications.

4.4 Conclusions

Based on a kinetic model of ligand-substitution reactions, utilizing pre-formed $[Fe_2M(\mu_3\text{-}O)(COOCH_3)_6]$ clusters (M represents Fe(II,III), Mn(II), Co(II), Ni(II), or Zn(II)), we have developed a kinetically tuned dimensional augmentation (KTDA) synthetic route for the preparation of highly crystalline and extremely robust metal-organic frameworks (MOFs) with the preserved metal cluster core. Through this versatile synthetic route, we have obtained large single crystals of thirty-four different

Fe-MOFs. Among them, PCN-250(Fe_2Co) exhibits a record-high gravimetric and volumetric H_2 uptake at 77 K/1.2 bar as well as an exceptionally high volumetric uptake at high pressure. The total CH_4 uptake (210 V(STP)/V) of PCN-250(Fe_2Co) at 298 K and 35 bar is also among the highest reported. Remarkably, PCN-250(Fe_2Co) exhibits extraordinary stability in water and aqueous solutions with a wide range of pH values.

5. SUMMARY

In this dissertation, three independent projects based on stable metal-organic frameworks have been accomplished .In the first project, five different porphyrininc zirconium MOFs have been synthesized. These five zirconium MOFs exhibit different structures, porosity as well as chemical stability. Among them, PCN-222 has one of the largest 1-D channel(3.7nm) and can be stable in concentrated HCl. Moreover, due to the extraordinary chemical stability and highly dense porphyrinic center in the framework, PCN-222 can be used for biomimetic application and shows high catalytic activity even compared to the enzyme –horseradish peroxidase, which demonstrated MOFs potentials as practical applicable heterogeneous catalyst. PCN-223 as a heterogeneous catalyst for hetero Diels Alder reaction, shows even better catalytic performance compared to the homogeneous protocol catalyst. More importantly, the crystallinity of PCN-223 is well maintained after many catalytic cycles due ot its high stability. PCN-225 was also demonstrated as a heterogeneous pH sensor, which is the first proof of concept study for such application in MOFs field. The excellent performance of the catalytic porphyrin moiety in these frameworks are all supported by the high chemical stability of these MOFs, which demonstrates the importance of framework stability for expanding MOFs' potential applications. A series of highly stable mesoporous MOFs based on trivalent metal species have also been obtained. Due to their high stability of ultralarge pores, PCN-333(Al) was selected as the support to immobilize HRP and cyto-C. The loading amount of HRP and Cyto-c in PCN-333 (Al) can reach as high as 1g/g, which is the

highest among all the reported porous solid state supports. More importantly, due to the suitable pore size, the immobilized enzymes can be ideally isolated into each cage, which can form single molecular trap for enzyme and stabilize the entrapped enzymes. As a result, PCN-333(Al) immobilized HRP and Cyto-c both show improved catalytic performance either under the conventional aqueous media or organic solvent. More importantly, due to the heterogeneous feature, immobilized enzymes can be easily recycled through the simple filtration, which greatly promoted the potential of enzyme engineering by reducing the cost through convenient recycle process.

Also a new synthetic strategy, kinetically tuned dimensional augmentation has been developed for the synthesis of large single crystalline Fe-MOFs. Based on the simple interpret of MOFs growing process, using preform Fe-clusters and acetic acid as competing reagent, 34 single crystalline Fe-MOFs have been obtained. Among these Fe-MOFs, PCN-250 shows very high methane uptake capacity (235V/V) at 35bar as well as excellent stability either in the air or water (maintaining stability more than six months), which is an very promising candidate for on-board methane storage absorbent in vehicles.

REFERENCES

(1) Walton, K. S.; Snurr, R. Q. *J. Am. Chem. Soc.* **2007**, *129*, 8552.

(2) Eddaoudi, M.; Moler, D. B.; Li, H.; Chen, B.; Reineke, T. M.; O'Keeffe, M.; Yaghi, O. M. *Acc. Chem. Res.* **2001**, *34*, 319.

(3) Yaghi, O. M.; O'Keeffe, M.; Ockwig, N. W.; Chae, H. K.; Eddaoudi, M.; Kim, J. *Nature* **2003**, *423*, 705.

(4) Zhou, H.-C.; Long, J. R.; Yaghi, O. M. *Chem. Rev.* **2012**, *112*, 673.

(5) Perry Iv, J. J.; Perman, J. A.; Zaworotko, M. J. *Chem. Soc. Rev.* **2009**, *38*, 1400.

(6) O'Keeffe, M.; Yaghi, O. M. *Chem. Rev.* **2011**, *112*, 675.

(7) Ferey, G.; Serre, C. *Chem. Soc. Rev.* **2009,** *38*, 1380.

(8) Horike, S.; Shimomura, S.; Kitagawa, S. *Nat. Chem.* **2009,** *1*, 695.

(9) Long, J. R.; Yaghi, O. M. *Chem. Soc. Rev.* **2009,** *38*, 1213.

(10) Yaghi, O. M.; O'Keeffe, M.; Ockwig, N. W.; Chae, H. K.; Eddaoudi, M.; Kim, J. *Nature* **2003,** *423*, 705.

(11) Chui, S. S.-Y.; Lo, S. M.-F.; Charmant, J. P. H.; Orpen, A. G.; Williams, I. D. *Science* **1999,** *283*, 1148.

(12) Furukawa, H.; Cordova, K. E.; O'Keeffe, M.; Yaghi, O. M. *Science* **2013,** *341*, 974.

(13) Zhou, H.-C.; Long, J. R.; Yaghi, O. M. *Chem. Rev.* **2012,** *112*, 673.

(14) Li, J.-R.; Sculley, J.; Zhou, H.-C. *Chem. Rev.* **2012,** *112*, 869.

(15) Foo, K. Y.; Hameed, B. H. *Adv. Colloid Interfac* **2011,** *162*, 22.

(16) Cui, Y.; Yue, Y.; Qian, G.; Chen, B. *Chem. Rev.* **2012,** *112*, 1126.

(17) Kurmoo, M. *Chem. Soc. Rev.* **2009,** *38*, 1353.

(18) Zhang, W.; Xiong, R.-G. *Chem. Rev.* **2012,** *112*, 1163.

(19) Suh, M. P.; Park, H. J.; Prasad, T. K.; Lim, D.-W. *Chem. Rev.* **2012,** *112*, 782.

(20) Makal, T. A.; Li, J.-R.; Lu, W.; Zhou, H.-C. *Chem. Soc. Rev.* **2012,** *41*, 7761.

(21) Dunford, H. B. in *Encyclopedia of Catalysis*, John Wiley & Sons, Inc., **2002**;

(22) Shaik,S.; Cohen, S.; Wang, Y.; Chen, H.; Kumar, D.; Thiel, W. *Chem. Rev.* **2009**, *110*, 949.

(23) Wang,Q.; Yang, Z.; Zhang, X.; Xiao, X.; Chang,C. K.; Xu, B. *Angew. Chem. Int. Ed.* **2007**, 46, 4285.

(24) Xue,T.; Jiang, S.; Qu,Y.; Su,Q.; Cheng, R.; Dubin, S.; Chiu,C.-Y. ; Kaner, R.; Huang, Y.; Duan, X. *Angew. Chem. Int. Ed.* **2012,** 51, 3822.

(25) Shema-Mizrachi, M.; Pavan, G. M.; Levin, E.; Danani, A.; Lemcoff, N. G. *J. Am. Chem. Soc.* **2011**, *133*, 14359.

(26) Bezzu, C. G.; Helliwell, M. J.; Warren,E. D.; Allan, R. N.; McKeown, B. *Science* **2010**, *327*, 1627.

(27) Zhou, H.-C.; Long, J. R.; Yaghi, O. M. *Chem. Rev.* **2012**, *112*, 673.

(28) Horcajada, P. ; Gref, R. ; Baati, T. ; Allan, P. K. ; Maurin, G. ; Couvreur, P. ; Férey, G. ; Morris, R. E. ; Serre, C. *Chem. Rev.* **2012**, *112*, 1232.

(29) Kreno,L. E. ; Leong, K. ; Farha, O. K. ; Allendorf, M. ; Van Duyne,R. P. ; Hupp, J. T. *Chem. Rev.* **2012**, *112*, 1105.

(30) Suh, M. P.; Park, H. J.; Prasad,T. K.; Lim, D.-W. *Chem. Rev.* **2012**, *112*, 782.

(31) Yoon, M.; Srirambalaji, R.; Kim, K. *Chem. Rev.* **2012**, *112*, 1196.

(32) Li,J.-R.; Sculley, J.; Zhou, H.-C. *Chem. Rev.* **2012**, *112*, 869.

(33) Wu, H.; Gong,Q.; Olson,D. H. J. Li, *Chem. Rev.* **2012**, *112*, 836.

(34) Morris,W.; Volosskiy,B.; Demir, S.; Gándara, F.; McGrier, L.; Furukawa, H.; Cascio, D.; Stoddart, J. F.; Yaghi, O. M. *Inorg. Chem.* **2012**, *51*, 6443.

(35) Lu,W.-G.; Su, C.-Y.; Lu, T.-B. L.; Jiang, J.-M. Chen, *J. Am. Chem. Soc.* **2005**, *128*, 34.

(36) Jiang, H.-L.; Xu, Q. *Chem. Commun.* **2011**, *47*, 3351.

(37) Umemura, A.; Diring, S.; Furukawa, S.; Uehara, H.; Tsuruoka,T. ; Kitagawa,S. *J. Am. Chem. Soc.* **2011**, *133*, 15506.

(38) Hupp, J. T. *Nat. Chem.* **2010**, *2*, 432.

(39) Abrahams,B.; Hoskins, F. B.; Michail,D. M.; Robson, R. *Nature* **1994**, *369*, 727.

(40) Kosal,M. E.; Chou, J.-H.; Wilson,S. R.; Suslick,K. S. *Nat. Mater.* **2002**, *1*, 118.

(41) Alkordi, M. H.; Liu,Y.; Larsen, R. W.; Eubank,J. F.; Eddaoudi, M. *J. Am. Chem. Soc.* **2008**, *130*, 12639.

(42) Shultz, A. M.; Farha, O. K.; Hupp,J. T.; Nguyen, S. T. *J. Am. Chem. Soc.* **2009**, *131*, 4204.

(43) Larsen,R. W.; Wojtas, L.; Perman, J.; Musselman, R. L.; Zaworotko,M. J.; Vetromile, C. M. *J. Am. Chem. Soc.* **2011**, *133*, 10356.

(44) Farha,O. K.; Shultz, A. M.; Sarjeant,A. A.; Nguyen, S. T.; Hupp, J. T. *J. Am. Chem. Soc.* **2011**, *133*, 5652.

(45) Zou,C. ; Zhang, Z.; Xu, X.; Gong, Q.; Li, J.; Wu, C.-D. *J. Am. Chem. Soc.* **2011**, *134*, 87.

(46) Zhang, Z.; Zhang, L.; Wojtas, L.; Eddaoudi, M.; Zaworotko,M. J. *J. Am. Chem. Soc.* **2012**, *134*, 928.

(47) Zhang, Z.; Zhang, L.; Wojtas, L.; Nugent, P.; Eddaoudi, M. ; Zaworotko, M. J. *J. Am. Chem. Soc.* **2012**, *134*, 924.

(48) Wang, X.-S.; Meng, L.; Cheng, Q.; Kim, C.; Wojtas, L.; Chrzanowski, M.; Chen, Y.-S.; Zhang, X. P.; Ma, S. *J. Am. Chem. Soc.* **2011**, *133*, 16322.

(49) Choi, E.-Y.; DeVries, L. D.; Novotny, R. W.; Hu, C.; Choe, W. *Cryst. Growth Des.* **2009**, *10*, 171.

(50) Choi, E.-Y.; Wray, C. A.; Hu, C.; Choe, W. *CrystEngComm* **2009**, *11*, 553.

(51) Barron, P. M. ; Wray, C. A.; Hu, C. H.; Guo, Z. Y.; Choe, W. *Inorg. Chem.* **2010**, *49*, 10217.

(52) Choi, E.-Y. ; Barron, P. M. ; Novotny, R. W. ; Son, H.-T. ; Hu, C. ; Choe, W. *Inorg. Chem.* **2008**, *48*, 426.

(53) Verduzco, J. M.; Chung, H.; Hu, C.; Choe, W. *Inorg. Chem.* **2009**, *48*, 9060.

(54) Zou,C.; Wu, C.-D. *Dalton Trans.* **2012**, *41*, 3879.

(55) An, J.; Farha, O. K.; Hupp, J. T.; Pohl, E.; Yeh, J. I.; Rosi, N. L. *Nat. Commun.* **2012**, *3*, 604.

(56) Cavka, J. H.; Jakobsen, S. ; Olsbye, U.; Guillou, N.; Lamberti, C.; Bordiga, S.; Lillerud, K. P. *J. Am. Chem. Soc.* **2008**, *130*, 13850.

(57) Schaate, A.; Roy, P.; Godt, A.; Lippke, J.; Waltz, F.; Wiebcke, M.; Behrens, P. *Chem. Eur. J.* **2011**, *17*, 6643.

(58) Wang, C.; Xie, Z.; deKrafft, K. E.; Lin, W. *J. Am. Chem. Soc.* **2011**, *133*, 13445.

(59) Koh, K.; Wong-Foy, A. G.; Matzger, A. J.*Angew. Chem. Int. Ed.* **2008**, *47*, 677.

(60) Deng, H ; Grunder, S.; Cordova, K. E.; Valente,C.; Furukawa, H.; Hmadeh, M.; Gándara, F.; Whalley, A. C.; Liu, Z. ; Asahina, S.; Kazumori, H.; O'Keeffe, M.; Terasaki, O.; Stoddart, J. F.; Yaghi, O. M. *Science* **2012**, *336*, 1018.

(61) Metelitsa, D. I.; Rus, O. B.; Puchkaev, A. V. *Russ. J. Appl. Chem.* **1997**, *70*, 1629.

(62) Gao, L. Z.; Zhuang, J.; Nie, L.; Zhang, J. B.; Zhang,Y. ; Gu, N.; Wang,T. H.; Feng, J.; Yang, D. L.; Perrett, S. X. Yan, *Nat. Nanotechnol.* **2007**, *2*, 577.

(63) Bindhu, L.; Emilia Abraham, V. T. *Biochem. Eng. J.* **2003**, *15*, 47.

(64) Juan-Alcañiz, J.; Gascon , J.; Kapteijn, F. *J. Mater. Chem.* **2012**, *22*, 10102.

(65) Tranchemontagne, D. J.; Mendoza-Cortés, J. L.; O'Keeffe, M.; Yaghi, O. M. *Chem. Soc. Rev.* **2009**, *38*, 1257.

(66) Perry IV, J. J.; Perman, J. A.; Zaworotko, M. J. *Chem. Soc. Rev.* **2009**, *38*, 1400.

(67) Cavka, J. H.; Jakobsen, S.; Olsbye, U.; Guillou, N.; Lamberti, C.; Bordiga, S.; Lillerud, K. P. *J. Am. Chem. Soc.* **2008**, *130*, 13850.

(68) Schaate A.; Roy, P.; Godt, A.; Lippke, J.; Waltz, F.; Wiebcke, M.; Behrens, P. *Chem. Eur. J.* **2011**, *17*, 6643.

(69) Schaate, A.; Roy, P.; Preuße, T.; Lohmeier, S. J.; Godt, A.; Behrens, P. *Chem. Eur. J.* **2011**, *17*, 9320.

(70) Morris, W.; Volosskiy, B.; Demir, S.; Gándara, F.; McGrier, P. L.; Furukawa, H.; Cascio, D.; Stoddart, J. F.; Yaghi, O. M. *Inorg. Chem.* **2012**, *51*, 6443.

(71) Bon, V.; Senkovskyy, V.; Senkovska, I.; Kaskel, S. *Chem. Commun.* **2012**, *48*, 8407.

(72) Jiang, H.-L.; Feng, D.; Liu, T.-F.; Li, J.-R.; Zhou, H.-C. J. *J. Am. Chem. Soc.* **2012**, *134*, 14690.

(73) Feng, D.; Gu, Z.-Y.; Li, J.-R.; Jiang, H.-L.; Wei, Z.; Zhou, H.-C. *Angew. Chem. Int. Ed.* **2012**, *51*, 10307.

(74) Guillerm, V.; Ragon, F.; Dan-Hardi, M.; Devic, T.; Vishnuvarthan, M.; Campo, B.; Vimont, A.; Clet, G.; Yang, Q.; Maurin, G.; Férey, G.; Vittadini, A.; Gross, S.; Serre, C. *Angew. Chem. Int. Ed.* **2012**, *51*, 9267.

(75) Kickelbick, G.; Holzinger, D.; Brick, C.; Trimmel, G.; Moons, E. *Chem. Mater.* **2002,** *14*, 4382.

(76) Otero, A.; Fernández-Baeza, J.; Antiñolo, A.; Tejeda, J.; Lara-Sánchez, A.; Sánchez-Barba, L.; Fernández-López, M.; López-Solera, I. *Inorg. Chem.* **2004**, *43*, 1350.

(77) Baumann, S. O.; Puchberger, M.; Schubert, U. *Dalton Trans.* **2011**, *40*, 1401. (d) Gross, S. *J. Mater. Chem.* **2011**, *21*, 15853.

(78) Babcock, L. M.; Day, V. W.; Klemperer, W. G. *Inorg. Chem.* **1989**, *28*, 806.

(79) Dalgarno, S. J.; Atwood, J. L.; Raston, C. L. *Inorg. Chim. Acta* **2007**, *360*, 1344.

(80) APEX2 v2012.2.0 and SAINT v7.68A data collection and data processing programs, respectively. Bruker Analytical X-ray Instruments, Inc., Madison, WI; SADABS v2008/1 semi-empirical absorption and beam correction program. G.M. Sheldrick, University of Göttingen, Germany.

(81) Sheldrick, G. M. *SHELXTL*, Version 6.14, Structure Determination Software Suite, Bruker AXS, Madison, WI, **2003**.

(82) Brown, I. D.; Altermatt, D. *Acta Crystallogr.* **1985**, *B 41*, 244.

(83) Brese, N. E.; O'Keeffe, M. *Acta Crystallogr.* **1991**, *B 47*, 192.

(84) Liao, W.; Zheng, T.; Wang, P.; Tu, S.; Pan, W. *J. Environ. Sci.* **2010**, *22*, 1800.

(85) Lan, M.; Zhao, H.; Yuan, H.; Jiang, C.; Zuo, S.; Jiang, Y. *Dyes Pigments* **2007**, *74*, 357.

(86) Farha, O. K.; Shultz, A. M.; Sarjeant, A. A.; Nguyen, S. T.; Hupp, J. T. *J. Am. Chem. Soc.* **2011**, *133*, 5652.

(87) Lee, C. Y.; Farha, O. K.; Hong, B. J.; Sarjeant, A. A.; Nguyen, S. T.; Hupp, J. T. *J. Am. Chem. Soc.* **2011**, *133*, 15858.

(88) Burnett, B. J.; Barron, P. M.; Hu, C.; Choe, W. *J. Am. Chem. Soc.* **2011**, *133*, 9984.

(89) Yang, X.-L.; Xie, M.-H.; Zou, C.; He, Y.; Chen, B.; O'Keeffe, M.; Wu, C.-D. *J. Am. Chem. Soc.* **2012**, *134*, 10638.

(90) O'Keeffe, M.; Delgado-Friedrichs, O.; Yaghi, O. M. *Acta Crystallogr.* **2006**, *A 62*, 350.

(91) Chang, Z.; Zhang, D.-S.; Hu, T.-L.; Bu, X.-H. *Cryst. Growth Des.* **2011**, *11*, 2050.

(92) Zhao, X.; Wang, X.; Wang, S.; Dou, J.; Cui, P.; Chen, Z.; Sun, D.; Wang, X.; Sun, D. *Cryst. Growth Des.* **2012**, *12*, 2736.

(93) Spek, A. L. *J. Appl. Crystallogr.* **2003**, *36*, 7.

(94) Fei, H.; Rogow, D. L.; Oliver, S. R. J. *J. Am. Chem. Soc.* **2010**, *132*, 7202.

(95) Zheng, S.-T.; Bu, J. J.; Wu, T.; Chou, C.; Feng, P.; Bu, X. *Angew. Chem. Int. Ed.* **2011**, *50*, 8858.

(96) Zheng, S.-T.; Wu, T.; Zuo, F.; Chou, C.; Feng, P.; Bu, X. *J. Am. Chem. Soc.* **2012**, *134*, 1934.

(97) Fateeva, A.; Devautour-Vinot, S.; Heymans, N.; Devic, T.; Grenèche, J.-M.; Wuttke, S.; Miller, S.; Lago, A.; Serre, C.; Weireld, G. D.; Maurin, G.; Vimont, A.; Férey, G. *Chem. Mater.* **2011**, *23*, 4641

(98) Wang, X.-S.; Chrzanowski, M.; Gao, W.-Y.; Wojtas, L.; Chen, Y.-S.; Zaworotko, M. J.; Ma, S. *Chem. Sci.* **2012**, *3*, 2823.

(99) Weissermel, K.; Arpe, H.-J. Industrial Organic Chemistry, second ed., VCH Press, Weinheim, **1993**.

(100) Grootboom, N.; Nyokong, T. *J. Mol. Catal A: Chem.* **2002**, *179*, 113.

(101) Alkordi, M. H.; Liu, Y.; Larsen, R. W.; Eubank, J. F.; Eddaoudi, M. *J. Am. Chem. Soc.* **2008**, *130*, 12639.

(102) Maksimchuk, N. V.; Kovalenko, K. A.; Fedin, V. P.; Kholdeeva, O. A. *Chem. Commun.* **2012**, *48*, 6812.

(103) Paddock, R. L.; Hiyama, Y.; McKay, J. M.; Nguyen, S. T. *Tetrahedron Lett.* **2004**, 45, 2023.

(104) Lu, X.-B.; Darensbourg, D. J. *Chem. Soc. Rev.* **2012**, *41*, 1462.

(105) Friedrichs,O.D.; O'Keeffe,M.; Yaghi,O.M. *Acta. Crystallogr. A,***2006**, 62, 350

(106) Tietze, L.-F.; Kettschau, G. Top. *Curr. Chem.* **1997**, 189, 1.

(107) Aggarwal, V.; Vennall, P. G. ; Davey, P. N.; Newman, C. *Tetrahedron Lett.* **1997**, 38, 2569.

(108) Cavka, J. H.; Jakobsen, S.; Olsbye, U.; Guillou, N.; Lamberti, C.; Bordiga, S.; Lillerud, K. P. *J. Am. Chem. Soc.* **2008**, *130*, 13850.

(109) Banerjee, D.; Borkowski, L. A.; Kim, S. J.; Parise, J. B. *Cryst. Growth Des.* **2009**, *9*, 4922.

(110) Ibarra, I. A.; Yang, S.; Lin, X.; Blake, A. J.; Rizkallah, P. J.; Nowell, H.; Allan, D. R.; Champness, N. R.; Hubberstey, P.; Schröder, M. *Chem. Commun.* **2011**, *47*, 8304.

(111) Colombo, V.; Galli, S.; Choi, H. J.; Han, G. D.; Maspero, A.; Palmisano, G.; Masciocchi, N.; Long, J. R. *Chem. Sci.* **2011**, *2*, 1311.

(112) Feng, D.; Gu, Z.-Y.; Li, J.-R.; Jiang, H.-L.; Wei, Z.; Zhou, H.-C. *Angew. Chem. Int. Ed.* **2012**, *51*, 10307.

(113) Manna, B. K.; Bera, S. C.; Rohatgi-Mukherjee, K. K. *Spectrochim. Acta, Part A* **1995**, *51*, 1051.

(114) Thyagarajan, S.; Leiding, T.; Årsköld, S. P.; Cheprakov, A. V.; Vinogradov, S. A. *Inorg. Chem.* **2010**, *49*, 9909

(115) Cui, Y.; Yue, Y.; Qian, G.; Chen, B. *Chem. Rev.* **2012**, 112, 1126.

(116) Harbuzaru, B. V.; Corma, A.; Rey, F.; Jordá, J. L.; Ananias, D.; Carlos, L. D.; Rocha, J. *Angew. Chem. Int. Ed.* **2009**, 48, 6476.

(117) Zhou, H.-C.; Yaghi, O.M.; Long, J. R. *Chem. Rev.* **2012.** 112, 673.

(118) Férey, G. *et al., Science* **2005**, 309, 2040.

(119) Deng, H. *et al., Science* **2012**, 336, 1018.

(120) V. Lykourinou *et al., J. Am. Chem. Soc.* **2011**,133, 10382.

(121) Hudson, S.; Cooney, J.; Magner, E. *Angew. Chem. Int. Ed.* **2008**, 47 , 8582.

(122) Klibanov, A. M. *Science* **1983**, 219, 722.

(123) Filice, M.; Guisan, J. M.; Terreni, M.; Palomo, J. M. *Nature protocols* **2012**, 7, 1783.

(124) Datta, S. *et al.*, Materials. *Biotech*, **2013**, *3:1–9.* 2.

(125) Engstrom, K. *et al., Angew. Chem. Int. Ed.* **2013,** 52 , 14006.

(126) Li, J.-R. *et al., Nature Commun.* **2013**, 4,1538.

(127) Liu, W.-L. *et al*; *Chem. Eur. J.* **2014**, 20, 8923.

(128) Liu, W.-L. *et al*; *J. Mater. Chem. B*. **2013,**1, 928.

(129) Furukawa, H. *et al*. *Science* **2010,** 329, 424.

(130) Farha, O. K. *et al*. *J. Am. Chem. Soc.* **2012,** 134,15016.

(131) Yuan, D. *et al. Angew. Chem. Int. Ed.* **2010,** 49 , 5357.

(132) Koh, K.; Wong-Foy, A. G.; Matzger, A. J. *Angew. Chem. Int. Ed*. **2008**, 47, 677.

(133) Farha, O. K. *et al*. *Nat. Chem*. **2010,** 2, 944.

(134) Chae, H. K. *et al*. *Nature* **2004,** 427, 523.

(135) Furukawa, H.; Cordova, K. E.; O'Keeffe, M.; Yaghi, O. M. *Science* **2013**, 341, 1230.

(136) Férey, G. *et al*. *Angew. Chem. Int. Ed*. **2004,** 43, 6296.

(137) Bloch, E. D. *et al*. *J. Am. Chem. Soc*. **2010**, 132, 14382.

(138) Millange, F. *et al*. *Chem. Commun*. **2002**, 822.

(139) Reinsch, H. *et al. Chem. Commun.* **2012,** 48, 9486.

(140) Yang, S. *et al.*, *Nat. Chem.* **2012,** 4, 887.

(141) Serre, C. *et al*., *Science* **2007,**315, 1828.

(142) An, J. *et al.*, *Nat. Commun.* **2012,** 3, 604.

(143) Li, T. *et al*., *J. Am. Chem. Soc*. **2013**, 135, 11688.

(144) Qiao, S. Z. *et al*., *Chem. Mater*. **2005**, 17, 6172.

(145) Deere, J.; Magner, E.; Wall, J. G.; Hodnett, B. K. *J. Phys. Chem. B.* **2002**, 106, 7340.

(146) Takahashi, H. *et al*., *Chem. Mater.* **2000,** 12, 3301.

(147) Vazquez-Duhalt, R. *J. Mol. Catal. B: Enzym.* **1999**,**7**, 241.

(148) Vazquez-Duhalt, R.; Semple, K. M.; Westlake, D. W.; Fedorak, P. M., *Enzyme. Microb. Technol.* **1993**, 15, 936.

(149) Li, L. *et al*., *Nat.Comm.***2013,** 4, 1774.

(150) Makal,T.A., Li,J.-R., Lu ,W., Zhou,H.-C. *Chem.Soc.Rev*. **2012,** 41, 7761.

(151) Barthelet, K. *et al. Chem. Commun*. **2002,** 1492.

(152) Liu, Y. et al. *Angew. Chem. Int. Ed.* **2007,** 46, 3278.